Cellular Dynamics of Tumor-Vessel Interactions in Breast Cancer Metastasis

by

Vanesa Laura Silvestri

A dissertation submitted to Johns Hopkins University in conformity with the
requirements for the degree of Doctor of Philosophy

Baltimore, Maryland

May 2019

Abstract

A key goal in cancer research is to understand the underlying mechanisms of the metastatic process, by which cancer cells spread from a primary tumor to other sites and form secondary tumors. Indeed, metastasis is responsible for around 90% of cancer patient mortality. However, metastatic dissemination is an inefficient process as only a small subset of cancer cells leaving the primary tumor has the potential to form metastases. In experimental animal models, less than 0.02% of the single tumor cells leaving the primary tumor ultimately develop metastases. We have found that cells from primary tumors sometimes escape as clusters, and those cell clusters more efficiently form metastases compared to single tumor cells.

Based on our previous findings, we aimed to investigate the ways in which tumors interact with the vasculature that would allow the intravasation of polyclonal tumor cell clusters. A barrier to answer this question is largely a result of the difficulties in establishing models in which the dynamics of tumor-vessel interactions can be visualized and characterized. To overcome this barrier, we used of a microfluidic approach with a physiologically and morphologically realistic vasculature along with 3D organotypic culture of tumor organoids. This device allowed us real-time and quantitative assessment of tumor- vessel interactions under *in vivo* like conditions.

We observed the dynamics of three types of tumor-vessel interactions: mosaic vessel (i.e., partial endothelial cell lining), vessel constriction, and vessel pull. We found that mosaic vessels are the most frequent type of tumor-vessel interaction observed *in vitro*. Moreover, our work shows that tumor cells invade through the vessel wall by integrating and displacing the endothelial cell lining suggesting a tumor-endothelial cell junction. Furthermore, we were able to observe in real time the passive shedding of a tumor cell cluster that preceded mosaic vessel formation.

This study is the first to show the dynamics of tumor-vessel interactions using a 3D microvessel model along with 3D organotypic culture of primary breast cancer tissue. We anticipate that deeper understanding of the mechanisms of tumor-vessel interactions along with intravasation will provide new insights for targeted anti-metastatic treatments.

Primary reader and advisor: Andrew J. Ewald

Secondary reader: Peter C. Searson

Acknowledgments

I am lifetime indebted to my mentor and thesis advisor Dr. Andrew Ewald for his assistance, guidance, support and enthusiasm over my entire PhD Program at the Johns Hopkins University. His professional guidance has been a vital source of inspiration and encouragement during my first steps in the journey of scientific research. It has been a great joy to learn from him and work with him. His advice both on strictly scientific research as well as on career path aspects have helped me tremendously in shaping the researcher I am today and what I aspire for the future. He calls a spade a spade, which coupled with his sharp and insightful comments proves to be essential for research progress.

I also would like to express my gratitude to Dr. Peter Searson who has been an invaluable collaborator who has crucially helped me to learn and understand the insights, making, and language of an engineer.

I would also like to thank all the past and current members of the Ewald and Searson labs. I couldn't have asked for a better group of colleagues and friends. I will certainly miss working with them, but I trust our paths will cross in the near future.

This dissertation is specially dedicated to Guillermo, my husband, to whom I could have not getting this far. Thank you for the being a role model and for the many sacrifices you have made in order for me to complete this lengthy project. You love me unconditionally, in spite of all my mood swings. Since the first day you constantly supported me and encouraged me to pursue my goals. I am indebted to you for being always there. To my parents, Micaela and Marcelino, thanks for instilling in me the importance of a good education, hard work and perseverance and for being always enthusiastic despite the distance. To my brother, Hugo, who has provided me with continuous encouragement and provided me with tons of love. To my in-laws, Elinor and Raul, who always believed in me and supported Guillermo and me since we started our journey years ago.

Table of Contents

List of Figures

CHAPTER 1

Understanding the role of the tumor microenvironment in cancer invasion and intravasation

Introduction

Breast cancer is the second leading cause of cancer-related mortality among women in the United States. Metastasis is responsible for more than 90% of breast cancer deaths (Weigelt et al., 2005; Mehlen and Puisieux, 2006) and the many details governing each step of the metastatic cascade remain poorly understood (Wirtz et al., 2011).

Breast cancer is a very heterogeneous disease that varies from each patient. This heterogeneity is classified clinically by staging systems and by the histopathologic grade. Differential expression of established prognostic and predictive biomarkers, and hormone receptors is the basis for targeted treatment. Currently, the focus of treatment relies mostly on inducing tumor cell apoptosis. However, there is growing evidence that demonstrates the importance of the tumor microenvironment in the development and progression of cancer, and consequently, emerging treatments have focused on targeting the tumor stroma (Condeelis and Pollard, 2006; Grivennikov, 2016)

To better understand cancer progression, there have been numerous *in vivo* animal and *in vitro* models developed to study cancer metastasis (Cekanova and Rathore, 2014; Denayer et al., 2014). While *in vivo* animal models better represent the complexity of the metastatic process, the visualization and characterization of this multi-step process is challenging. The need to improve our understanding of tumor progressions and metastasis has pushed for the improvement of *in vitro* tumor models. These *in vitro* models vary in complexity and incorporate different components of the tumor microenvironment to better approach physiological conditions. (Hulkower and Herber, 2011; Wirtz et al., 2011; Infanger et al., 2013; Vidi et al., 2013; DeVita Jr and Rosenberg, 2012).

Metastasis

Metastasis is the main cause of cancer related deaths, accounting for more than 90% of cancer mortality (Nguyen, Bos, and Massagué 2009). A complex series of sequential steps need to be completed to form a clinically detectable metastatic lesion at a distant organ (Valastyan and Weinberg 2011). These steps begin by the invasion of epithelial cells in a primary solid tumor into the local stroma, intravasation into the lumen of blood (or lymphatic) vessels, surviving during circulation, arrest at a secondary site, extravasation into the stroma, and re-initiation of proliferation at the secondary site.

Invasion into the surrounding stroma involves the breaching of the epithelium basement membrane (BM), which separates epithelial tissues from the adjacent extracellular components. The BM causes alterations in cell polarity, proliferation, invasiveness, and survival through a series of signaling pathways activated by cancer cells via integrin-mediated cell-matrix adhesion (Wolf and Friedl 2003; Bissell and Hines, 2011). Recent work indicates that the normal epithelium serves as an intrinsic barrier to invasion and dissemination. For example, in the mammary gland, myoepithelial cells are found to work as a dynamic barrier that restrains invasion and dissemination (Sirka et al., 2018).

Once the BM is breached, tumor cells encounter the stroma. Conventional models of cancer metastasis have described the process as the detachment of a single tumor cell from the primary tumor that is able to gain access to the circulation and seed a secondary site (Poste and Fidler, 1980; Fidler, 2003; Talmadge and Fidler, 2010). This single tumor cell model has been challenged by clinical observations of tumor cell clusters (also termed, “tumor microemboli”) in the blood of patients, and it has been correlated with poor patients’ outcomes (Hou et al., 2012; Aceto et al., 2014). Using a mouse model of highly metastatic breast cancer, we (and others) found that metastasis can occur through the invasion and dissemination of polyclonal tumor clusters that are able to seed secondary sites (Aceto et al., 2014; Cheung et al., 2016). Furthermore, we found that tumor cell clusters have > 100-fold metastatic potential compared to single tumor cells. These data provide evidence that tumor clusters can escape from primary tumors and seed secondary sites as multicellular groups of cells. Despite these intriguing observations, how tumor clusters are able to access the systemic circulation is still unknown.

The tumor microenvironment

Since 1889, when Stephen Paget proposed the “seeds” (cancer cells) and “soil” (microenvironment) hypothesis, research has been steered to the analysis of the tumor microenvironment (TME) that promotes tumor growth and metastasis (Paget, 1889; Hart and Fidler, 1980). Tumor cells secrete a plethora of grow factors, such as Transforming growth factor beta (TGF-β), Platelet-derived growth factor (PDGF), Vascular Endothelial Growth Factor (VEGF) and Epidermal Growth Factor (EGF), among others (Wolf and

Friedl, 2003; Hu et al., 2008). The tumor stroma can become “reactive”, acquiring wound healing or chronically inflamed traits (Grivennikov et al., 2010).

Tumors invade through this reactive stroma and encounter fibroblasts, adipocytes, endothelial cells, bone marrow-derived stem cells, macrophages and other immune cells (Joyce and Pollard, 2009). For example, the infiltration of white blood cells has been described as an important hallmark of cancer (Balkwill and Mantovani 2001). Studies have shown that leukocyte infiltration in breast cancer stimulates tumor invasiveness by the secretion of interleukin-6 (IL-6) by adipocytes present in the local microenvironment (Dirat et al., 2011). Tumor associated macrophages (TAMs) have been shown to promote invasion and dissemination of tumor cells and their presence in breast cancer has been associated with poor patient survival (Biswas and Mantovani, 2010). Fibroblasts are another predominant stromal cell type found throughout the tumor microenvironment which continuously remodel the ECM (Kalluri, 2016). These tumors associated fibroblast (CAFs) are considered to be pro-tumorigenic due to the secretion of several cytokines and growth factors like Fibroblast Growth Factor (FGF), PDGF, TGF-b, monocyte chemotactic protein 1 (MCP1) and many secreted proteases (Olumi et al. 1999; Kalluri and Zeisberg 2006).

The tumor vasculature

One of the hallmarks of cancer is tumor angiogenesis, which is essential to support rapid tumor growth. During early stages of tumor development, access to nutrients and oxygen is supplied by the pre-existing vasculature, termed "vessel co-option". However, once tumors grow beyond 1-2 mm., angiogenesis is triggered by the resulting hypoxic conditions, since the diffusion distance of oxygen has been measured to be 100-200 μm (Carmeliet and Jain, 2000). Tumors transition from a pre-vascular hyperplastic state to a hypervascularization state referred as the "angiogenic switch" (Bergers and Benjamin, 2003). Tumor cells induce the expression of hypoxia-inducible factor-1 (HIF-1) which promotes the expression of pro-angiogenic proteins, such as VEGF, EGF, FGF, hepatocyte growth factor (HGF), and PDGF, increasing the signals for neovascularization (Bergers and Benjamin, 2003; Itatani, 2018). The sustained expression of pro-angiogenic signals results in the development of a vasculature that is abnormal, with a tortuous structure, characterized by dilated vessels that show increased vascular permeability and high interstitial fluid pressure. This high interstitial fluid pressure further disrupts blood flow that eventually increase hypoxic conditions that helps sustain the balance toward pro-angiogenic factors (Maeda et al., 2000; Snuderl et al., 20013; Dvorak, 2002).

Tumor vasculature has also been shown to exhibit partial endothelial cell lining, a structure termed "mosaic vessels" (Chang et al., 2000). For example, analysis of tumor vasculature in histological sections of colon carcinoma xenografts showed that approximately 15% of the total vessels lacked complete endothelial coverage (Chang et al., 2000). Other studies, have shown evidence of vessels completely lacking endothelial cell lining, termed "vascular mimicry" (Hendrix et al., 2003). These vessels are described to be formed by the tumor itself and are characterized by the deposition of BM, vascular endothelial cadherin (VE-CAD), and the formation of connections with existing tumor vasculature (Hendrix et al., 2003; Hallani et al., 2010).

Abnormal angiogenesis in solid tumors not only results in structural defects but also in functional deficiencies (Folkman, 1995). These vessels are usually leaky, resulting in an heterogenous blood flow, and elevated interstitial fluid pressure (Fukumura and Jain, 2007). Solid tumors often show increased uptake and retentions of nanoparticles or high molecular weight probes, known as the enhanced permeability and retention (EPR) effect (Hashizume et al., 2000; Wong et al., 2015). Vessel functionality has been studied in animal models by measuring the permeability of fluorescent tracer molecules that are perfused through the vasculature.

The tumor vasculature shows low to moderate permeability in the order of 10^{-6} to 10^{-7} cm s^{-1} for albumin and 70-kDa dextran, respectively (Yuan, 1994). These studies are often limited to peripheral and/or ectopic tumor vasculature, where the vessel endothelium is largely intact. Nevertheless, intact tumor vasculature has been shown to have higher permeability to normal vasculature and has been shown to be leakier than normal vasculature, with defect cut-off sizes of 400–600 nm (Yuan, 1994). This leakiness is referred to as the enhanced permeation and retention (EPR) effect and it is widely used in the delivery of cancer therapeutics (Wong, 2015).

The 3D tumor microvasculature network has been studied using corrosion casts, creating replicas of the tumor vasculature from human colorectal cancers (Folarin et al., 2010). This study revealed that the tumor vasculature shows aberrant intervessel spacing, tortuosity, and diameter which changes from the periphery to the core of the tumor. Histological sections of tumor xenografts from different murine and human tumor cell lines have revealed intercellular defects up to 5 μm in size that enable the local extravasation of nanoparticles and red blood cells (Folarin et al., 2010).

Vascular structure and function could regulate the mode and frequency of intravasation by cancer cells and cancer cell clusters. Intravasation is a process that involves the entry of cancer cells into the lumen of lymphatic or blood vessels. Intravasation is facilitated by molecular changes that promote the ability of cancer cells to cross endothelial cell barriers. Evidence from intravital imaging suggests that intravasation is an active process that necessitates the disruption of the endothelium in a process term trans-endothelial migration (TEM; Harney, 2015). Other evidence points to intravasation as a passive process in which tumor cells and/or clusters are shed into the blood flow due to mechanical disruption of fragile vessel walls (Liotta, 1976).

Despite all these intriguing observations, little is known about the dynamics of tumor-vessel interactions and how it can influence the pathway for tumor cell entry into the cirluation. *In vivo* assays have been used to analyze the process of intravasation (Ref); however, the detailed mechanisms of the cell-cell interactions are difficult to analyze, and the dynamics are challenging to capture. The recent development of *in vitro* models that can recapitulate the complexities of the tumor microenvironment provide a platform to study these mechanisms that might shed light in the process of intravasation.

3D microvessel model to study tumor-vessel interactions

Numerous tumor mouse models have been developed that ranges from genetically engineered inducible models to human tumor xenografts (Cekanova and Rathore, 2014; Denayer et al., 2014). *In vivo* models provide the complexity of a living system, but visualization and the mechanism of individual steps remain difficult to analyze. In contrast, *in vitro* models can model many aspects of the tumor microenvironment, allowing us to study each step of the metastatic cascade while controlling for many variables and performing quantitative analysis.

Many in *vitro* models have been used to provide mechanistic insights in regard to tumor growth, invasion, dissemination, matrix remodeling, dormancy, intravasation, angiogenesis, and drug delivery. The complexity of the models depends on the objective of the study. For drug screening, 2D cell culture provides a low-cost platform; while studies of invasion and dissemination are performed with cells embedded in a matrix material (Shamir and Ewald, 2014). To analyze solid tumors, the use of 3D models better recapitulates cell-cell and cell-matrix interactions (Nguyen-Ngoc, 2015). Studies of tumor-vessel interactions and intravasation necessitate a microenvironment that incorporates perfusable microvessels. The microvessels used to study interactions between tumor cells and the tumor vasculature are fabricated by introducing endothelial cells within predefined ECM scaffolds within a matrix material (Bogorad et al., 2015).

In this study, we generated a cylindrical microvessel, with a diameter of 150-200 μm, using a template scaffold. These microvessels were developed by seeding endothelial cells within a predefined channel, surrounded by a collagen type I gel. Cells seeded on these ECM surfaces self-assembled into a continuous monolayer and were tested for functional properties, such as vessel permeability, expression of relevant junctional proteins (Chrobak et al., 2006). The advantages of these 3D cylindrical microvessels are that they exhibit a physiologically relevant geometry, can be maintained under constant flow and shear stress, and can be co-cultured with a variety of cell types. In a recent study, qualitative observations of invasion and intravasation using this 3D microvessel platform found that single tumor cell entry into the vasculature is mediated by tumor cell division at the ECM–vessel interface resulting in the disruption of the endothelial monolayer (Wong and Searson, 2014).

To study the cellular dynamics of tumor-vessel interactions we used a 3D tumor-microvessel model that incorporated a functional vasculature within an extracellular matrix material as mentioned above. This reductive model combined both a perfusable microvessel with freshly isolated mammary gland tumor organoids that were embedded into collagen-I gels (Wong and Searson, 2014). In this way, we were able to recapitulate both the microvessel cylindrical geometry, endothelium-matrix interactions, shear stress and flow, with the 3D structure of tumors (Nguyen-Ngoc et. al, 20015). This approach offered us the advantage of being able to monitor tumor-vessel interactions in real time, using live cell imaging, partially recapitulating the spatial organization and structure of the tumor microenvironment.

In this study, we were able to model three types of tumor-vessel interactions: mosaic vessel, vessel constriction and vessel pull, each of which may have important implications for metastasis. We speculate that tumors that generate sufficient force on the endothelium to disrupt endothelial cell-cell junctions could enable the formation of mosaic vessel structures which may facilitate shedding of CTCs and/or CTMs exposed to the vessel flow without the need of TEM. While vessel constriction may give rise to other vascular defects such as dead-ends, vessel pull could be a mechanism used by highly adherent tumor cells to co-opt pre-existing vessels. Additionally, the state of the endothelium may contribute to the formation of any of these tumor-vessel structures. For example, if the endothelium had a net increase in cell death rate, it could facilitate the integration of tumors within the vasculature. On the other hand, if the rate of proliferation was higher and the overall state of the vessel was intact, tumors could interact with the endothelium by constricting or pulling on the vessel wall. Our experimental approach enables a convenient way to study multiple steps in the metastatic cascade that are otherwise very difficult to observe *in vivo*. Moreover, this tumor-microvessel model could also be adapted and customized to reflect other aspects of the tumor microenvironment to further study the metastatic process.

References

Aceto, N., A. Bardia, D.T. Miyamoto, M.C. Donaldson, B.S. Wittner, J.A. Spencer, M. Yu, A. Pely, A. Engstrom, H. Zhu, B.W. Brannigan, R. Kapur, S.L. Stott, T. Shioda, S. Ramaswamy, D.T. Ting, C.P. Lin, M. Toner, D.A. Haber, and S. Maheswaran. 2014. Circulating tumor cell clusters are oligoclonal precursors of breast cancer metastasis. *Cell*. 158:1110-1122.

Balkwill, F., and A. Mantovani. 2001. Inflammation and cancer: back to Virchow? *Lancet.* 357:539-545.

Bergers, G., and L.E. Benjamin. 2003. Tumorigenesis and the angiogenic switch. *Nature reviews. Cancer. 3*:401-410.

Bissell, M.J., and W.C. Hines. 2011. Why don't we get more cancer? A proposed role of the microenvironment in restraining cancer progression. *Nat Med.* 17:320-329.

Biswas, S.K., and A. Mantovani. 2010. Macrophage plasticity and interaction with lymphocyte subsets: cancer as a paradigm. *Nature immunology*. 11:889-896.

Bogorad, M.I., J. DeStefano, A.D. Wong, and P.C. Searson. 2017. Tissue-engineered 3D microvessel and capillary network models for the study of vascular phenomena. *Microcirculation.* 24.

Carmeliet, P., and R.K. Jain. 2000. Angiogenesis in cancer and other diseases. *Nature*. 407:249-257.

Cekanova, M., and K. Rathore. 2014. Animal models and therapeutic molecular targets of cancer: utility and limitations. *Drug Des Devel Ther*. 8:1911-1921.

Chang, Y.S., E. di Tomaso, D.M. McDonald, R. Jones, R.K. Jain, and L.L. Munn. 2000. Mosaic blood vessels in tumors: frequency of cancer cells in contact with flowing blood. *Proceedings of the National Academy of Sciences of the United States of America*. 97:14608-14613.

Cheung, K.J., V. Padmanaban, V. Silvestri, K. Schipper, J.D. Cohen, A.N. Fairchild, M.A. Gorin, J.E. Verdone, K.J. Pienta, J.S. Bader, and A.J. Ewald. 2016. Polyclonal breast cancer metastases arise from collective dissemination of keratin 14-expressing tumor cell clusters. *Proceedings of the National Academy of Sciences of the United States of America.* 113:E854-863.

Chrobak, K.M., D.R. Potter, and J. Tien. 2006. Formation of perfused, functional microvascular tubes in vitro. *Microvasc Res.* 71:185-196.

Condeelis, J., and J.W. Pollard. 2006. Macrophages: obligate partners for tumor cell migration, invasion, and metastasis. *Cell*. 124:263-266.

Denayer, T., Stöhr, T., and Vanroy, M. 2014. Animal models in translational medicine: validation and prediction. *New Horiz. Transl. Med*. 2: 5–11.

DeVita, V.T., Jr., and S.A. Rosenberg. 2012. Two hundred years of cancer research. *N Engl J Med.* 366:2207-2214.

Dirat, B., L. Bochet, M. Dabek, D. Daviaud, S. Dauvillier, B. Majed, Y.Y. Wang, A. Meulle, B. Salles, S. Le Gonidec, I. Garrido, G. Escourrou, P. Valet, and C. Muller. 2011. Cancer-associated adipocytes exhibit an activated phenotype and contribute to breast cancer invasion. *Cancer Res*. 71:2455-2465.

Dvorak, H.F. 2002. Vascular permeability factor/vascular endothelial growth factor: a critical cytokine in tumor angiogenesis and a potential target for diagnosis and therapy. *J Clin Oncol*. 20:4368-4380.

Fidler, I.J. 2003. The pathogenesis of cancer metastasis: the "seed and soil" hypothesis revisited. *Nat Rev Cancer*. 3(6): 453–458.

Folarin, A.A., M.A. Konerding, J. Timonen, S. Nagl, and R.B. Pedley. 2010. Three-dimensional analysis of tumour vascular corrosion casts using stereoimaging and micro-computed tomography. *Microvasc Res*. 80:89-98.

Folkman, J. 1995. Angiogenesis in cancer, vascular, rheumatoid and other disease. *Nat Med.* 1:27-31.

Folkman, J., and R. Kalluri. 2004. Cancer without disease. *Nature*. 427:787.

Friedl, P., and K. Wolf. 2003. Proteolytic and non-proteolytic migration of tumour cells and leucocytes. *Biochem Soc Symp*:277-285.

Fukumura, D., and R.K. Jain. 2007. Tumor microvasculature and microenvironment: targets for anti-angiogenesis and normalization. *Microvasc Res*. 74:72-84.

Grivennikov, S.I., and M. Karin. 2010. Inflammation and oncogenesis: a vicious connection. *Curr Opin Genet Dev*. 20:65-71.

Harney, A.S., E.N. Arwert, D. Entenberg, Y. Wang, P. Guo, B.Z. Qian, M.H. Oktay, J.W. Pollard, J.G. Jones, and J.S. Condeelis. 2015. Real-Time Imaging Reveals Local, Transient Vascular Permeability, and Tumor Cell Intravasation Stimulated by TIE2hi Macrophage-Derived VEGFA. *Cancer Discov*. 5:932-943.

Hart, I.R., and I.J. Fidler. 1980. Role of organ selectivity in the determination of metastatic patterns of B16 melanoma. *Cancer Res*. 40:2281-2287.

Hashizume, H., et al. 2000. Openings between defective endothelial cells explain tumor vessel leakiness. *Am J Pathol,* 156:1363-80.

Hendrix, M.J., E.A. Seftor, A.R. Hess, and R.E. Seftor. 2003. Vasculogenic mimicry and tumour-cell plasticity: lessons from melanoma. Nature reviews. Cancer. 3:411-421.S. El Hallani, B. Boisselier, F. Peglion, A. Rousseau, C. Colin, A. Idbaih, Y. Marie, K. Mokhtari, J.L. Thomas, A. Eichmann, et al. 2010. A new alternative mechanism in glioblastoma vascularization: tubular vasculogenic mimicry. *Brain*, 133, pp. 973-982

Hou, JM, et al. 2012. Clinical significance and molecular characteristics of circulating tumor cells and circulating tumor microemboli in patients with small-cell lung cancer. *J Clin Oncol*. 30(5):525–532.

Infanger, D. W., Cho, Y., Lopez, B. S., Mohanan, S., Liu, S. C., Gursel, D., et al. 2013. Glioblastoma stem cells are regulated by interleukin-8 signaling in a tumoral perivascular niche. Cancer Res. 73, 7079–7089.

Hulkower, K. I., and Herber, R. L. 2011. Cell migration and invasion assays as tools for drug discovery. *Pharmaceutics* 3, 107–124.

Itatani, Y., K. Kawada, T. Yamamoto, and Y. Sakai. 2018. Resistance to Anti-Angiogenic Therapy in Cancer-Alterations to Anti-VEGF Pathway. *Int J Mol Sci*. 19.

Joyce, J.A., and J.W. Pollard. 2009. Microenvironmental regulation of metastasis. *Nature reviews. Cancer.* 9:239-252.

Kalluri, R., and E. Zeisberg. 2006. Controlling angiogenesis in heart valves. *Nat Med*. 12:1118-1119.

Kalluri R., 2016. The biology and function of fibroblasts in cancer. *Nat. Rev. Cancer*. 16:582-598.

Liotta, L.A., M.G. Saidel, and J. Kleinerman. 1976. The significance of hematogenous tumor cell clumps in the metastatic process. *Cancer Res*. 36:889-894.

Maeda, H., J. Wu, T. Sawa, Y. Matsumura, and K. Hori. 2000. Tumor vascular permeability and the EPR effect in macromolecular therapeutics: a review. *J Control Release*. 65:271-284.

Mehlen, P., and A. Puisieux. 2006. Metastasis: a question of life or death. *Nature reviews. Cancer*. 6:449-458.

Nguyen-Ngoc, K.V., E.R. Shamir, R.J. Huebner, J.N. Beck, K.J. Cheung, and A.J. Ewald. 2015. 3D culture assays of murine mammary branching morphogenesis and epithelial invasion. *Methods in molecular biology (Clifton, N.J.)*. 1189:135-162.

Nguyen, D.X., A.C. Chiang, X.H. Zhang, J.Y. Kim, M.G. Kris, M. Ladanyi, W.L. Gerald, and J. Massague. 2009. WNT/TCF signaling through LEF1 and HOXB9 mediates lung adenocarcinoma metastasis. *Cel*l. 138:51-62.

Olumi, A.F., G.D. Grossfeld, S.W. Hayward, P.R. Carroll, T.D. Tlsty, and G.R. Cunha. 1999. Carcinoma-associated fibroblasts direct tumor progression of initiated human prostatic epithelium. Cancer Res. 59:5002-5011.

Paget, S. 1889. The distribution of secondary growths in cancer of the breast. *Cancer Metastasis Rev*. 8:98-101.

Poste, G., Fidler, I.J. 1980. The pathogenesis of cancer metastasis. *Nature*. 283(5743):139-146.

Shamir, E.R., and A.J. Ewald. 2014. Three-dimensional organotypic culture: experimental models of mammalian biology and disease. *Nature reviews. Molecular cell biology*. 15:647-664.

Sirka, O.K., E.R. Shamir, and A.J. Ewald. 2018. Myoepithelial cells are a dynamic barrier to epithelial dissemination. *The Journal of cell biology*. 217:3368-3381.

Snuderl, M., A. Batista, N.D. Kirkpatrick, C. Ruiz de Almodovar, L. Riedemann, E.C. Walsh, R. Anolik, Y. Huang, J.D. Martin, W. Kamoun, E. Knevels, T. Schmidt, C.T. Farrar, B.J. Vakoc, N. Mohan, E. Chung, S. Roberge, T. Peterson, C. Bais, B.H. Zhelyazkova, S. Yip, M. Hasselblatt, C. Rossig, E. Niemeyer, N. Ferrara, M. Klagsbrun, D.G. Duda, D. Fukumura, L. Xu, P. Carmeliet, and R.K. Jain. 2013. Targeting placental growth factor/neuropilin 1 pathway inhibits growth and spread of medulloblastoma. *Cell*. 152:1065-1076.

Su, S., Q. Liu, J. Chen, J. Chen, F. Chen, C. He, D. Huang, W. Wu, L. Lin, W. Huang, J. Zhang, X. Cui, F. Zheng, H. Li, H. Yao, F. Su, and E. Song. 2014. A positive feedback loop between mesenchymal-like cancer cells and macrophages is essential to breast cancer metastasis. *Cancer Cell*. 25:605-620.

Talmadge, J.E, Fidler, I.J. 2010. AACR centennial series: the biology of cancer metastasis: historical perspective. *Cancer Res*. 70(14): 5649–5669.

Valastyan, S., and R.A. Weinberg. 2011. Tumor metastasis: molecular insights and evolving paradigms. *Cell*. 147:275-292.

Vidi, P. A., Bissell, M. J., and Lelievre, S. A. 2013. Three-dimensional culture of human breast epithelial cells: the how and the why. *Methods Mol. Biol.* 945, 193–219.

Wang, X.Y., Y. Pei, M. Xie, Z.H. Jin, Y.S. Xiao, Y. Wang, L.N. Zhang, Y. Li, and W.H. Huang. 2015. An artificial blood vessel implanted three-dimensional microsystem for modeling transvascular migration of tumor cells. *Lab Chip*. 15:1178-1187.

Weigelt, B., C.K. Ng, R. Shen, T. Popova, M. Schizas, R. Natrajan, O. Mariani, M.H. Stern, L. Norton, A. Vincent-Salomon, and J.S. Reis-Filho. 2015. Corrigendum:

metastatic breast carcinomas display genomic and transcriptomic heterogeneity. *Mod Pathol*. 28:607.

Wirtz, D., K. Konstantopoulos, and P.C. Searson. 2011. The physics of cancer: the role of physical interactions and mechanical forces in metastasis. *Nature reviews. Cancer*. 11:512-522.

Wong, A.D., and P.C. Searson. 2014. Live-cell imaging of invasion and intravasation in an artificial microvessel platform. *Cancer Res*. 74:4937-4945

Wong, A.D., M. Ye, M.B. Ulmschneider, and P.C. Searson. 2015. Quantitative Analysis of the Enhanced Permeation and Retention (EPR) Effect. *PLoS One*. 10:e0123461.

Yuan, F., H.A. Salehi, Y. Boucher, U.S. Vasthare, R.F. Tuma, and R.K. Jain. 1994. Vascular permeability and microcirculation of gliomas and mammary carcinomas transplanted in rat and mouse cranial windows. *Cancer Res*. 54:4564-4568.

CHAPTER 2

Mosaic loss of non-muscle myosin IIA and IIB is sufficient to induce mammary epithelial proliferation

(Modified from Nguyen-Ngoc, K.V.*, V.L. Silvestri*, D. Georgess, A.N. Fairchild, and A.J. Ewald. 2017. Mosaic loss of non-muscle myosin IIA and IIB is sufficient to induce mammary epithelial proliferation. *Journal of Cell Science*. 130:3213-3221)

Abstract

The mammary epithelium elaborates through hormonally-regulated changes in proliferation, migration, and differentiation. Non-muscle myosin II (NMII) functions at the interface between contractility, adhesion, and signal transduction. It was therefore a plausible regulator of mammary morphogenesis. We tested the genetic requirement for NMIIA and NMIIB through deletion of the myosin heavy chains (*NMHC*) that confer specificity to the complex. Surprisingly, mosaic loss, but not ubiquitous loss, of *NMHCIIA* and *IIB* induced high levels of proliferation in 3D culture. This phenotype was observed even in basal media conditions that do not support tissue level growth of wildtype epithelium. Mosaic loss of NMIIA and IIB combined with FGF signaling to induce hyperplasia. Mosaic analysis revealed that both NMIIA,B-null and wild-type cells proliferated, indicating that the regulation of proliferation is both cell autonomous and non-autonomous within epithelial tissues. This phenotype appears mediated by cell-cell contact, as co-culture did not induce proliferation. Mosaic loss of NMIIA and IIB also induced excess proliferation *in vivo*. Our data therefore reveal a role for NMIIA and NMIIB as negative regulators of proliferation in the mammary epithelium.

Introduction

Cell proliferation and tissue architecture need to be tightly regulated to ensure normal development and homeostasis. Excessive proliferation is a hallmark of cancer and can be induced by constitutive activation of mitogenic signals, inactivation of growth suppressors, or escape from contact inhibition of proliferation (Hanahan and Weinberg, 2011). For example, loss of the cadherin/catenin complex can induce uncontrolled proliferation and tumor growth (Jeanes et al., 2008). However, most genetic studies of proliferation have been conducted in conventional 2D cell culture, which only partially recapitulate the structure and dynamics of epithelial tissues. The molecular mechanism by which cells sense and regulate proliferation in three-dimensional (3D) tissues remains incompletely understood.

Non-muscle myosin II (NMII) is expressed in most cell types and plays an essential role in diverse cellular processes including contractility, adhesion, cytokinesis, migration, and signal transduction (Lecuit and Yap, 2015; Ma and Adelstein, 2014). NMII exists in three isoforms: NMIIA, NMIIB, and NMIIC. Each NMII isoform is composed of three pairs of proteins: two regulatory light chains, two essential light chains, and two heavy chains (Vicente-Manzanares et al., 2009). The specificity of the NMII complex is determined by the identity of the heavy chain, which in mammals can be encoded by three genes: NMII heavy chains A, B, and C (*NMHC IIA, IIB, IIC*). NMII molecules bind to and crosslink the actin cytoskeleton to form networks of actomyosin filaments, which support cell architecture and function (Vicente-Manzanares et al., 2009). In single cell migration, NMII molecules orchestrate integrin-mediated adhesion to extracellular matrix (ECM) substrates (Choi et al., 2008) to ensure directional movement (Yam et al., 2007). In multicellular systems, such as epithelia, NMIIs are required for the establishment and maintenance of apical junctions in early developing tissues, such as the visceral endoderm (Conti et al., 2004) and the spinal neuroepithelium (Ma et al., 2007) and in mature organs such as the epidermis (Sumigray et al., 2012).

Using a variety of genetic tools, including isoform specific ablation and replacement, Adelstein and colleagues have discovered both specific and redundant functions of NMII isoforms (Ma and Adelstein, 2014). For example, NMIIA and NMIIB are interchangeable in regulating spinal neuroepithelial intercellular junctions (Ma et al., 2007) whereas NMIIA is uniquely required for mouse placental blood vessel formation, and NMIIB is uniquely required for neuronal cell migration (Ma et al., 2004). Exchanging the two isoforms only partially rescues organ defects in the non-redundant cases. Distinct molecular functions of NMIIA and NMIIB have also been found during the spatio-temporal regulation of E-cadherin-based junction in epithelial sheets (Smutny et al., 2010). These findings demonstrate the importance of NMII molecules in epithelial tissue architecture and function, and also stimulate questions about how loss of NMII could disrupt tissue homeostasis and promote pathogenesis.

Disruption of NMII-mediated cellular contractility is associated with diverse diseases, including cancer. Cell adhesion to the ECM activates myosin and Rho/ROCK signaling, enabling NMII to mediate both extracellular adhesion and mechanical signals and thereby affect cell behavior (Vicente-Manzanares et al., 2009). Recent studies have also discovered multiple roles for NMII in cancer. For example, sustained elevation of NMII-mediated cellular tension in response to increasing matrix stiffness and rigidity can promote cell proliferation and tumorigenesis (DuFort et al., 2011). NMIIA and NMIIB have distinct roles in force generation and nuclear translocation during cancer invasion (Thomas et al., 2015). Finally, inducible expression of p190-B Rho GTPase disrupted mammary tissue architecture resulting in increased cell proliferation (Vargo-Gogola et al., 2006). In contrast, reduced contractility due to loss of NMIIA in a tumor susceptible background promotes cell proliferation and metastasis in squamous cell carcinoma (Schramek et al., 2014). This emerging evidence indicates that NMIIA can be a tumor suppressor; however, the genetic consequences of NMII loss in the normal mammary epithelium remain unclear.

Here we sought to understand the role of NMII in epithelial organization and development, using the mammary epithelium as a model system. We combined 3D culture of primary epithelial organoids with adenoviral delivery of Cre-recombinase (Ad-Cre) and time-lapse imaging to reveal the cellular consequence of NMII deletion in mammary epithelium. Surprisingly, we found that mosaic deletion of NMIIA and NMIIB is sufficient to induce epithelial tissue growth and cell proliferation.

Results

Isoform specific deletion of NMII in mammary organoids

The mammary epithelium consists of two major cell types: an inner luminal epithelial cell layer, surrounded by a basally-positioned myoepithelial cell layer. We first examined the expression and localization of NMII isoforms A, B, and C within these epithelial populations using both *NMIIA-GFP* and *NMIIB-GFP* knock-in mice and immunofluorescent staining to detect endogenous proteins. Consistent with previous reports (Beach et al., 2011), NMIIA was expressed in both luminal and myoepithelial cells, NMIIB was predominantly observed in myoepithelial cells and at low levels near the apical limit of the luminal cell membranes, and NMIIC was restricted to the luminal epithelial cell layer (Supplemental Figure 2-1 A-C).

To study the consequences of loss of NMII in the mammary epithelium, we used Ad-Cre to delete the *NMHCIIA* and *NMHCIIB* genes in primary mammary organoids, which are fragments of primary epithelial ducts embedded within 3D ECM gels (Matrigel; Figure 2-1 1A). In these assays, organoids will not grow in basal medium without supplemental growth factor addition (No GF) and will undergo branching morphogenesis in response to FGF2 (Ewald et al., 2008; Nguyen-Ngoc et al., 2015). Since the heavy chain confers the specificity of the NMII complex, we refer to the deletion of *NMHCIIA* and *NMHCIIB* and loss of NMIIA and NMIIB interchangeably.

We isolated mammary epithelial organoids from mice carrying floxed *NMHCIIA* and *NMHCIIB* alleles, and a ubiquitously expressed tamoxifen-inducible Cre recombinase

(*Cre-ER;NMIIA*$^{fl/fl}$*;NMIIB*$^{fl/fl}$). Organoids from the same mouse were initially evaluated in three groups: control (Untreated), Ad-Cre and tamoxifen (Tam) treatments in basal medium. Infections with Ad-Cre were designed to yield Cre expression in 50-75% of cells (Badea et al., 2003; Shamir et al., 2014). We refer to the organoids treated with Ad-Cre as mosaic NMIIA,B-null organoids. Tamoxifen induced Cre-ER activity resulted in recombination in essentially all cells. Western blotting confirmed the loss of NMIIA and NMIIB proteins in Tam treated organoids, and a reduction in both proteins in the Ad-Cre treatment group, while NMIIC protein levels remained unchanged in both treatments (Figure 2-1 B-C). To analyze the effects of loss of NMIIA and IIB in mammary epithelial organoid growth, we measured the fold increase in projected surface area of organoids at day 5 divided by day 0 in culture. We observed a significant increase in growth of mosaic organoids compared to control and Tam treatment, respectively (Figure2-1 1D and Supplemental Figure 2-2 A,C,D). In contrast, control and Tam did not show significant increase in tissue size. To control for the effects of adenoviral infection, we separately evaluated the consequences of Ad-GFP infection and found no effect on tissue growth (Supplemental Figure 2-2 B,G). To control for the effects of Tam on tissue growth, we isolated mammary epithelial organoids from wild-type mice not carrying loxP-flanked *NMHCIIA* and *NMHCIIB* alleles and treated with 50nM Tam. At the dose used, Tam did not have an effect on organoid growth (Figure 2-1 1D and Fig. Supplemental Figure 2-2 E-G). These data suggest that NMII is negatively regulating tissue growth.

Mosaic loss of both NMIIA and NMIIB is sufficient to induce hyperproliferation in the mammary epithelium

We investigated the consequences of loss of NMIIA and/or NMIIB in basal medium conditions (Nguyen-Ngoc et al., 2015). Control epithelial organoids typically maintained their size (Figure 2-1 E). Deletion of two or three alleles of the *NMHCIIA* and *NMHCIIB* genes did not grossly affect organoid size (Figure 2-1 F-J). In contrast, mosaic deletion of all four alleles of *NMHCIIA* and *NMHCIIB* genes resulted in tissue growth (Figure 2-1 K and Figure 2-2 A). Strikingly, complete deletion of NMIIA and NMIIB in the Tam treated organoids did not affect organoid growth, while mosaic deletion with Ad-Cre resulted in large increase in organoid projected surface area by day 5 in culture (Figure 2-1 D and Supplemental Figure 2-2 C,G). Consistent with this level of tissue growth, mosaic NMIIA,B-null organoids had a higher mitotic index than control organoids, as assayed by phospho-Histone H3 staining (pH3, Figure 2-2 B-D). Taken together, these data indicate that loss of NMIIA and NMIIB in a mosaic subset of cells is sufficient to induce extensive proliferation in the mammary epithelium, even in basal medium conditions.

Mosaic loss of NMIIA and NMIIB combined with exogenous FGF2 induces hyperplasia

During puberty, mammary epithelial cells undergo branching morphogenesis in response to proliferative signals mediated through steroid hormones and growth factors (Sternlicht et al., 2006). We have previously shown that this process can be modeled through addition of nanomolar concentrations of FGF2 in our "branching" assay (Ewald et al., 2008; Nguyen-Ngoc et al., 2015). Addition of FGF2 in control organoids induced cell division and resulted in the formation of branched epithelial structures (Supplemental Figure 2-2 H), with a corresponding increase in projected surface area relative to initial size (~4 fold, Figure 2-2 E). Deletion of 1-3 alleles of *NMHCIIA* and *NMHCIIB* genes correlated with a non-significant reduction in tissue growth and was compatible with relatively normal branching (Supplemental Figure 2-2 I-M). In contrast, mosaic deletion of all four alleles in FGF2 treated organoids led to a significant increase in tissue growth (~9 fold), inferred from the change in projected surface area of organoids in time-lapse movies (Figure 2-2 E and Supplemental Figure 2-2 N). Consistent with the tissue growth in time-lapse movies, mosaic NMIIA,B-null organoids had a higher mitotic index than control organoids, as assayed by pH3 staining (Figure 2-2 F-H). These data demonstrate that loss of both NMIIA and NMIIB, combined with growth factor signaling, further promote excess proliferation. Taken together, we conclude that NMIIA and NMIIB cooperatively serve as negative regulators of proliferation within the mammary epithelium.

Mosaic loss of NMIIA and NMIIB induce both cell autonomous and non-autonomous proliferation within the mammary epithelium

We next asked whether the excess proliferation was limited to NMIIA,B-null cells. To address this question, we introduced a convertible double-fluorescent Cre reporter into the floxed myosin II line, $NMIIA^{fl/fl}$;$NMIIB^{fl/fl}$;*mTmG*. In this model, all cells constitutively express membrane-localized tdTomato (red fluorescence) and, upon Ad-Cre treatment, switch heritably to expression of membrane-localized green fluorescent protein (GFP). Therefore, green fluorescence serves as a direct reporter for Cre activity and an indirect reporter for *NMHCIIA* and *NMHCIIB* genes deletion. $NMIIA^{fl/fl}$;$NMIIB^{fl/fl}$;*mTmG* organoids were treated with Ad-Cre to generate a mixture of red and green cells. Mosaic organoids were then embedded in 3D Matrigel in basal medium. This strategy allowed us to identify which population of cells, wild-type (red, Cre-) or NMIIA,B-null (green, Cre+), contributed to the overgrowth phenotype (Figure 2-3 A).

Since we observed a significant increase in proliferation in Ad-Cre treated organoids by 70-80 hours in culture (Figure 2-2 A), we collected fluorescent confocal z-stack images at day 3 and day 5 (Figure 2-3 B,D). To calculate the contributions of wild-type and NMIIA,B-null cells, we measured the total volume of each population of cells for each mosaic organoid at day 3 (initial volume) and day 5 (final volume) of culture using 3D surface rendering (Figure 2-3 C,E). Using initial and final surface-rendered volumes of wild-type and NMIIA,B-null cells (Figure 2-3 F,G), we calculated and compared growth rates. We found that the % change in volume for NMIIA,B-null cells was 101.5% compared to 41% for wild-type cells (Figure 2-3 H). Time-lapse movies also confirmed that the increase in volume was due to increased cell proliferation and not cell growth (Supplemental Figure 2-3 A-C). We validated successful completion of cytokinesis by evaluating cell shapes in 3D in confocal time-lapse movies and speculate that it could be accomplished due to residual NMIIC (Figure 2-1 B). We conclude that loss of NMIIA and NMIIB induce both cell autonomous and non-autonomous proliferation in mammary epithelium.

Hyperproliferation induced by mosaic loss of NMIIA and NMIIB is not mediated by soluble factors

Having demonstrated that wildtype and NMIIAB-null cells proliferate in response to mosaic loss of NMIIA and IIB within an organoid, we next sought to determine whether this effect was mediated by soluble factors. To test this hypothesis, we used the *NMIIA*$^{fl/fl}$*;NMIIB*$^{fl/fl}$*;mTmG* line to generate both wild-type (containing only red cells) and Ad-Cre treated organoids (mixture of red and green cells) for mosaic NMIIA,B deletion as previously described. We then co-cultured wild-type and mosaic organoids in a 1:1 ratio in 3D Matrigel with basal medium (Figure 2-4 A). Confocal microscopy images were taken at day 5 in culture (Figure 2-4 B-D). To analyze differences in growth, we measured the projected area of organoids in co-culture compared to wild-type (control) and mosaic (control) organoids, respectively. We observed a consistent and significant 2.5-fold increase in growth of mosaic organoids in both monoculture and co-culture, relative to wild-type (Figure 2-4 E). In contrast, wild-type organoids essentially did not increase in size in either monoculture or co-culture (Figure 2-4 E). Taken together, these data suggest that the hyperproliferation caused by mosaic deletion of NMIIA and NMIIB in mammary organoids is not mediated by soluble factors but is instead likely mediated by cell-cell contact.

NMIIA,B deletion increases sporadic cell proliferation in epithelial ducts *in vivo*

Our genetic analysis in 3D culture revealed that mosaic loss of NMIIA,B resulted in excess proliferation in both wild-type and NMIIA,B-null cells. We next tested the consequences of NMIIA,B deletion in polarized mammary epithelium *in vivo*. We isolated and orthotopically transplanted organoids from *Cre-ER;NMIIA$^{fl/fl}$;NMIIB$^{fl/fl}$;mTmG* and *CreER;NMIIA$^{fl/+}$;mTmG* (control) mice into the cleared mammary fat pad of nonfluorescent host mice. We allowed six weeks for ductal network formation, then induced NMIIA,B deletion by tamoxifen injection and, waited an additional six weeks before collecting mammary glands (Supplemental Figure 2-4 A) to assay proliferation by pH3 staining. Similar to the organoids cultured in basal medium without additional growth factors, control epithelium contained very few pH3+ mitotic cells (Supplemental Figure 2-4 B-C). In contrast, epithelium where NMIIA and NMIIB were deleted displayed an increased number of mitotic cells (Supplemental Figure 2-4 B'-C'). We calculated the number of proliferative cells per 40x field of view and observed a statistically significant increase following loss of NMIIA and NMIIB (Supplemental Figure 2-4 D). Finally, proliferation was observed in both red (Cre-) and green (Cre+) cells demonstrating that the effect of NMIIA,B deletion on proliferation was also both cell autonomous and non-autonomous *in vivo* (Supplemental Figure 2-4 E'-G). The magnitude of the increase in proliferation and the associated disruption of epithelial architecture were both smaller *in vivo* compared to *in vitro*. We speculate that this difference is due to the presence of additional negative regulators of proliferation, to differences in the extent of mosaicism in the epithelium, or to differential protein stability.

Discussion

Our genetic analysis of NMII was motivated by previous pharmacologic studies in which inhibition of myosin activity disrupted branching morphogenesis in multiple organs (Daley et al., 2009; Ewald et al., 2008; Meyer et al., 2006; Michael et al., 2005; Moore et al., 2005). Our data support the concept that NMII can function as a negative regulator of proliferation. NMII mediated tension regulates the establishment and dynamics of intercellular junctions (Smutny et al., 2010) and loss of junctional components such as E-Cadherin (Derksen et al., 2006) accelerates mammary tumor progression. Cell tension derived from NMII-based contractility is required to support these adhesion complexes and also responds to the forces generated by adjacent cells and the ECM (Lecuit and Yap, 2015). Therefore, either an elevation or reduction of myosin activity could change cell behavior and tissue organization. We therefore speculate that mosaic but not ubiquitous loss of NMII isoforms could induce proliferation by destabilizing intercellular junctions or disrupting mechanotransduction.

NMIIA and NMIIB are essential for multiple functions at the cell and tissue level, and so deletion of all four alleles may be statistically unlikely in cancer cells. However, a similar heterogeneity in myosin activity across the tissue could be achieved through clonal loss of myosin inhibitors or clonal gain of activators. These mechanisms would phenocopy the effect of NMIIA,B deletion in a subset of cells and could drive clonal fixation in either the myosin-deficient or neighboring myosin-normal cells. As an example, overexpression of p190-RhoB induced hyperplasia in the mammary epithelium (Vargo-Gogola et al., 2006). Given the ubiquity of disruptions in Rho GTPase signaling in human cancer (Sahai and Marshall, 2002; Vega and Ridley, 2008), we speculate that heterogeneity in myosin levels between neighboring cells could be a major driver of cancer cell proliferation.

Materials and methods

Mouse strains

The NMIIA$^{fl/fl}$, NMIIB$^{fl/fl}$, NMIIA-GFP and NMII-GFP knock-in mouse lines (Jacobelli et al., 2010; Ma et al., 2009) were a gift from R. Adelstein (National Heart, Lung, and Blood Institute, NIH, Bethesda, MD). The *R26::Cre-ER* mouse line was a gift of J. Nathans (Johns Hopkins University; Baltimore, MD). The *FVB/NJ*, *mT/mG* (Muzumdar et al., 2007) and NOD.Cg-*Prkdcscid Il2rgtm1Wjl/SzJ* (NSG) mouse lines were acquired from the Jackson Laboratory. Mouse husbandry and procedures were all conducted according to an animal protocol approved by the Johns Hopkins University School of Medicine Institutional Animal Care and Use Committee.

3D culture assays of primary mammary epithelial organoids

We used a combined mechanical and enzymatic digestion using collagenase (C2139; Sigma-Aldrich) and trypsin (27250-018; Gibco Life Technologies), followed by differential centrifugation to isolate groups of mammary epithelial ducts, termed organoids, as previously described (Ewald et al., 2008; Nguyen-Ngoc et al., 2015). Organoids were then embedded in 3D Matrigel™ (354230; Corning) at 2-3 organoids/µL as 150 µL suspensions in a 24-well multiwell glass bottom plate (662892; Greiner Bio-One) or 2-well chamber coverglass (155379; ThermoFisher Scientific). Gels were allowed to polymerize for 30 minutes at 37°C and then cultured in minimal medium: DMEM/F12 (10565-018, Gibco), 1% v/v insulin, transferrin, selenium (51500, ThermoFisher) and 1% v/v penicillin/streptomycin (15140-122, Gibco). Basal medium conditions (No GF) refer to organoids embedded in growth factor-reduced Matrigel and cultured in minimal medium without the addition of supplemental growth factors. For branching morphogenesis assay, minimal medium is supplemented with 2.5 nM FGF2 (F0291, Sigma).

Tamoxifen-inducible Cre-mediated deletion in 3D culture

Cre activity was induced in *Cre-ER;NMIIA$^{fl/fl}$;NMIIB$^{fl/fl}$;mT/mG* mammary epithelium by culturing organoids embedded in 3D Matrigel with 50 nM tamoxifen (T5648; Sigma-Aldrich) for 18 hours. Cultures were then rinsed with PBS to wash out tamoxifen and incubated in fresh organoid medium for 5 days at 37°C. The tamoxifen-inducible system resulted in Cre activity in essentially all cells but did not have obvious morphological consequences for wildtype organoids.

Adenoviral gene delivery

As previously described (Huebner et al., 2016; Shamir et al., 2014), prior to embedding in 3D Matrigel, organoids were infected with Adenoviral-GFP or Adenoviral-CMV-Cre (Vector BioLabs) at the ratio of ~10^7 PFU per 1000 organoids. Infections were conducted in 50 µL DMEM for 1.5 hours at 37°C. Following viral treatment, organoids were washed twice in DMEM-F12 and suspended in Matrigel as previously described.

Orthotopic transplantation to mammary fat pad

For transplantation of mammary organoids followed by induction of gene deletion, we isolated and incubated organoids overnight at 37°C in organoid medium with 2.5 nM FGF2 in HydroCell 96-well microplates (174907, Thermo Fisher Scientific). The next day, organoids were suspended in a 50% DMEM: 50% Matrigel solution at a density of 20-30 organoids/µL and kept on ice throughout the procedure. We conducted orthotopic transplantations into 3- to 4-week-old NSG mice in a sterile hood. In brief, mice were anesthetized with 2- 2.5% isoflurane and immobilized, the surgical site was cleaned with ethanol. The mammary gland was exposed by a 1-cm mid-sagittal cut followed by a 0.5-cm oblique cut from the initial incision to one hip. The skin was then retracted to expose the number 4 mammary gland. The number 5 gland and the lymph node in the number 4 gland were removed. 10-20 μL of organoid suspension was injected into the number 4 gland using a syringe (702RN[7636–01]; Hamilton; custom 1-in needles, 26 gauge). The skin was then locally infiltrated with 5–10 μL of 0.25% bupivacaine. The same procedure was repeated in the contralateral mammary gland. For each mouse, we transplanted control organoids (*Cre-ER;NMIIA$^{fl/+}$;mTmG*) in one gland and experimental organoids (*Cre-ER;NMIIA$^{fl/fl}$;NMIIB$^{fl/fl}$;mTmG*) in the other. The wounds were closed with 9-mm autoclips. Triple antibiotic ointment was applied to wounding sites. Deletion of NMIIA and NMIIB in mature ductal networks was accomplished six weeks post transplantation by injection of 100 μL of 10mg/mL tamoxifen i.p every other day for 5 days (three total injections) using a 1 mL syringe and a 30G1/2 needle (305106; BD). Glands were harvested 6 weeks after tamoxifen injection.

Differential interference contrast (DIC) microscopy

Time-lapse imaging was performed with an LD Plan-Neofluar 20×/0.4 Korr Ph2 objective lens and a Cell Observer system with an AxioObserver Z1 and an AxioCam MRM camera (Carl Zeiss). In general, 100-200 positions were captured in parallel at 20-min intervals for 5 days. Temperature was set at 37°C and CO_2 at 5%. AxioVision (Carl Zeiss) was used to acquire and analyze the movies, place scale bars, and export time frames as TIFFs. Photoshop CS6 (Adobe) was used to adjust levels and brightness across entire images to maximize image clarity.

Confocal microscopy

Confocal imaging was conducted on a spinning-disk confocal microscope (Solamere Technology Group Inc.) with an XR/MEGA-10 S30 camera (Stanford Photonics, Inc.), as previously described (Ewald, 2013). A Fluar 20×/0.75 objective lens (Carl Zeiss) was used for intermediate magnification images, an LD C-Apochromat 40×/1.1 W Korr objective lens (Carl Zeiss) for high magnification single and time-lapse image acquisition, with water and Immersol^{TM} W 2010 (Zeiss) used as the imaging mediums, respectively. Acquisition was done with a combination of µManager (Edelstein et al., 2010) and Piper (Stanford Photonics, Inc.). For time-lapse imaging to observe cell division, images were captured at 20 minutes intervals for 16-18 hours, and temperature was set at 37°C and CO_2 at 5%. Imaris (Bitplane) was used to analyze images, add scale bars, and export individual TIFFs. Photoshop CS6 (Adobe) was used to adjust levels and gamma for each channel, across the entire image, to maximize image clarity.

Immunofluorescence staining

Organoids and mammary gland tissues were collected, fixed, and stained as previously described (Nguyen-Ngoc et al., 2015). Briefly, organoids embedded in 3D Matrigel and whole mammary glands were fixed in 4% paraformaldehyde for 15 minutes and 3 hours, respectively. The samples were then rinsed three time with PBS for 10 min, embedded in Optimal Cutting Temperature compound (OCT), and stored at -80°C. OCT blocks were sectioned at 100 µm thickness for cultured organoid samples and 50 µm thickness for gland tissue. Sections were placed on Superfrost Plus Gold microscope slides (15-188-48; Fisherbrand) and stored at -80°C. For antibody staining, slides were thawed at ambient temperature, rinsed twice with PBS to remove OCT and permeabilized with 0.5% Triton X-100 for 1 hour. Samples were then blocked with 10% FBS/1% BSA in PBS for 2-3 hours and incubated with primary antibody solution overnight at 4°C in 1% FBS/1%BSA in PBS. Slides were then rinsed twice in PBS with 10% FBS/1% BSA and then incubated with secondary antibodies diluted in PBS with 1% FBS/1% BSA overnight at 4°C. Slides were rinsed twice in PBS with 1% FBS/1% BSA for 10 minutes and once in PBS for 10 minutes, mounted with Fluoromount (F4680; Sigma-Aldrich), and sealed with coverslips. Nuclei were stained with DAPI (1:1000, D3571, Invitrogen). Immunofluorescent staining for each antibody was done for at least three independent biological replicates. Mouse anti-Phospho-Histone H3 (1:300, 9706L, Cell Signaling Technology) was used as primary antibody and Alexa Fluor-647 goat anti-mouse (1:200, Invitrogen) as secondary antibody.

Protein extraction

Lysis buffer was prepared by diluting 10x RIPA buffer (20-188; EMD Millipore) with ultrapure water and incubation on ice for 2 hours. Immediately before addition to cell pellets, lysis buffer was supplemented with 0.1% SDS, 5% glycerol, 3 mM EDTA, 1 mM NaF, 1 mM PMSF, 1.5 mM $NaVO_4$, Aprotinin (A6279; Sigma-Aldrich), and a mini protease inhibitor tablet (11836153001; Roche). Organoids embedded in 3D Matrigel were collected for protein extraction as follows: the medium was aspirated, the gels were rinsed once with 1 mL cold PBS, and then dissolved in 1 mL cold PBS/EDTA buffer (5 mM, 1 mM $NaVO_4$, 1.5 mM NaF, and 1 mM PMSF in PBS). The suspensions were then transferred to centrifuge tubes, mixed well by pipetting, incubated on a shaker for 1 hour at 4°C, and centrifuged at 1500 rpm for 5 minutes at 4°C. Supernatants were removed and pellets were suspended with 50-100 μL of RIPA lysis buffer. The suspension was left on ice for 40-60 minutes and vortexed every 10 minutes. Tubes were centrifuged for 10 minutes at 13,000 rpm at 4°C. Supernatants were transferred to another tubes and stored at -80°C.

Western blotting

Cell lysates were thawed or directly used after preparation. Samples were mixed with Laemmli sample buffer (161-0747; Bio-Rad Laboratories), β-mercaptoethanol and heated at 70°C for 10 minutes. Samples were loaded for equal amount of protein based on bicinchoninic acid (BCA) analysis (Thermo Fisher Scientific) in in 4–15% Mini-PROTEAN TGX precast gels (456-1084; Bio-Rad Laboratories). SDS-PAGE was run at 115V for 1 hour. Gels were transferred onto Immobilon-FL membranes (IPFL07810; Millipore) at 100 V for 1 hour at 4°C. Membranes were blocked in 10 mL Odyssey Blocking Buffer for 1 hour at room temperature on shaker before incubated with primary antibody in 50:50 Odyssey Blocking Buffer/TBST at 4°C overnight. Primary antibodies used were rabbit anti-NMIIA (1:1000; 909801; BioLegend), rabbit anti-NMIIB (1:1000; 909901; BioLegend), rabbit anti-NMIIC (1:1000; 919201; BioLegend) and mouse anti-□ Tubulin (1:1000; T5201; Sigma). Membranes were washed three times with TBST for 5 min, before incubated with secondary antibodies (IR-conjugated Licor) in 50:50 Odyssey blocking buffer/TBST for 1 hour at room temperature on shaker. Secondary antibodies used were goat anti-Rabbit 800CW (1:10,000, 827-08365; Licor) and goat anti-Mouse 680RD (1:10,000; 926-68170; Licor). Membranes were then washed twice with TBST for 5 minutes and once with TBS for 5 minutes, before being imaged wet on the Licor Odyssey CLx. Bands were quantified using ImageJ.

Quantification and statistical analysis

Image analyses were performed using imageJ and Imaris software (Bitplane Scientific, Zurich, Switzerland). All statistical analyses were conducted using STATA or Graphpad Prism. Data was evaluated for normality using D'Agostino-Pearson omnibus test. P value was determined by one-way ANOVA or Mann-Whitney test if the data did not presented a normal distribution. $P < 0.05$ was considered significant. Column plots report s.e.m. All data represent at least three biological replicates.

Acknowledgments

We thank members of the Ewald laboratory for helpful discussions. We thank Seyvonne Ip for help with image acquisition and Alex Choi for help with image analysis. DG is funded by a postdoctoral fellowship grant from the Suzan G. Komen Foundation for the Cure (PDF15332336). AJE received support for this project from the Commonwealth Foundation, the Breast Cancer Research Foundation / Pink Agenda (BCRF-16-048), a grant from the NIH/NCI (U54 CA2101732), the Isaac and Lucille Hay Fellowship, and the Jodi's Climb for Hope Foundation.

Author contributions

Conceptualization: K.N., V.L.S., A.J.E.; Methodology: K.N., V.L.S., D.G., A.N.F., A.J.E.; Formal analysis: K.N., V.L.S., A.J.E.; Investigation: K.N., V.L.S., D.G., A.N.F.; Writing: K.N., V.L.S., A.J.E; Visualization: K.N., V.L.S.; Supervision: A.J.E.; Funding acquisition: A.J.E.

References

Badea, T.C., Y. Wang, and J. Nathans. 2003. A noninvasive genetic/pharmacologic strategy for visualizing cell morphology and clonal relationships in the mouse. *The Journal of neuroscience : the official journal of the Society for Neuroscience*. 23:2314-2322.

Beach, J.R., G.S. Hussey, T.E. Miller, A. Chaudhury, P. Patel, J. Monslow, Q. Zheng, R.A. Keri, O. Reizes, A.R. Bresnick, P.H. Howe, and T.T. Egelhoff. 2011. Myosin II isoform switching mediates invasiveness after TGF-beta-induced epithelial-mesenchymal transition. *Proceedings of the National Academy of Sciences of the United States of America*. 108:17991-17996.

Choi, C.K., M. Vicente-Manzanares, J. Zareno, L.A. Whitmore, A. Mogilner, and A.R. Horwitz. 2008. Actin and alpha-actinin orchestrate the assembly and maturation of nascent adhesions in a myosin II motor-independent manner. *Nature cell biology*. 10:1039-1050.

Conti, M.A., S. Even-Ram, C. Liu, K.M. Yamada, and R.S. Adelstein. 2004. Defects in cell adhesion and the visceral endoderm following ablation of nonmuscle myosin heavy chain II-A in mice. *The Journal of biological chemistry*. 279:41263-41266.

Daley, W.P., K.M. Gulfo, S.J. Sequeira, and M. Larsen. 2009. Identification of a mechanochemical checkpoint and negative feedback loop regulating branching morphogenesis. *Dev Biol*. 336:169-182.

Derksen, P.W., X. Liu, F. Saridin, H. van der Gulden, J. Zevenhoven, B. Evers, J.R. van Beijnum, A.W. Griffioen, J. Vink, P. Krimpenfort, J.L. Peterse, R.D. Cardiff, A. Berns, and J. Jonkers. 2006. Somatic inactivation of E-cadherin and p53 in mice leads to metastatic lobular mammary carcinoma through induction of anoikis resistance and angiogenesis. *Cancer Cell*. 10:437-449.

DuFort, C.C., M.J. Paszek, and V.M. Weaver. 2011. Balancing forces: architectural control of mechanotransduction. *Nature reviews. Molecular cell biology*. 12:308-319.

Edelstein, A., N. Amodaj, K. Hoover, R. Vale, and N. Stuurman. 2010. Computer control of microscopes using microManager. *Current protocols in molecular biology*. Chapter 14:Unit14.20.

Ewald, A.J. 2013. Practical considerations for long-term time-lapse imaging of epithelial morphogenesis in three-dimensional organotypic cultures. *Cold Spring Harbor protocols*. 2013:100-117.

Ewald, A.J., A. Brenot, M. Duong, B.S. Chan, and Z. Werb. 2008. Collective epithelial migration and cell rearrangements drive mammary branching morphogenesis. *Dev Cell*. 14:570-581.

Hanahan, D., and R.A. Weinberg. 2011. Hallmarks of cancer: the next generation. *Cell*. 144:646-674.

Huebner, R.J., N.M. Neumann, and A.J. Ewald. 2016. Mammary epithelial tubes elongate through MAPK-dependent coordination of cell migration. *Development*. 143:983-993.

Jacobelli, J., R.S. Friedman, M.A. Conti, A.M. Lennon-Dumenil, M. Piel, C.M. Sorensen, R.S. Adelstein, and M.F. Krummel. 2010. Confinement-optimized three-dimensional T cell amoeboid motility is modulated via myosin IIA-regulated adhesions. *Nature immunology*. 11:953-961.

Jeanes, A., C.J. Gottardi, and A.S. Yap. 2008. Cadherins and cancer: how does cadherin dysfunction promote tumor progression? *Oncogene*. 27:6920-6929.

Lecuit, T., and A.S. Yap. 2015. E-cadherin junctions as active mechanical integrators in tissue dynamics. *Nature cell biology*. 17:533-539.

Ma, X., and R.S. Adelstein. 2014. The role of vertebrate nonmuscle Myosin II in development and human disease. *Bioarchitecture*. 4:88-102.

Ma, X., J. Bao, and R.S. Adelstein. 2007. Loss of cell adhesion causes hydrocephalus in nonmuscle myosin II-B-ablated and mutated mice. *Molecular biology of the cell*. 18:2305-2312.

Ma, X., S. Kawamoto, Y. Hara, and R.S. Adelstein. 2004. A point mutation in the motor domain of nonmuscle myosin II-B impairs migration of distinct groups of neurons. *Molecular biology of the cell*. 15:2568-2579.

Ma, X., K. Takeda, A. Singh, Z.X. Yu, P. Zerfas, A. Blount, C. Liu, J.A. Towbin, M.D. Schneider, R.S. Adelstein, and Q. Wei. 2009. Conditional ablation of nonmuscle myosin II-B delineates heart defects in adult mice. *Circulation research*. 105:1102-1109.

Meyer, T.N., C. Schwesinger, R.V. Sampogna, D.A. Vaughn, R.O. Stuart, D.L. Steer, K.T. Bush, and S.K. Nigam. 2006. Rho kinase acts at separate steps in ureteric bud and metanephric mesenchyme morphogenesis during kidney development. *Differentiation; research in biological diversity*. 74:638-647.

Michael, L., D.E. Sweeney, and J.A. Davies. 2005. A role for microfilament-based contraction in branching morphogenesis of the ureteric bud. *Kidney Int*. 68:2010-2018.

Moore, K.A., T. Polte, S. Huang, B. Shi, E. Alsberg, M.E. Sunday, and D.E. Ingber. 2005. Control of basement membrane remodeling and epithelial branching morphogenesis in embryonic lung by Rho and cytoskeletal tension. *Dev Dyn*. 232:268-281.

Muzumdar, M.D., B. Tasic, K. Miyamichi, L. Li, and L. Luo. 2007. A global double-fluorescent Cre reporter mouse. *Genesis (New York, N.Y. : 2000)*. 45:593-605.

Nguyen-Ngoc, K.V., E.R. Shamir, R.J. Huebner, J.N. Beck, K.J. Cheung, and A.J. Ewald. 2015. 3D culture assays of murine mammary branching morphogenesis and epithelial invasion. *Methods in molecular biology (Clifton, N.J.)*. 1189:135-162.

Sahai, E., and C.J. Marshall. 2002. RHO-GTPases and cancer. *Nature reviews. Cancer*. 2:133-142.

Schramek, D., A. Sendoel, J.P. Segal, S. Beronja, E. Heller, D. Oristian, B. Reva, and E. Fuchs. 2014. Direct in vivo RNAi screen unveils myosin IIa as a tumor suppressor of squamous cell carcinomas. *Science (New York, N.Y.)*. 343:309-313.

Shamir, E.R., E. Pappalardo, D.M. Jorgens, K. Coutinho, W.T. Tsai, K. Aziz, M. Auer, P.T. Tran, J.S. Bader, and A.J. Ewald. 2014. Twist1-induced dissemination preserves epithelial identity and requires E-cadherin. *The Journal of cell biology*. 204:839-856.

Smutny, M., H.L. Cox, J.M. Leerberg, E.M. Kovacs, M.A. Conti, C. Ferguson, N.A. Hamilton, R.G. Parton, R.S. Adelstein, and A.S. Yap. 2010. Myosin II isoforms identify distinct functional modules that support integrity of the epithelial zonula adherens. *Nature cell biology*. 12:696-702.

Sternlicht, M.D., H. Kouros-Mehr, P. Lu, and Z. Werb. 2006. Hormonal and local control of mammary branching morphogenesis. *Differentiation; research in biological diversity*. 74:365-381.

Sumigray, K.D., H.P. Foote, and T. Lechler. 2012. Noncentrosomal microtubules and type II myosins potentiate epidermal cell adhesion and barrier formation. *The Journal of cell biology*. 199:513-525.

Thomas, D.G., A. Yenepalli, C.M. Denais, A. Rape, J.R. Beach, Y.L. Wang, W.P. Schiemann, H. Baskaran, J. Lammerding, and T.T. Egelhoff. 2015. Non-muscle myosin IIB is critical for nuclear translocation during 3D invasion. *J Cell Biol*. 210:583-594.

Vargo-Gogola, T., B.M. Heckman, E.J. Gunther, L.A. Chodosh, and J.M. Rosen. 2006. P190-B Rho GTPase-activating protein overexpression disrupts ductal morphogenesis and induces hyperplastic lesions in the developing mammary gland. *Molecular endocrinology (Baltimore, Md.)*. 20:1391-1405.

Vega, F.M., and A.J. Ridley. 2008. Rho GTPases in cancer cell biology. *FEBS Letters*. 582:2093-2101.

Vicente-Manzanares, M., X. Ma, R.S. Adelstein, and A.R. Horwitz. 2009. Non-muscle myosin II takes centre stage in cell adhesion and migration. *Nature reviews. Molecular cell biology*. 10:778-790.

Yam, P.T., C.A. Wilson, L. Ji, B. Hebert, E.L. Barnhart, N.A. Dye, P.W. Wiseman, G. Danuser, and J.A. Theriot. 2007. Actin-myosin network reorganization breaks symmetry at the cell rear to spontaneously initiate polarized cell motility. *The Journal of cell biology*. 178:1207-1221.

Figure 2-1. Concurrent loss of both NMIIA and NMIIB in a subset of cells in the mammary epithelium is sufficient to induce tissue growth.

(A) Schematic representation of 3D organotypic culture of *Cre-ER;NMIIA$^{fl/fl}$;NMIIB$^{fl/fl}$* mammary epithelial organoids in basal medium (No GF). Organoids from the same mouse are divided into three groups for control (Untreated), adenoviral Cre recombinase (Ad-Cre) or tamoxifen (Tam) treatments. Ad-Cre was used to accomplish mosaic recombination and tamoxifen induced the Cre-ER to recombine ubiquitously. (B) Representative western blot and (C) protein quantification showing a reduction of NMIIA and NMIIB proteins levels in organoids after Ad-Cre and Tam treatments, respectively. (n= 3 mice. Whole organoid lysate samples were loaded for equal protein based on BCA analysis). (D) Mammary organoid growth was evaluated by fold increase in projected surface area of organoids at day 5 divided by day 0 in culture. Data are presented as mean+/-s.d. ns, non-significant. n, number of organoids summed across three biologically independent experiments ($P<0.0001$, one-way ANOVA). (E-K) Still images from time-lapse movies of organoids carrying different combinations of NMIIA and NMIIB floxed alleles, treated with Ade-Cre in basal medium without growth factor. Scale bars: (E-K) 50μm.

Figure 2-1.

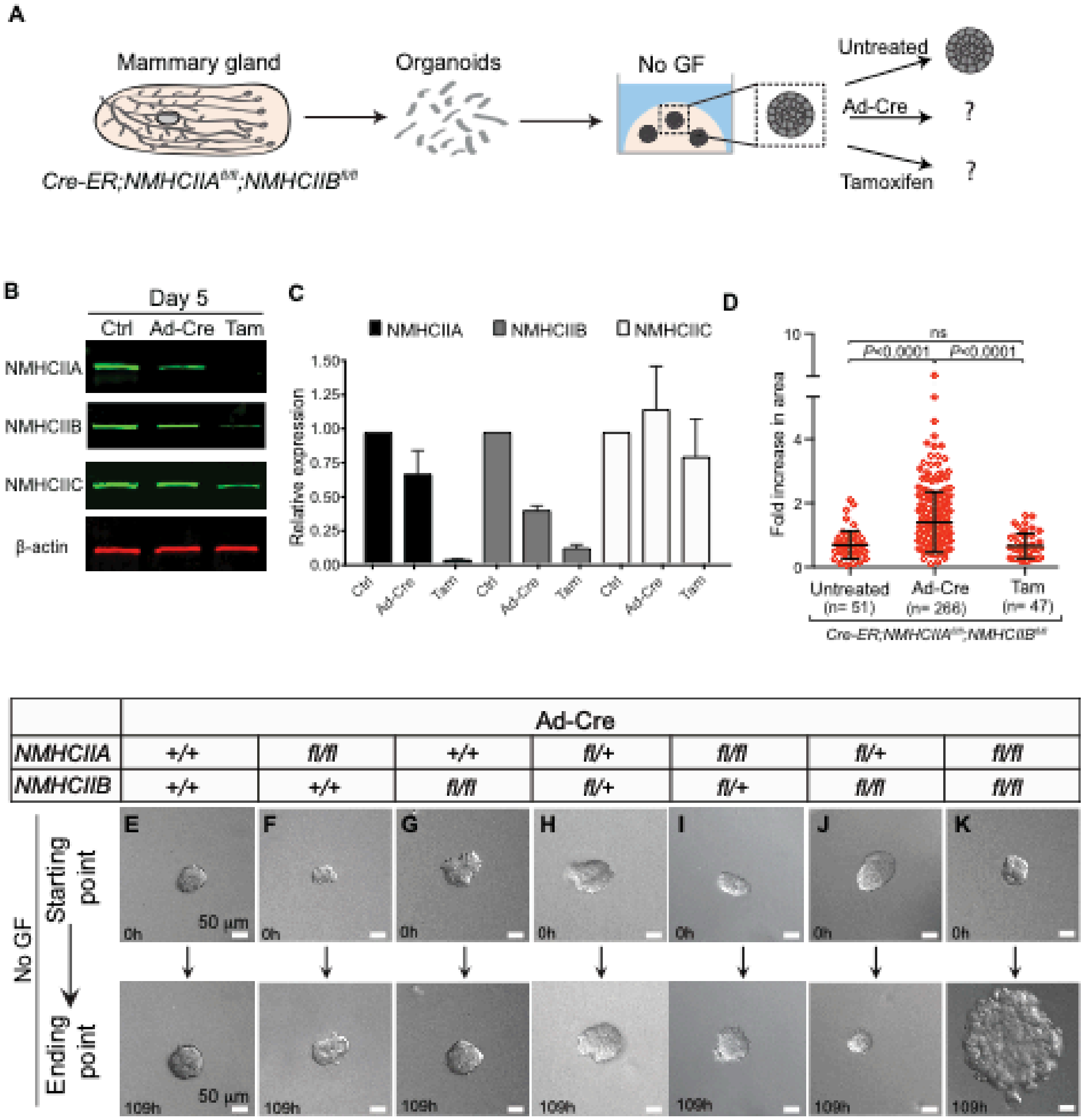
A
Mammary gland
Organoids
No GF
Untreated
Ad-Cre
?
Tamoxifen
?
Cre-ER;NMHCIIA fl/fl;NMHCIIB fl/fl
B
Day 5
Ctrl
Ad-Cre
Tam
NMHCIIA
NMHCIIB
NMHCIIC
β-actin
C
NMHCIIA
NMHCIIB
NMHCIIC
Relative expression
1.50
1.25
1.00
0.75
0.50
0.25
0.00
Ctrl
Ad-Cre
Tam
Ctrl
Ad-Cre
Tam
Ctrl
Ad-Cre
Tam
D
Fold increase in area
10
4
2
0
ns
P<0.0001
P<0.0001
Untreated (n= 51)
Ad-Cre (n= 266)
Tam (n= 47)
Cre-ER;NMHCIIA fl/fl;NMHCIIB fl/fl
Ad-Cre
NMHCIIA
+/+
fl/fl
+/+
fl/+
fl/fl
fl/+
fl/fl
NMHCIIB
+/+
+/+
fl/fl
fl/+
fl/+
fl/fl
fl/fl
No GF
Starting point
Ending point
E
F
G
H
I
J
K
0h
50 µm
109h
50 µm

Figure 2-2. Mosaic loss of NMIIA and IIB induces proliferation in mammary organoids cultured in basal medium or with FGF2 supplementation.

(A) The growth rate of organoids carrying different numbers of floxed alleles of NMIIA and NMIIB treated with Ad-Cre in basal medium (No GF) was determined by measuring organoid projected surface area normalized to initial size. (B-C) Confocal images of mammary organoids in basal medium stained to label proliferation (pH3, green) and nuclei (blue). (D) Fold increase in pH3+ cells of organoids in basal medium was calculated by dividing the number of pH3+ cells per number of cells per organoid compared to control. (E) The growth rate of organoids carrying different numbers of floxed alleles of NMIIA and NMIIB treated with Ad-Cre in FGF2 supplemented medium was determined by measuring organoid projected area normalized to the initial size. (F-G) Confocal images of organoids in FGF2 supplemented medium stained to label proliferation (pH3, green) and nuclei (blue). (H) Fold increase in pH3+ cells of organoids in FGF2 supplemented medium was calculated by dividing the number of pH3+ cells by the organoid projected surface area compared to control. n, number of organoids summed across three biologically independent experiments. Stars highlight the significant difference in growth rate across samples within the same time point. White dash lines mark the shape of organoids. Error bars indicate s.e.m. [$P<0.0001$, one-way ANOVA (A), (E)]. [$P<0.0001$, Mann-Whitney test (D), (H)]. Scale bars: 20μm.

Figure 2-2.

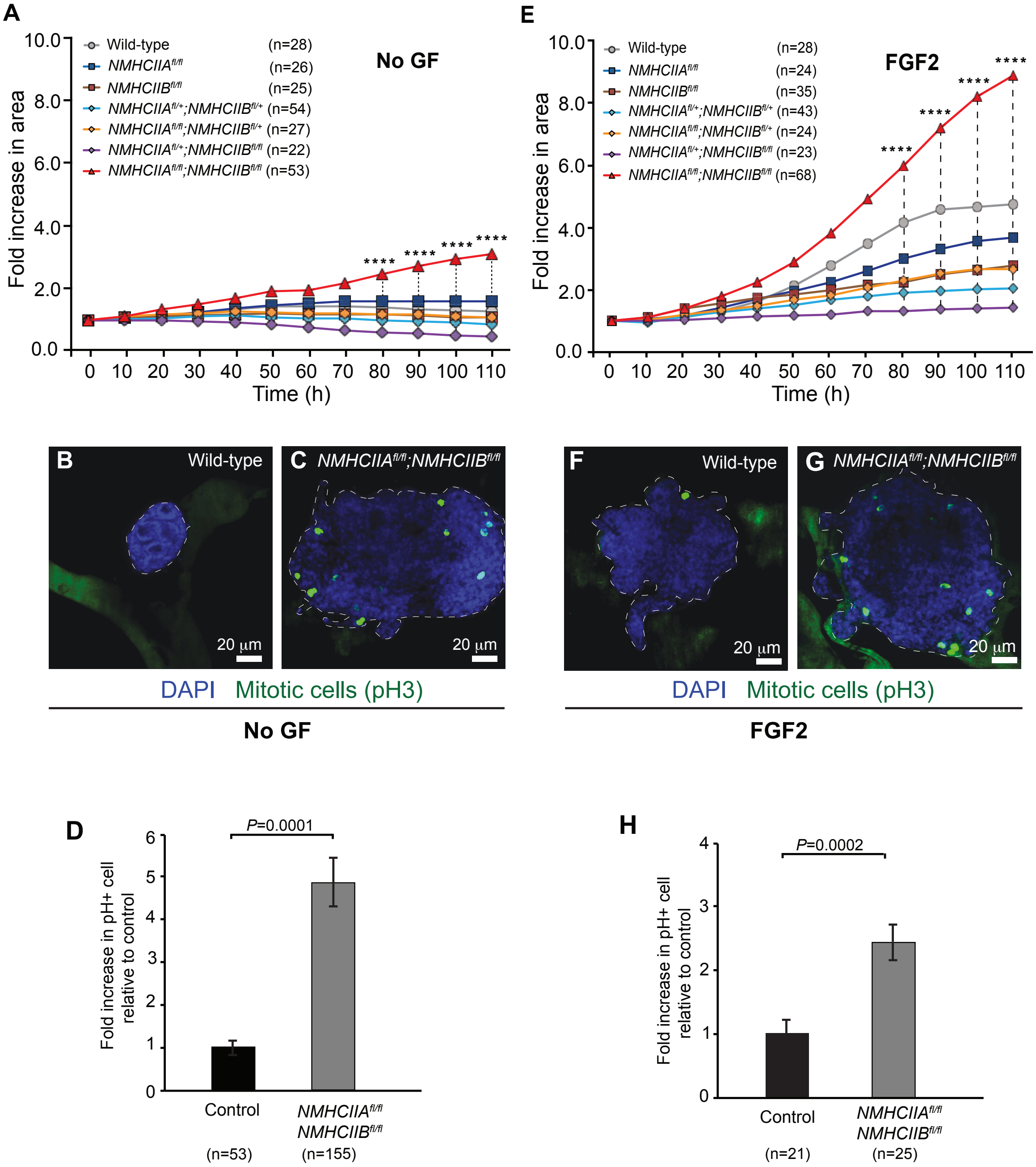
A
No GF
Fold increase in area
Time (h)
10.0
8.0
6.0
4.0
2.0
0.0
0 10 20 30 40 50 60 70 80 90 100 110
Wild-type (n=28)
NMHCIIA$^{fl/fl}$ (n=26)
NMHCIIB$^{fl/fl}$ (n=25)
NMHCIIA$^{fl/+}$;NMHCIIB$^{fl/+}$ (n=54)
NMHCIIA$^{fl/fl}$;NMHCIIB$^{fl/+}$ (n=27)
NMHCIIA$^{fl/+}$;NMHCIIB$^{fl/fl}$ (n=22)
NMHCIIA$^{fl/fl}$;NMHCIIB$^{fl/fl}$ (n=53)
****
E
FGF2
Fold increase in area
Time (h)
10.0
8.0
6.0
4.0
2.0
0.0
0 10 20 30 40 50 60 70 80 90 100 110
Wild-type (n=28)
NMHCIIA$^{fl/fl}$ (n=24)
NMHCIIB$^{fl/fl}$ (n=35)
NMHCIIA$^{fl/+}$;NMHCIIB$^{fl/+}$ (n=43)
NMHCIIA$^{fl/fl}$;NMHCIIB$^{fl/+}$ (n=24)
NMHCIIA$^{fl/+}$;NMHCIIB$^{fl/fl}$ (n=23)
NMHCIIA$^{fl/fl}$;NMHCIIB$^{fl/fl}$ (n=68)
****
B Wild-type
C NMHCIIA$^{fl/fl}$;NMHCIIB$^{fl/fl}$
20 μm
DAPI Mitotic cells (pH3)
No GF
F Wild-type
G NMHCIIA$^{fl/fl}$;NMHCIIB$^{fl/fl}$
20 μm
DAPI Mitotic cells (pH3)
FGF2
D
Fold increase in pH+ cell relative to control
0 1 2 3 4 5 6
P=0.0001
Control (n=53)
NMHCIIA$^{fl/fl}$ NMHCIIB$^{fl/fl}$ (n=155)
H
Fold increase in pH+ cell relative to control
0 1 2 3 4
P=0.0002
Control (n=21)
NMHCIIA$^{fl/fl}$ NMHCIIB$^{fl/fl}$ (n=25)

Figure 2-3. Heterogeneous loss of NMIIA and NMIIB induces proliferation of both NMIIA,B-null and wildtype cells within the mammary epithelium.

(A) Organoids isolated from *Cre-ER;NMIIA*$^{fl/fl}$*;NMIIB*$^{fl/fl}$*;mTmG* mice were treated with Ad-Cre to generate a mixture of Cre- (red) and Cre+ (green) cells. Mosaic organoids were plated in 3D Matrigel in basal medium (No GF) to test cell autonomy. There were 3 potential outcomes: i) Cre+ dominant, ii) Cre- dominant or iii) a mixture of both Cre+ and Cre- cells. (B and D) Representative 3D Projection and (C and E) 3D surface rendering of mosaic organoid at day 3 and day 5 in culture. (F-G) Plots of initial and final surface-rendered volumes of red and green cell, respectively. (H) Percent change in volume of Cre- and Cre+ cells. Error bars indicate s.e.m. P value determined by the Mann–Whitney test. n, number of organoids summed across three biologically independent experiments. Scale bars: 20μm.

Figure 2-3.

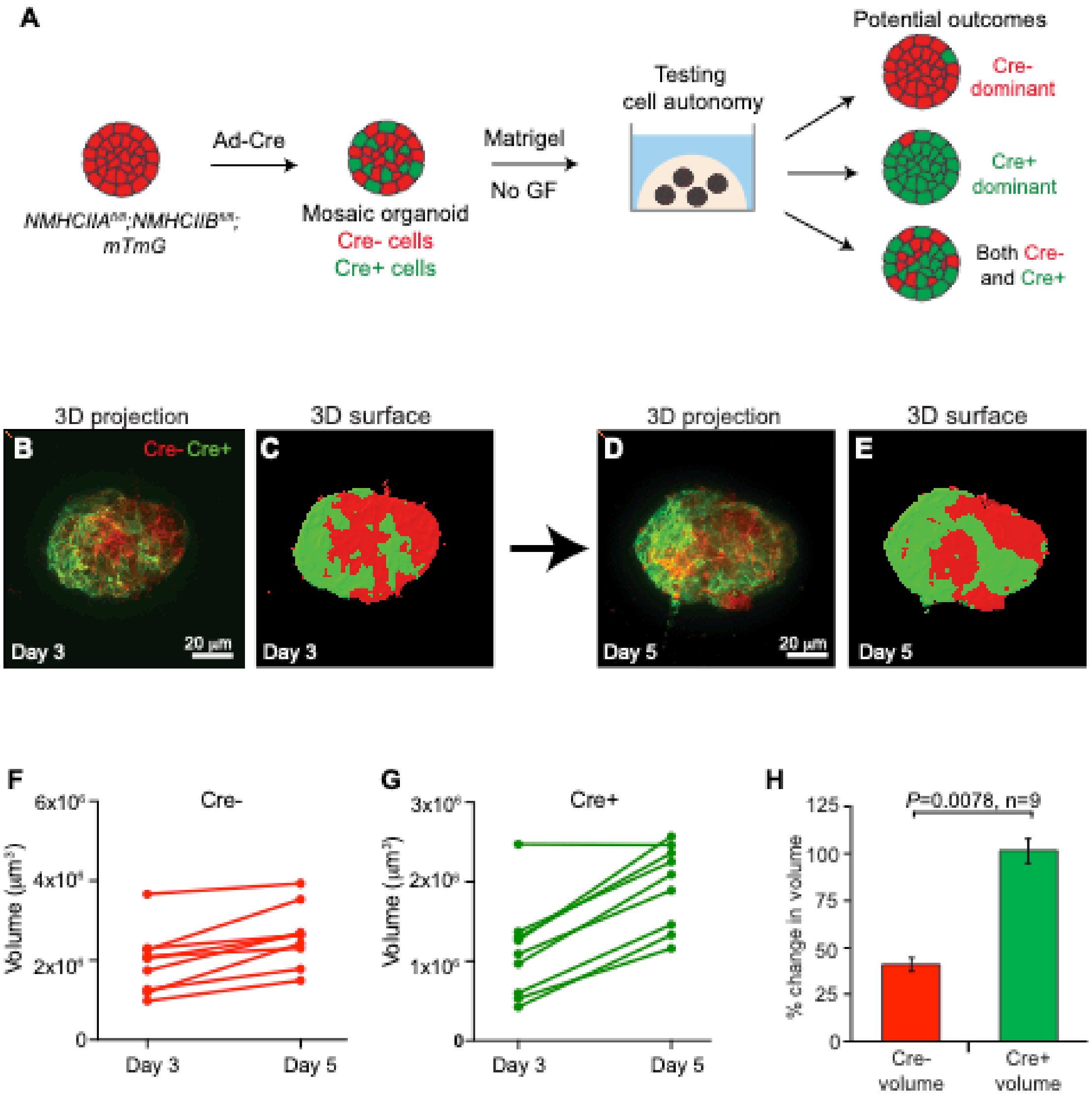
A
NMHCIIA$^{fl/fl}$;NMHCIIB$^{fl/fl}$;
mTmG
Ad-Cre
Mosaic organoid
Cre- cells
Cre+ cells
Matrigel
No GF
Testing
cell autonomy
Potential outcomes
Cre-
dominant
Cre+
dominant
Both Cre-
and Cre+
3D projection
B
Cre- Cre+
Day 3
20 µm
3D surface
C
Day 3
3D projection
D
Day 5
20 µm
3D surface
E
Day 5
F
Cre-
Volume (µm^3)
6x10^6
4x10^6
2x10^6
0
Day 3
Day 5
G
Cre+
Volume (µm^3)
3x10^6
2x10^6
1x10^6
0
Day 3
Day 5
H
P=0.0078, n=9
% change in volume
125
100
75
50
25
0
Cre-
volume
Cre+
volume

Figure 2-4. Coculture of mosaic NMIIA,B-null organoids with wildtype organoids reveal that the hyperproliferation is restricted to the mosaic epithelium.

(A) Control and genetic mosaic organoids from the same mouse were mono-cultured or co-cultured in a 1:1 ratio (control organoid: mosaic organoid) in basal media (No GF) for 5 days. Representative 3D projection images for (B) wild-type (negative control) (C) co-culture (wild-type + mosaic organoids) and (D) mosaic organoids (positive control) at day 5 in culture. (E) Fold increase in mammary organoid growth was calculated by measuring projected surface area compared to wild-type control. Error bars indicate s.e.m.

P<0.0001, ns, non-significant, Mann-Whitney test. n, number of organoids summed across three biologically independent experiments. Scale bars: 20μm.

Figure 2-4.

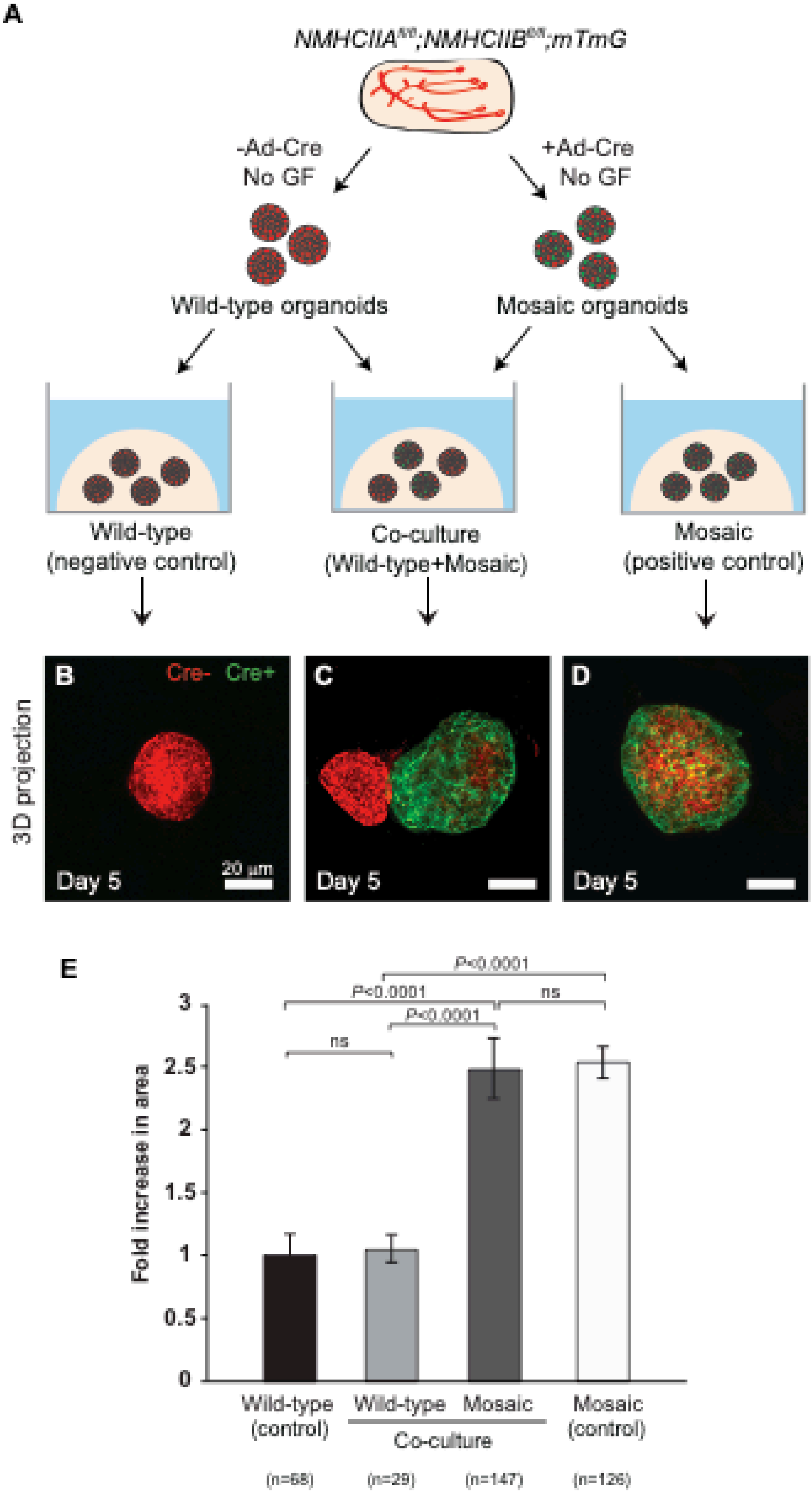
A
$NMHCIIA^{fl/fl};NMHCIIB^{fl/fl};mTmG$
-Ad-Cre
No GF
+Ad-Cre
No GF
Wild-type organoids
Mosaic organoids
Wild-type
(negative control)
Co-culture
(Wild-type+Mosaic)
Mosaic
(positive control)
3D projection
B
Cre-
Cre+
Day 5
20 µm
C
Day 5
D
Day 5
E
Fold increase in area
3
2.5
2
1.5
1
0.5
0
P<0.0001
P<0.0001
ns
P<0.0001
ns
Wild-type
(control)
Wild-type
Mosaic
Co-culture
Mosaic
(control)
(n=68)
(n=29)
(n=147)
(n=126)

Supplemental Figure 2-1. Expression and localization of NMII isoforms in the mammary epithelium.

Mammary epithelial ducts were imaged to show localization of (A') NMHIIA-GFP (located in both luminal and myoepithelial cells), (B') NMHIIB-GFP (located in myoepithelial and in luminal cells at the apical membrane), and (C') stained for NMHIIC (located predominantly in luminal epithelial cells). (A''-C'') F-actin and (A'''-C'''). smooth muscle actin (SMA; Connan et al.) Merged images Scale bars: 20µm.

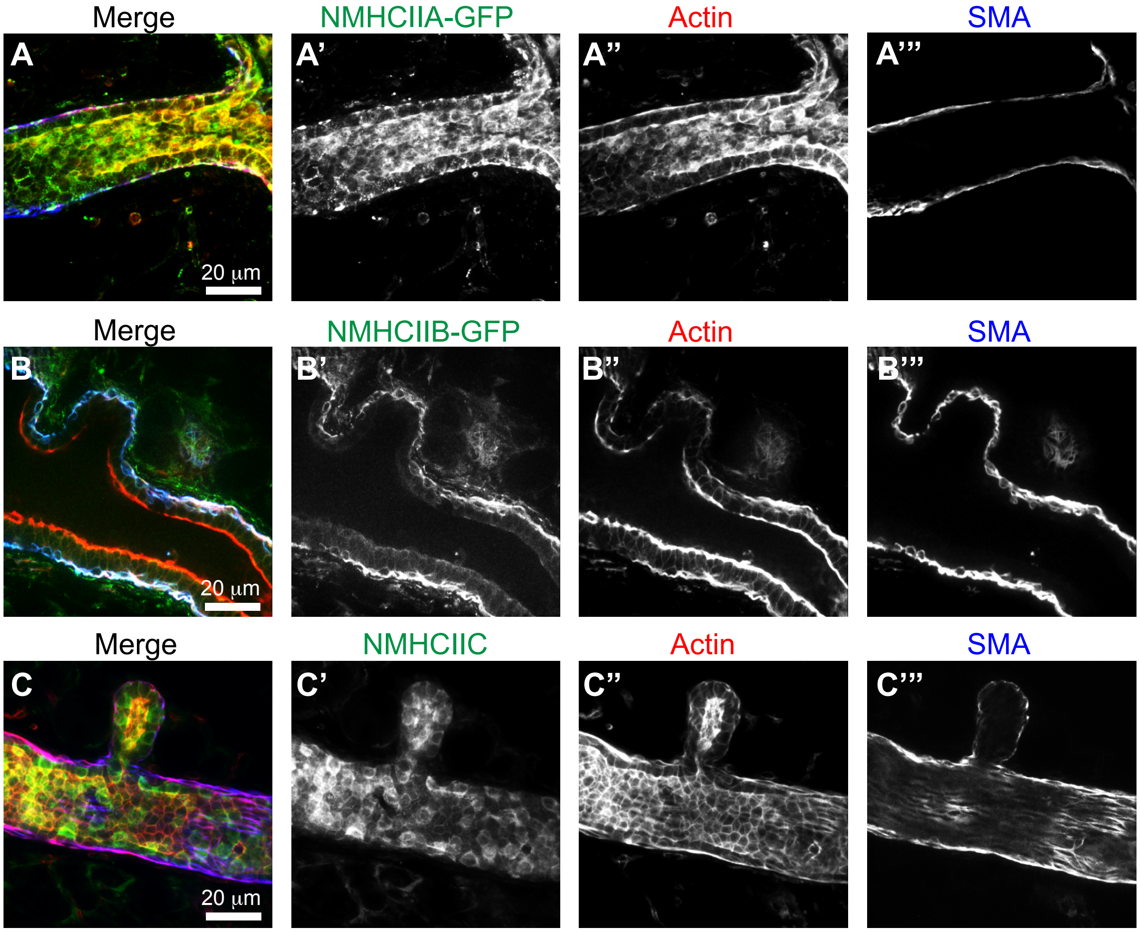

Supplemental Figure 2-2. Mosaic deletion of both alleles of NMIIA and NMIIB induces proliferation in organoids cultured in basal medium or with FGF2 supplementation.

(A-D) Representative still images of mammary organoids from *Cre-ER;NMIIA*$^{fl/fl}$*;NMIIB*$^{fl/fl}$ mice for control (Untreated), adenoviral GFP (Ad-GFP, adenoviral control), adenoviral Cre recombinase (Ad-Cre) and Tamoxifen (Tam) treatments. (E-F) Representative still images of mammary epithelial organoids from wild-type mice not carrying loxP-flanked *NMHCIIA* and *NMHCIIB* alleles for control (Untreated) and Tam treatment. (G) Mammary organoid growth in basal medium was evaluated by fold increase in projected surface area of organoids at day 5 divided day 0 in culture. Images and data correspond to figure 1D. Data are presented as mean+/-s.d., ns, non-significant. n, total number of organoids for 3 mice ($P<0.0001$, one-way ANOVA). The data for *Cre-ER;NMIIA*$^{fl/fl}$*;NMIIB*$^{fl/fl}$ organoids in the Untreated, Ad-Cre, and Tam conditions are duplicated from Figure 1D for ease of comparison. (H-N) Representative still images from time-lapse movies of organoids carrying different genetic variants of *NMHIIA* and *NMHIIB* alleles treated with Ad-Cre in media supplemented with FGF2. Scale bars: 50µm.

Supplemental Figure 2-2.

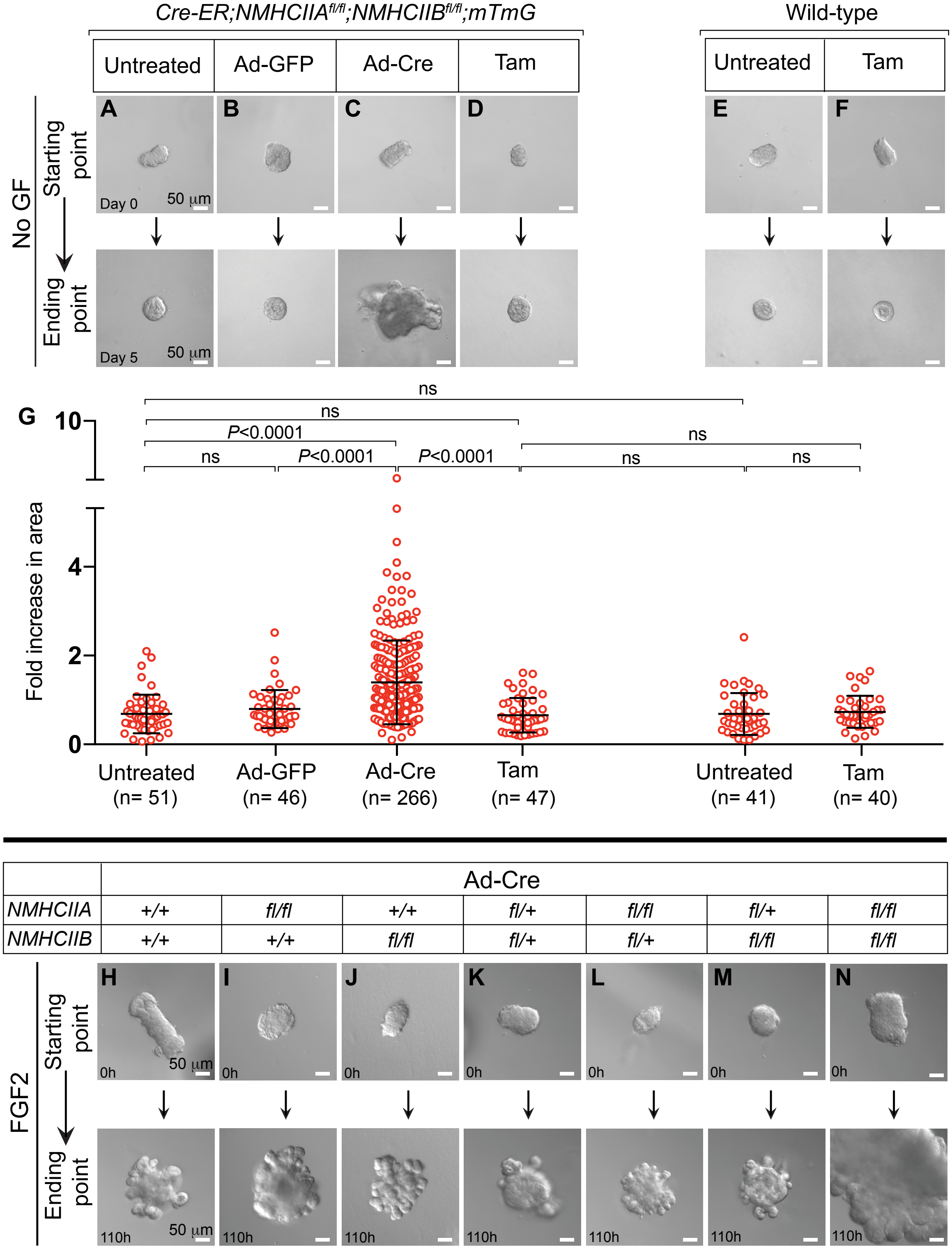

Supplemental Figure 2-3. NMIIA and NMIIB double deletion induces proliferation of both wild-type and NMIIA,B null cells in mosaic organoids.

(A) Frames from a representative confocal time-lapse movie of a mosaic NMIIA,B-null organoid in basal medium conditions. (B) Insets of the red channel to depict cell division in wild-type cells. (C) Insets of the green channel to depict cell division in NMIIA,B-null cells. White dash lines marked changes in cell shape throughout cell division. Scale bars: 20μm.

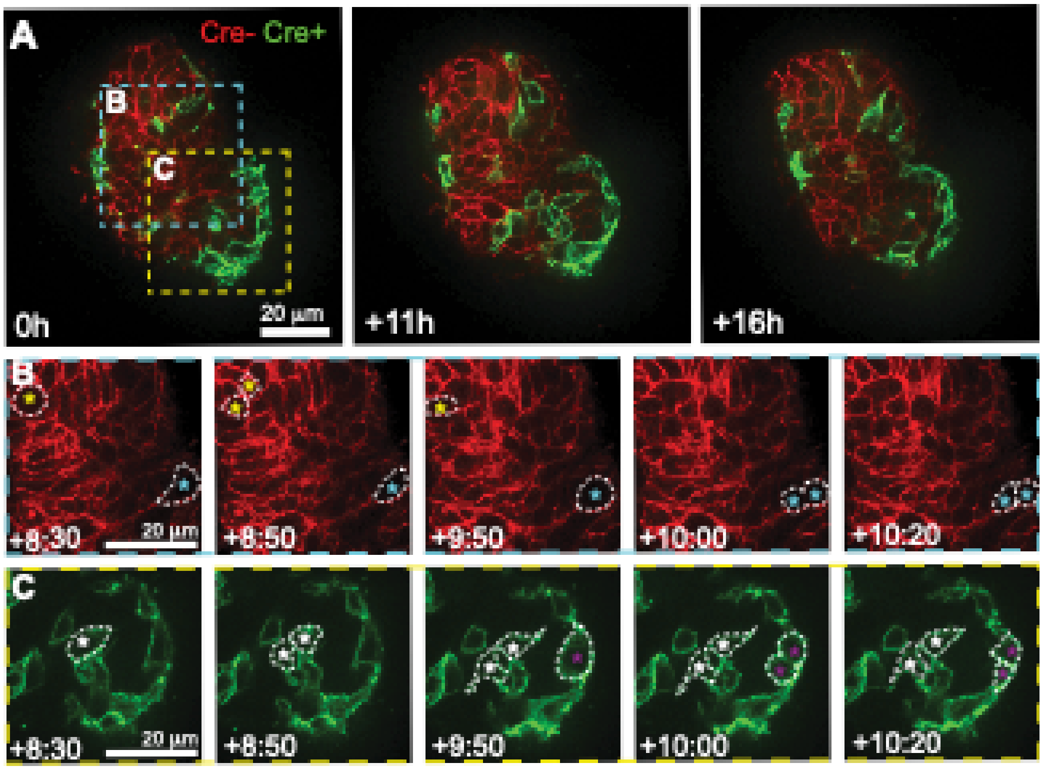

Supplemental Figure 2-4. NMIIA,B deletion increases spontaneous proliferation *in vivo*.

(A) Schematic description of orthotopic transplantation and inducible gene deletion. (B-C) Representative images of different epithelial structures found in the control glands. (B’-C’) Representative images of epithelial structures with pH3+ cells found in NMIIA,B deleted glands. (D) The average number of pH3+ cells per epithelial duct imaged at 40x magnification. (E-F) Different section views of the same epithelial duct. (E’-F’) Insets of proliferating (pH3) NMIIA,B-null (Cre+) and wild-type (Cre-) cells. (G) Fold increase in proliferating Cre- and Cre+ cells within NMIIA,B-null epithelium. Error bars indicate s.e.m. $P<0.0001$, Mann–Whitney test. n, number of fields summed across three biologically independent experiments. Scale bars: (B-C’ and E-F) 20µm, (E’-F’) 10µm.

Supplemental Figure 2-4.

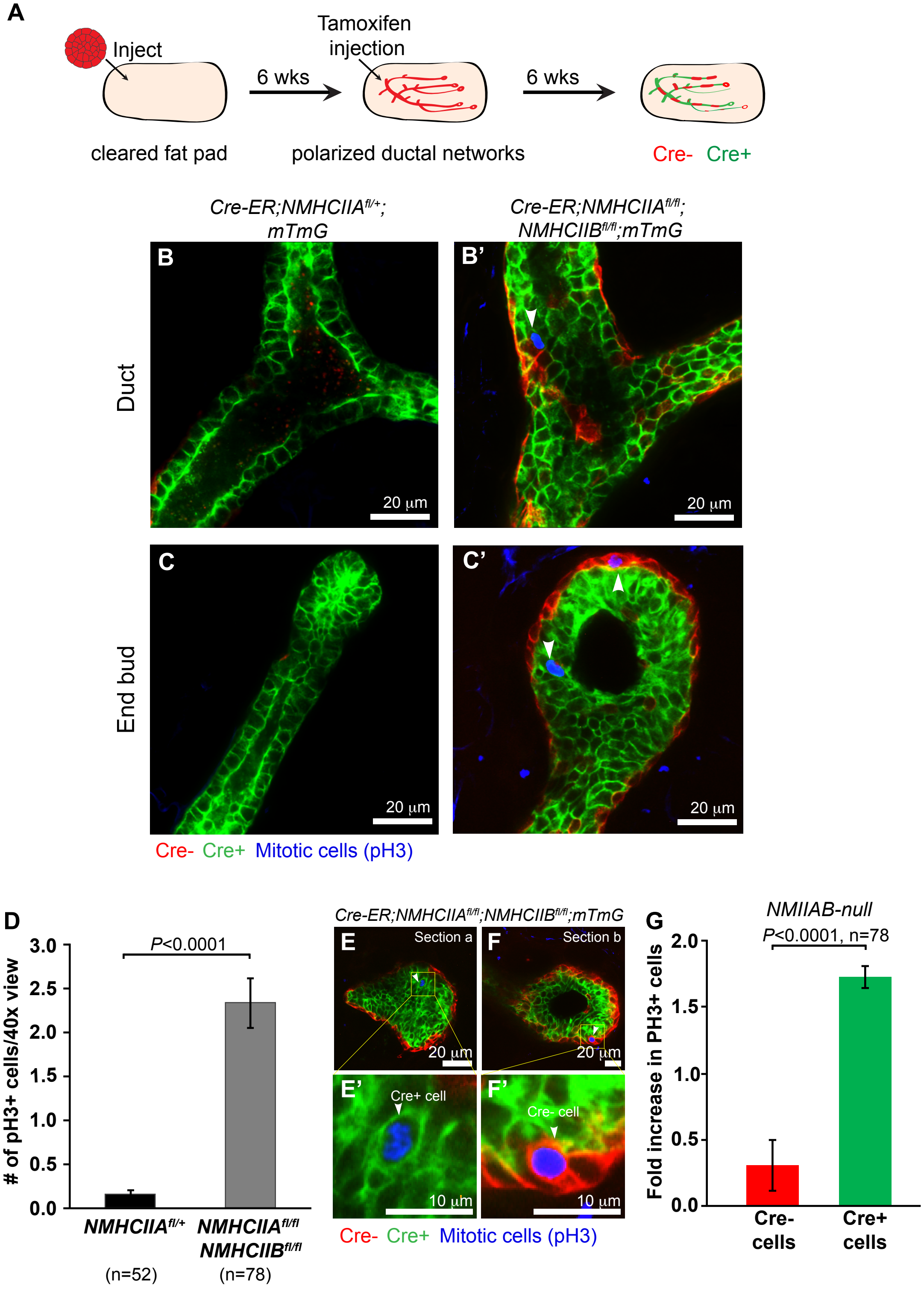

CHAPTER 3

Polyclonal breast cancer metastases arise from collective dissemination of keratin 14 expressing tumor cell clusters

(Modified from Cheung, K.J., V. Padmanaban, V. Silvestri, K. Schipper, J.D. Cohen, A.N. Fairchild, M.A. Gorin, J.E. Verdone, K.J. Pienta, J.S. Bader, and A.J. Ewald. 2016. Polyclonal breast cancer metastases arise from collective dissemination of keratin 14-expressing tumor cell clusters. *Proceedings of the National Academy of Sciences of the United States of America*. 113:E854-863.)

Abstract

Recent genomic studies challenge the conventional model that each metastasis must arise from a single tumor cell and instead reveal that metastases can be composed of multiple genetically distinct clones. These intriguing observations raise the question: How do polyclonal metastases emerge from the primary tumor? In this study, we used multicolor lineage tracing to demonstrate that polyclonal seeding by cell clusters is a frequent mechanism in a common mouse model of breast cancer, accounting for >90% of metastases. We directly observed multicolored tumor cell clusters across major stages of metastasis, including collective invasion, local dissemination, intravascular emboli, circulating tumor cell clusters, and micrometastases. Experimentally aggregating tumor cells into clusters induced a >15-fold increase in colony formation ex vivo and a >100-fold increase in metastasis formation in vivo. Intriguingly, locally disseminated clusters, circulating tumor cell clusters, and lung micrometastases frequently expressed the epithelial cytoskeletal protein, keratin 14 (K14). RNA-seq analysis revealed that K14+ cells were enriched for desmosome and hemidesmosome adhesion complex genes, and were depleted for MHC class II genes. Depletion of K14 expression abrogated distant metastases and disrupted expression of multiple metastasis effectors, including Tenascin C (*Tnc*), Jagged1 (*Jag1*), and Epiregulin (*Ereg*). Taken together, our findings reveal K14 as a key regulator of metastasis and establish the concept that K14+ epithelial tumor cell clusters disseminate collectively to colonize distant organs.

Introduction

During metastasis, cancer cells escape the primary tumor, travel through the circulation, and colonize distant organs. Conventional models of cancer progression propose that each metastasis arises from the clonal outgrowth of a single tumor cell and this conceptual framework is a foundation for models, such as epithelial-mesenchymal transition (EMT) and migratory cancer stem cells (1). Challenging the generality of the single-cell/single-metastasis model are long-standing clinical observations that tumor cell clusters (also termed “tumor clumps”) are also observed across the stages of metastasis. Tumor cell clusters are detected in the bloodstream of cancer patients (2), clusters can efficiently seed metastases (3), and though rare, circulating tumor cell (CTC) clusters have prognostic significance (4, 5). Furthermore, metastases are composed of multiple genetically distinct tumor cell clones, in mouse models of breast, pancreas, and small cell carcinoma (5–7), and in human metastatic prostate cancer patients (8). Taken together, these observations provide accumulating evidence that tumor cell clusters contribute to metastasis. However, they leave unresolved two important questions: how do tumor cell clusters emerge from the primary tumor, and which molecular features identify cell clusters that metastasize?

An important clinical observation is that cancer cells invade the surrounding stroma as cohesive clusters in the majority of epithelial tumors, a process termed “collective invasion” (9, 10). In breast cancer, collective invasion is facilitated by invasive leader cells, a subpopulation of tumor cells that highly express keratin 14 (K14) and other basal epithelial markers (11). K14+ cells are migratory, protrusive, and lead trailing K14− cells, while maintaining cell–cell cohesion and E-cadherin–based cell contacts.

In this study, we sought to understand how these K14+ cells exit collective invasion strands in the primary tumor and travel to distant organs (12). One hypothesis is that collective invasion is an intermediate step toward eventual single-cell dissemination and monoclonal metastasis. However, tumor cell clusters are detected in circulation (5) and primary human breast tumors can disseminate collectively into the surrounding extracellular matrix in ex vivo assays (13–15). These data prompted an alternative hypothesis, that collectively invading K14+ cancer cells could initiate and complete the metastatic process as a cohesive multicellular unit. Here we define the clonal nature of metastases in a spontaneous mouse model of metastasis to the lungs (16, 17), in which the predominant invasive form in the primary tumor is collective invasion strands led by K14+ cells (11). We establish that the majority of metastases arise from polyclonal seeds, and show that disseminated tumor cell clusters are predominantly composed of K14+ cells. We propose a mechanism for polyclonal metastasis via the collective invasion, dissemination, and colonization of clusters of K14+ cancer cells.

Results

Multicolor fluorescent lineage tracing identifies frequent polyclonal metastasis in a mouse model of breast cancer

To define the clonal origin of metastasis in a model of collective invasion, we developed a multicolor lineage-tracing strategy in a commonly used mouse model of breast cancer, MMTV-PyMT, which has provided fundamental insights into diverse aspects of metastatic progression (16, 17). In this model, the MMTV promoter drives mammary epithelial expression of the polyoma virus middle T antigen (PyMT), a potent activator of PI3K signaling, a hallmark of human breast cancer. The mammary tumors formed in this model show gene expression most similar to luminal B, an aggressive subtype of human breast cancer prone to metastasis (18).

We generated a convertible double-fluorescent mammary tumor model, ROSA$^{mT/mG}$;MMTV-PyMT, in which tumor cells express membrane-localized tdTomato (mTomato) and, upon treatment with adenoviral Cre recombinase (adeno-Cre), switch heritably to expression of membrane-localized enhanced GFP. ROSA$^{mT/mG}$;MMTV-PyMT tumor organoids were treated with adeno-Cre to generate a mixture of red and green cells. Mosaic organoids were then injected orthotopically into the cleared mammary fat pad of nonfluorescent host mice. Because the host is nonfluorescent, this experimental system enabled us to unambiguously identify tumor metastases and their clonal origin (Fig. 1A). The principle of this strategy is that if there is an obligate single-cell intermediate during the metastatic process, we would expect to see a transition from a multicolored primary tumor (red and green) to singly red or green metastases.

In the lungs of these mice, we detected single disseminated tumor cells, micrometastases (2–50 cells), and macrometastases (>50 cells). Single disseminated tumor cells were 47-fold more frequent than metastases (range 10- to 150-fold, n = 10 mice). We reasoned that if lung metastases arose exclusively from seeding of single disseminated tumor cells, then each lung metastasis should express only one color. In contrast, multicellular seeding should be able to produce metastases with both colors. Interestingly, we observed lung metastases composed of both red and green tumor cells across a range of sizes, from 2 cells to >1,000 cells per metastasis (Fig. 1B) (n = 375 multicolored metastases). Multicolored metastases demonstrated significant intermixing of red and green tumor cells. Transplanted mice showed wide variation in the percentage of multicolored metastases from a minimum of 0% to a maximum of 61% (n = 158 multicolored out of 257 metastases). Taken together, our data show that multicolored metastases can occur frequently in the MMTV-PyMT model.

To understand our variable frequency of detection of multicolored metastases, we analyzed the degree of mixing of red and green tumor cell clones at each step in our experiments. Whereas red and green tumor cells were well mixed in the recombined tumor organoids used as input (Fig. 1C), the tumors that resulted from transplanting these organoids showed surprisingly wide variation in the mixing of red and green tumor cells. We observed tumors composed almost entirely of a single color to tumors with significant intermixing of red and green zones (Fig. 1D). To analyze this variation further, we quantified the local mixing of red and green cells within each tumor. Local mixing was assessed in 100 × 100-pixel (1.3 mm × 1.3 mm) regions tiled across the tumor by calculating the probability of selecting two colors when pixel values were chosen at random within each region. We observed a strong linear correlation between the extent of local mixing and the percentage of detected multicolored metastases (Fig. 1E). Thus, local proximity between clones of different colors in the primary tumor determines our ability to detect multicolored metastases. Based on our analysis of the relationship between local mixing and the detection of multicolored metastases (Fig. 1E), we estimate that >97% of metastases were formed from multicellular seeds (95% confidence interval 74–100%).

We also determined the frequency of multicolored metastases in two additional transplant models. In MMTV-PyMT tumors expressing the Confetti lineage reporter (Fig. S1A), tumor cells are induced by adeno-Cre to one of five distinct possible colors: cytoplasmic red fluorescent protein (RFP), cytoplasmic yellow fluorescent protein (YFP), nuclear GFP (nGFP), membrane cyan fluorescent protein (mCFP), or an unrecombined no-color (19). We observed zonal patches of a single color in the primary tumor, with a clear preference for the unrecombined no-color (Fig. S1B). Even with this limitation, we observed lung metastases composed of both no-color and RFP+ tumor cells (Fig. S1C). In MMTVPyMT tumors expressing the Rainbow reporter (Fig. S1D), adeno-Cre induces recombination to one of 21 different color values (20). Despite the increased color diversity, we similarly observed zonal patches of a single color in the primary tumor, with preference for a no-color tumor cell (Fig. S1E). In the lungs of these mice, we observed multiple metastases composed of one to four different colors (Fig. S1F). Taken together, data from three distinct lineage analyses reveal polyclonal metastases in this genetically engineered mouse model of breast cancer metastasis.

Polyclonal lung metastases arise from multicellular seeds and not by serial seeding of single tumor cells

The multicolored metastases that we observed could arise via the serial seeding of single tumor cells or via colonization by a multicellular cluster of tumor cells. We sought to distinguish these mechanisms in two different ways. To model stochastic serial seeding events integrated over time, we first isolated organoids from different MMTV-PyMT tumors that constitutively expressed either mTomato or CFP. We then transplanted mTomato+ tumor organoids to the right flank and CFP+ tumor organoids to the left flank of a nonfluorescent host (Fig. S2 A and B). Interestingly, we observed a small degree of colonization of CFP+ primary tumors by mTomato+ cancer cells, accounting for 1–5% of the total tumor area, determined macroscopically in 5 of 11 mice (Fig. S2B, Lower, and Fig. S2 C and C′). These data are consistent with the reported ability of metastases to reseed primary tumors, termed "tumor self-seeding" (21). Importantly, when we examined the clonal composition in the lungs, we only observed single-colored metastases (Fig. S2D). Taken together, these data establish that polyclonal metastases do not efficiently arise from serial seeding.

To extend this finding, we modeled serial seeding by waves of disseminated tumor cells in the bloodstream. In this second experimental approach, we transplanted mTomato+ and CFP+ tumor cells serially via tail-vein injection (Fig. S2E). mTomato+ tumor cells were isolated by FACS and then injected as a singlecell suspension into a nonfluorescent host. Two days later, CFP+ tumor cells were isolated by FACS and injected as a single-cell suspension into the same mice. Three weeks later, lungs were collected and analyzed.

In the lung, we observed exclusively single-colored metastases (Fig. S2E). Therefore, serial delivery of cancer cells to the lungs was not an efficient mechanism for generation of polyclonal metastases. In agreement with a recent study revealing metastases from oligoclonal clusters in breast cancer cell lines (5), our data are most consistent with a model in which polyclonal metastases occur via colonization by multicellular seeds rather than serial arrival and aggregation of single tumor cells.

Direct observation of polyclonal collective invasion, polyclonal disseminated tumor emboli, and polyclonal CTC clusters

Having shown that polyclonal metastases arise from multicellular seeding, we next asked how multicellular seeds emerge from the primary tumor. To answer this question, we identified tumor cell clusters across stages of metastasis, starting from collective invasion at the primary tumor stromal interface. Consistent with our local mixing analysis (Fig. 1 D and E), when we imaged at single-cell resolution, transplanted tumors were composed of zonal patches and collective invasion strands were typically composed of a single color. Despite this technical barrier to detection of polyclonal groups, we observed multicolored collective invasion at interfaces between regions of red and green cancer cells (Fig. 2A). In these regions, we reasoned that there were two outcomes at the tumor–stromal interface corresponding to two distinct models for the collective invasive-disseminative transition (Fig. 2B). One possibility is that tumor cells invade collectively but that dissemination occurs obligately through single cells. In this case, because disseminated clusters should arise only from focal proliferation of single cells, disseminated clusters should be exclusively composed of singly red or green tumor cells. Alternatively, cancer cells could both invade and disseminate collectively as multicellular units. In this case, we would expect to identify multicolored disseminated clusters.

To distinguish these possibilities, we analyzed disseminated tumor cell clusters at three different stages of the metastatic sequence. First, we observed multicolored disseminated tumor cell clusters ≤200-μm away from the tumor–stromal interface, which we confirmed were fully disconnected from the primary tumor by 3D reconstruction (Fig. 2C). Next, we examined the adjacent vasculature at the tumor–stromal interface (Fig. S3 A–C). We observed both multicolored tumor microemboli and tumor macroemboli composed of >100 tumor cells within vessels (Fig. 2D and Fig. S3D). Consistent with their collective organization, we observed membrane-localized E-cadherin in collectively invading cancer cells, locally disseminated clusters, and tumor emboli (Fig. 2E). As a proof of concept, we next isolated CTCs from the systemic circulation of a mouse bearing fluorescently labeled tumors. Although this tumor had quite limited local mixing of blue and red clones, we identified both a multicolored and multiple singly colored CTC clusters (Fig. 2F). We analyzed CTC cluster size in three mice and found that they ranged from 2 to 66 cells per cluster, with a median of 6 cells (Fig. 2G). Taking these data together, our lineage-tracing studies enabled us to observe multicolored tumor cell clusters at five different stages of metastasis: collective invasion, locally disseminated clusters in the adjacent stroma, intravasated tumor emboli, CTC clusters, and distant micro- and macrometastases.

Aggregating tumor cells into clusters promotes colony formation *ex vivo* and lung metastatic colonization *in vivo*

An important question raised by these experiments is: why are multicellular seeds advantageous for metastatic colonization? This question is interesting because tumor cells typically maintain extensive cell-cell contacts in vivo, and the organization of epithelial cells into cohesive clusters promotes tissue growth in a variety of normal and tumor contexts. For example, doublets of Paneth and Lgr5+ stem cells enhance the organoid-forming potential of single Lgr5+ stem cells (19) while the survival of colonic tumor organoids is dependent on retaining E-cadherin contacts (22).

To model the colonization efficiency of multicellular seeding, we developed an experimental system to aggregate single tumor cells into cell clusters. Briefly, we isolated FACs-sorted single mTomato+ MMTV-PyMT tumor cells and incubated them overnight in a nonadherent dish to form cell clusters (Fig. 3A). Overnight incubation increased the median number of cell clusters by >15 fold relative to the input single cells (Fig. S4A and B). The tumor cell clusters that resulted had a median size of 2 cells, and ranged from 2-60 cells in size (Fig. S4B'). Importantly, co-incubation of red and green tumor cells confirmed that clusters were generated by aggregation rather than by clonal expansion of single tumor cells (Fig. S4C). Further, the experimentally determined percentages of multicolored clusters as a function of cluster size matched the predicted percentages, assuming random assortment of red and green tumor cells into clusters (Fig. S4C'). Incubation in a non-adherent dish therefore induces the efficient aggregation of single cancer cells into clusters. We next used this approach to compare the efficiency of colony formation by single cells or aggregated clusters, while holding the total cell number constant in each condition at 10,000 cells per well. Because each cluster is formed from multiple cells, the total number of starting seeds is lower in the aggregated condition when compared with the single cell condition. Despite this disadvantage, when cultured in 3D Matrigel, we observed that clusters were >15 fold more efficient at forming colonies when compared with single tumor cells (Fig. 3A and B). Thus, in an ex vivo setting cluster organization strongly enhances colony formation.

To assess metastatic efficiency in vivo, we next injected into the tail veins of nonfluorescent host mice either a single cell suspension of mTomato+ tumor cells or an equal number of mTomato+ tumor cells that had been aggregated into clusters in vitro. We assessed lung metastatic burden at 3 weeks (Fig. 3C). Single cell suspensions generated 0-1 metastases per mouse (Fig. 3D-E). In contrast, aggregated clusters generated many large macroscopic mTomato+ metastases with >100 fold increase in metastatic efficiency relative to single cells (Fig. 3D-E). Taken together, these data indicate that cluster organization is sufficient to significantly enhance tumor cell survival and promote metastasis formation.

Locally disseminated tumor cell clusters, CTC clusters, and micrometastases are enriched for K14+ cells, relative to macrometastases

Given the frequency of polyclonal metastases and the efficiency of metastasis formation by multicellular seeding, we next sought to determine the molecular characteristics of the multicellular seed. In MMTV-PyMT tumors, K14+ cells account for approximately 2% of the total tumor cell population (11). These K14+ tumor cells lead >88% of collective invasion strands extending into the surrounding stroma (11). Consistent with the pioneer function of K14+ cells during metastasis, we observed K14+ cells in polyclonal collective invasion, disseminated tumor cell clusters, and intravascular emboli (Fig. S5A). We also observed significant differences in K14 expression between single cells and disseminated clusters, with 2% and 59% expressing K14 respectively (Fig. S5B). In addition, we observed that 94% of CTC clusters contained K14+ cells (**N**=15 of 16 CTC clusters, Fig. 2H). The fraction of cells within the cluster that were K14+ decreased as the size of the cluster increased (Fig. 2H). Our data therefore show that K14+ cells are enriched in the dissemination stages of metastasis.

In lung metastases, the proportion of K14+ cells relative to the total cell number varied systematically with the size of the metastasis (Fig. 4A-B). In the primary tumor, micrometastases, and macrometastases, K14+ cells accounted for 0.9%, >50%, and 2.5% of cells respectively (Fig. 4C). Thus, K14+ cells are highly enriched in locally disseminated clusters, CTC clusters, and micrometastases relative to their frequency in the primary tumor, and the proportion of K14+ cells reverts to baseline in macrometastases.

To model these transitions in 3D culture, we next isolated single K14- and K14+ cells by FACS from MMTV-PyMT tumors that genetically encode for a fluorescent biosensor for K14 expression (Figure 4D and S5C) (11, 23). Accordingly, we observed that for individually purified K14- and K14+ populations, colony formation was >16-fold higher in aggregated clusters relative to single tumor cells (Fig. 4E). In contrast, colony formation was not significantly different for K14- single cells versus K14+ single cells, or for K14- aggregated cells versus K14+ aggregated clusters (Fig. 4E). Together, our data reveal that the difference in colony formation between K14- and K14+ cells is small relative to the difference between multicellular clusters and single cells.

One interpretation of these data could be that the interaction of K14- and K14+ tumor cells may synergistically enhance the efficiency of colony formation. Motivating this hypothesis, Wnt-driven murine mammary tumors contain two subclones that show interclonal cooperation during tumor progression (24). To test the synergy hypothesis, we employed our aggregation assay to test the effect of aggregating equal mixtures of K14- and K14+ cells (Fig. 4D). However, mixing K14- and K14+ cells in aggregating clusters did not significantly enhance colony formation relative to either pure K14- or K14+ cell clusters (Fig. 4E).

Alternatively, phenotypic transitions between differentiation states could blunt our ability to detect differences in colony formation (25). We therefore examined K14 expression in aggregated tumor cells at day 0, day 1 post aggregation (Fig. S5D), and at day 8 (Fig. S5E). Interestingly, cell clusters at day 1 already contained mixtures of K14- and K14+ cells regardless of whether isolated K14- cells, K14+ cells, or mixtures of both cell types were used as input (Fig. S5D). Similarly, at day 8, >80% of colonies were composed of mixtures of K14- and K14+ cells in each condition (Fig. S5E). Morphologically, small colonies were primarily composed of K14+ cells and larger colonies were composed of an inner core of K14- cells and an outer layer of K14+ cells

(Fig. 4F). Concordant with our observations of metastases *in vivo*, the proportion of K14+ cells varied with the size of clusters grown in 3D Matrigel. In small clusters 2-5 cells in size, 100% of cells were K14+ and in larger clusters with ≥ 20 cells, all clusters contained multiple K14- cells (Fig. 4G). Thus, isolated K14- and K14+ cells converge toward cell colonies composed of both cell states, with K14+ cells predominant in small colonies in culture and in micrometastases. Conversely, K14- cells are predominant in large colonies and in macrometastases.

The transcriptional program of K14+ tumor cells is enriched for desmosome and hemidesmosome adhesion complex genes, and depleted for genes involved in MHC class II immunosurveillance

Given the enrichment for K14+ cells in disseminated tumor cell clusters and micrometastases, we next asked how the transcriptional profiles of K14+ and K14- cells differed. To answer this question, we compared the transcriptomes of K14+ and K14- cells from primary MMTV-PyMT tumors. To focus our attention on changes in gene expression between cancer cell subpopulations, we first isolated epithelial organoids from the tumor and then used differential centrifugation to deplete immune and fibroblastic stromal cells. We then processed these organoids to single cells and FACS-sorted them based on K14 status. As expected, quantitative RT-PCR revealed that the K14+ cell fraction exhibited >12-fold higher levels of K14 RNA expression (Fig. 5A). Our RNA-seq analysis revealed 239 genes differentially expressed between K14- and K14+ cells at a genome wide significance level of $P < 10^{-6}$ (mean-variance normalized heatmap in Fig. 5B). By DAVID gene ontology (GO) analysis (26), we identified significantly enriched GO categories in each cell subpopulation (Table S1). This analysis revealed significant enrichment for genes involved in extracellular matrix proteins, intermediate filament organization, and epithelial differentiation in K14+ cells. Interestingly, K14+ cells were enriched for transcripts encoding TNC, POSTN, and CTGF, proteins required in the metastatic niche (27–29). In addition, DAVID analysis revealed a number of genes involved in the regulation of the immune system that were significantly depleted in K14+ cells (Table S1). These GO categories included immune response, MHC class II antigen presentation, T-cell activation, and genes involved in chemotaxis. Genes involved in MHC class II presentation were among the most depleted in K14+ cells (Fig. 5C″). Our data reveal that K14+ cells differ across multiple molecular programs that could be advantageous across distinct steps in metastasis, including immune evasion. Furthermore, two key features distinguishing K14+ cells from the bulk tumor cells are their increased expression of both cell–cell and cell–matrix adhesion genes.

We also tested the extent to which the K14+ cell transcriptome correlated with "stemness" in three ways (30, 31). First, we looked at the expression of putative stem cell markers in K14− and K14+ cells. We observed that *CD44* was differentially expressed between these cell populations, but *CD49f, CD24a, CD133*, and *CD29* were not (Fig. S6A). Next, we tested for gene set enrichment in K14− and K14+ cells with published mouse mammary stem cell gene sets (Fig. S6B). Our gene set tests revealed that K14− cells were enriched for fetal mammary stem cell and luminal epithelial gene signatures. In contrast, K14+ cells were enriched for mammary stem cell, adult mammary stem cell, and myoepithelial gene signatures. A third approach we took to test stemness was to assay the ability of isolated single K14− and K14+ cells to form mammospheres, as in Spike et al. (31) (Fig. S6C). Our data show that both K14− and K14+ cells form mammospheres and that the mammosphere-forming efficiency was not significantly different between K14− and K14+ cells (Fig. S6D). Taken together, our findings are consistent with a model in which stemness features are observed in both K14− and K14+ cells, and that both cell types are capable of colony formation.

K14 expression is required for distant metastasis and regulates gene expression of multiple metastasis effectors

Our gene expression study revealed that K14+ cells displayed coordinated upregulation of most desmosome (10/11) and hemidesmosome (10/12) complex genes (Fig. 5C and C') (32). These observations were intriguing to us because (i) K14 is the major intermediate filament in hemidesmosomes, (ii) leader cells require expression of basal epithelial genes including K14 for their collective invasive behavior (11), and (iii) a recent study has implicated desmosomal function in CTC clusters from human cancer patients (5).

To test the hypothesis that K14 expression is required for distant metastasis, we transplanted mTomato+ tumor organoids, either expressing control Luciferase or K14 shRNA, into host mice (Fig. 6A). Primary tumors derived from Luciferase control knockdown organoids did not show statistically significant differences in size compared to primary tumors derived from K14 knockdown tumor organoids (Fig. 6B). In contrast, K14 knockdown tumors had a 7-fold reduction in the mean number of metastases relative to control knockdown tumors (Fig. 6C).

Having shown that K14 expression is required for distant metastasis, we next asked whether knockdown of K14 altered gene transcription. We determined the transcriptomes of luciferase control knockdown and K14 knockdown tumor organoids by RNA-Seq and identified 1584 genes differentially expressed between conditions (mean-variance normalized heatmap in Fig. 6D). To dissect this list further, we next ranked genes by their association with *Krt14* transcript levels (487 genes at an FDR < 0.05). The top four genes most correlated with *Krt14* transcript expression were enriched for multiple major metastasis effector genes that promote metastatic niche remodeling (*Tnc, AdamTs1, Jag1*) and metastasis survival (*AdamTs1, Birc5*) (Fig. 6D') (27, 29, 33, 34). Thus, disruption of K14 expression abrogates the expression of multiple metastasis effectors.

To identify the core molecular program expressed in K14+ cells and regulated by K14 expression, we then integrated this transcriptome data with our RNA-seq enrichment data for K14+ cells. We identified 14 genes with 2 fold or greater significant enrichment in K14+ cells and whose gene expression was significantly associated with *Krt14* transcript levels (Figure 6E). Consistent with our observations in the K14 knockdown dataset, we observed that 9 of these genes were previously reported in metastasis regulation, including in metastatic niche, vascular remodeling, and immunosurveillance, including *Tnc, AdamTs1, Jag1 as well as Card10, Cav1, Ereg, Lgr5, Slpi, and Ptgs2* (29, 35-38). Core genes showed evidence of multiple physical and genetic interactions and occurrence along common pathways (Fig. S7A). Interestingly, the gene most highly enriched in K14+ cells and positively regulated by *Krt14* transcript levels was *Dsg3*, which encodes for the major desmoglein in desmosomes. Thus, K14 expression also regulates the expression of a major desmosome component. Taken together our data establish that K14 expression is required for distant metastasis and that K14 is a regulator of multiple genes that function at distinct steps of the metastatic cascade (Fig. 6F).

Discussion

A major goal of our study was to determine how breast cancer cells seed distant metastases. Our lineage analysis enabled us to identify polyclonal collective invasion strands, polyclonal disseminated tumor cell clusters in the stroma, polyclonal CTC clusters, and polyclonal micro- and macrometastases. Our findings, in conjunction with recent reports in CTC clusters (5), and genomic sequencing of metastases (7, 8), provide strong evidence for polyclonal seeding as a major mechanism for metastatic spread.

We next focused on the molecular features of the tumor cell clusters that give rise to polyclonal metastases. We have previously established that the cells leading collective invasion near uniformly express K14 (11). We reveal profound and systematic changes in the relative proportions of K14+ and K14− cells from micrometastatic to macrometastatic stages. We detect K14+ cells in disseminated tumor cell clusters, in intravascular tumor emboli, CTC clusters, and in micro- and macrometastases. Importantly, both CTC clusters and micrometastases are >20-fold enriched for K14+ cells relative to primary tumors or macrometastases. Thus, K14+ cells are significantly enriched in breast cancer cells during the phases of metastasis most associated with systemic spread. Conversely, K14− cells are significantly enriched in the phases of metastasis most associated with proliferation. Our in vivo data cannot distinguish between conversion of cells from a K14+ to a K14− state after arrival in the lung versus expansion of K14− cancer cells that arrived as a component of a mixed K14+/K14− cluster. However, our ex vivo assays provide clear evidence for interconversion between epithelial states in both directions. The molecular mechanisms that drive transitions between K14+ and K14− states are an important area for further study.

In our study, we also revealed transcriptomic differences between K14− and K14+ tumor cells and identified genes coding for protein complexes distinct to each compartment. Concordant with a recent report on plakoglobin, our data implicate the desmosome in polyclonal seeding (5). Intriguingly, K14+ cells are also enriched for hemidesmosome complex genes and genes encoding for proteinaceous extracellular matrix, and K14 expression is required for gene expression of multiple metastasiseffectors involved in niche remodeling (29, 37). It is likely that polyclonal tumor cell clusters provide an efficient nidus for interactions with collagen I, fibroblasts, macrophages, endothelial cells, and other tumor microenvironmental components in the multicellular seeding process (39-44).

Our data do not exclude the possibility of single-cell seeding events by either EMT or migratory stem cells. However, our lineage analysis does put an upper limit on the relative contribution of these events to metastasis in the MMTV-PyMT model. In agreement with our data, a recent study used lineage analysis in spontaneous mouse models of breast cancer to reveal that EMT does not significantly contribute to the formation of lung metastases in MMTV-PyMT mice, and that inhibition of EMT through miR-200 overexpression does not impair the ability of MMTV-PyMT tumor cells to form metastases (45). However, it remains technically prohibitive to image the transit of a cancer cell continuously from escape out of the primary tumor through to establishment of a distant site, and so some inference remains necessary to construct models of the process. Accordingly, it is important to acknowledge contrary observations. We observe K14− single cells in the mammary stroma and real-time intravital imaging was recently used to observe single MMTV-PyMT cancer cells intravasating at sites of macrophage–endothelial cell connections (44). Our data are compatible with a model in which K14 is required for collective invasion and dissemination, but not single cell dissemination. Furthermore, our data do not exclude the possibility of transitions between single cell and multicellular organization in the mammary stroma before intravasation. Future studies are needed to map the relative frequency of different single-cell and multicellular configurations and their molecular features across the entire mammary fat pad and in different cancer models

The simplest interpretation of our data is that breast cancer metastases form via the local dissemination, entry into circulation, and distal seeding of a multicellular cluster containing K14+ cancer cells (Figure S8). Within this framework, the survival advantage of multicellular organization provides a mechanism by which genetically distinct clones can jointly found a micrometastasis. Eradicating polyclonal micrometastases in the adjuvant setting will be particularly challenging when these founders have intrinsic differences in treatment sensitivity. Our findings also have potential clinical implications for patients with metastatic disease. CTC clusters have prognostic value in multiple tumor types (46). Finally, it will be important in future studies to determine how tumor cell clusters gain access to the lymphatic and venous circulation.

Materials and Methods

Mouse Lines and Breeding

Mice used in this study were backcrossed onto and maintained on the *FVB/NCrl* background in a specific pathogen-free facility. Animal protocols were approved by the Johns Hopkins University IACUC. *FVB/N-Tg(MMTV-PyVT)634Mul/J* (MMTV-PyMT) (23), *B6(D2)-Tg(CAGBrainbow1.0) 2Eggn/J* (Rainbow) (33), *Gt(ROSA)26Sortm1(CAG-Brainbow2.1)Cle/J* (Confetti) (32), *B6.129(Cg)-Gt(ROSA)26Sortm4(ACTB-tdTomato,-EGFP)Luo/J* (ROSAmT/mG) (63), and *NOD.Cg-Prkdcscid Il2rgtm1Wjl/SzJ* (NSG) mice were obtained from the Jackson Lab. K14-GFPactin mice (36) were a generous gift from Elaine Fuchs (Rockefeller University). *B6.129(ICR)-Tg(CAG-ECFP)CK6Nagy/*J (beta-actin-CFP) mice (64) were a gift from Mikala Egeblad (Cold Spring Harbor Laboratory). For multicolor lineage tracing experiments, MMTVPyMT mice were crossed with ROSA mT/mG mice, Confetti mice, Rainbow mice, and beta-actin-CFP mice and transplanted into NSG host mice. For sorting of K14- and K14+ cells, MMTV-PyMT mice were crossed with K14-GFPactin mice.

Isolation of Primary Mammary Tumor Organoids

Primary tumor organoids were isolated from mammary tumors by step-wise mechanical disruption, enzymatic digestion, and differential centrifugation according to our published protocols (17, 20). Tumors were harvested from 8-10 week old mice, minced with a scalpel, and digested for 1hr at 37°C in collagenase solution: (D-MEM (10565–018; Gibco® Life Technologies) with 2 mg/ml collagenase (C2139; Sigma-Aldrich), 2 mg/ml trypsin (27250–018; Gibco® Life Technologies), 5% fetal bovine serum (FBS) (F0926; Sigma-Aldrich), 5 μg/ml insulin (I9278; Sigma-Aldrich), and 50 **μ**g/ml gentamicin (15750;

Gibco® Life Technologies). The suspension was centrifuged at 1500 rpm to remove cellular debris, and the pellet was treated with 2U/μL DNase (D4263; Sigma-Aldrich) to separate out organoids. Tumor organoids were separated from single cells by differential centrifugation and counted under a microscope.

Mammary Fat Pad Transplantation

Tumor organoids from MMTV-PyMT;ROSA$^{mT/mG}$, MMTV-PyMT;Confetti, or MMTVPyMT;Rainbow were incubated with 1:50 adeno-CMV-Cre (1045; Vector BioLabs)/ D-MEM overnight in a non-adherent 96-well plate. Cre expression was induced successfully in more than 75% of the organoids. To wash out adeno-Cre, the samples were collected in a bovine serum albumin (BSA)-coated microcentrifuge tube and centrifuged at 1500 rpm for 10 mins. For intermediate mosaicism, tumor organoids were mixed 1:1 with unrecombined tumor organoids. Tumor organoids were resuspended in a 50% D-MEM/50% Matrigel (354230; Corning) solution at a density of 25–40 organoids/**μ**l and kept at 4°C during transplantation. We conducted orthotopic transplantations into 3-4 week old NSG mice in a sterile hood. The mice were anesthetized with 2.5% isoflurane, immobilized and the surgical site was made sterile using ethanol. A 1cm midline incision was made, the skin was retracted, and the no. 4 mammary gland was exposed. The fat pad proximal to the lymph node was removed. Using a syringe, 40 μl of the tumor organoid suspension was injected into the mammary fat pad. The skin was then locally infiltrated with 5–10 μl of 0.25% bupivacaine. The same procedure was repeated for the contralateral mammary gland. The surgical wounds were closed using 9mm autoclips and tissue glue. Triple antibiotic ointment was applied to the incision. The mice were closely monitored, and autoclips were removed 10 days post-surgery. Between 6-10 weeks, tumors and lungs from these mice were harvested.

DIC Imaging and Confocal Microscopy

Differential interference contrast (DIC) imaging of tumor organoids was conducted using a Zeiss Cell Observer system with a Zeiss AxioObserver Z1 and an AxioCam MRM camera (Carl Zeiss, Germany). Confocal imaging was conducted with a Zeiss 780 laser scanning confocal microscope (Carl Zeiss, Germany).

Immunofluorescence Staining

Tumors or lungs harvested from transplant mice were fixed in 4% or 1% paraformaldehyde respectively for 4 hours. They were then incubated in a 25% sucrose solution overnight, embedded in Tissue Tek® Optimal Cutting Temperature compound (O.C.T., Sakura) and frozen at -80°C. O.C.T. blocks were sectioned at 50 **µ**m thickness using a Leica cryostat (Leica Biosystems, Germany) set to -27°C. For antibody staining, the O.C.T. was removed by rinsing with PBS for 45 minutes. Samples were blocked for 2 hours with 10%FBS/1%BSA/PBS solution, incubated with the conjugated primary antibodies overnight at 4°C in 1%FBS/1%BSA/PBS solution, and rinsed two times in PBS for 10-20 minutes. Slides were optically cleared, mounted, and sealed with coverslips. Primary antibodies used were: Alexa Fluor® Phalloidin (Life Technologies) anti-K14 (PRB-155P; Covance), anti-E-Cad (24E10; Cell Signaling Technologies) and DAPI (D3571; Life Technologies). To label functional vasculature, 10ug of anti-CD31 (102416; Biolegend) and anti-CD144 (138108; Biolegend) antibodies were injected into the mouse by tail vein (65). After 20 minutes, mice were sacrificed and tumors and lungs were collected.

Isolation of CTCs

Approximately 500 **μ**L of blood was harvested from each mouse via the right atrium using a 20G needle (305176; BD Biosciences) and 1mL syringe (309659; BD Biosciences). Prior to cardiac puncture, tumors were mechanically palpated to liberate CTCs into the systemic circulation, as in (7). Blood was transferred to 1mL K2EDTA tubes (365974; BD Biosciences) and placed on an inverter to prevent clotting. Blood was mixed 1:2 with ACK Lysis Buffer (118-156-721; Quality Biological) and centrifuged at 500G for 5 mins. The pellet was washed with 500uL PBS without Mg^{+2}/Ca^{+2} (10010-023; Life Technologies) and centrifuged at 500G for an additional 5 mins. The pellet was resuspended in 450uL total volume with PBS without Mg^{+2}/Ca^{+2} and spread onto slides with a proprietary adhesion coating (0906000, Marienfeld). Cells were left to settle on the slide for 5 mins. The slide was then incubated at 37°C for 60 mins. Slide supernatant was discarded and adherent cells were fixed with 4% PFA at room temperature for 30 mins. Slides were then washed with PBS without Mg^{+2}/Ca^{+2} and permeabilized with 0.1% Triton-X at room temperature for 10 mins. Slides were again washed with PBS without Mg^{+2}/Ca^{+2} and then blocked at 37°C for 20 mins. with an Fc receptor blocking antibody diluted 1:20 (101320, BioLegend) in 10% Normal Goat Serum (50062Z, Life Technologies). Slides were incubated with conjugated primary antibodies diluted in PBS without Mg^{+2}/Ca^{+2} at 37°C for 1 hour. Antibodies used were pancytokeratin-AlexaFluor®488 (1:50; 4523S, Cell Signaling), Keratin 14-AlexaFluor®488 (1:250; PRB-155P, BioLegend), and CD45-AlexaFluor®647(1:50; 103124, BioLegend). Slides were washed with PBS without Mg^{+2}/Ca^{+2}, mounted and coverslipped using ProLong Diamond Anti-Fade with DAPI (P36971, Life Technologies) and 24x60 coverglass (12-545-M, Fisher). Slides were left to dry overnight in a dark chamber and imaged on a Zeiss Axio Imager Z2 (Carl Zeiss

Microscopy, Germany) using Metafer 5 software (v3.11.3) (MetaSystems,Newton, MA). High resolution 3D images were collected on a Zeiss 780 laser scanning confocal microscope (Carl Zeiss Microscopy, Germany).

FACS of Single K14- and K14+ Tumor Cells

MMTV-PyMT; K14-actin-GFP were harvested for tumor organoids. Organoids were subsequently dissociated to single cell suspensions in StemPro® Accutase® Cell Dissociation Reagent (A11105-01; Life Technologies) for 20 minutes. Cells were then re-suspended in HBSS/1%BSA. The resulting cell suspensions were filtered through 40 μm cell strainers and analyzed on a Beckman-Coulter MoFlo Cytometer by gating cellular distributions according to the eGFP reporter. Single cells and clusters were gated by FSLin vs Pulse Width. The nozzle size chosen for sorting was 100+ μm. Dead cells were excluded by propidium iodide fluorescence. For each condition, cells were sorted into 200 μL Matrigel and cultured in 24-well plates with D-MEM media supplemented with the growth factor basic human FGF (bFGF) (F0291; Sigma-Aldrich) at 37°C, 5%CO2. For the aggregation experiments, 10,000 single cells were sorted into D-MEM plus bFGF media and allowed to aggregate overnight in non-adherent well dishes at 37°C, 5%CO_2. The samples were then re-suspended into 200 μL Matrigel and plated as mentioned above. The samples were fixed at day 8 for counting of colonies. To confirm aggregation, fractions of single cell suspensions were incubated for 1 hour with 10μM Cell Tracker Green and Cell Tracker Red (C7025 and C34552, Life Technologies), respectively, prior to sorting. An equal number of red and green cells where plated for a total of 10,000 single cells per well. Cell aggregates were analyzed the following day.

Tail Vein Injections

NSG mice were injected with 200,000 single cells or an equivalent number of aggregated cells obtained from ROSA$^{mT/mG}$;MMTV-PyMT or Beta-actin-CFP;MMTV-PyMT tumor cells isolated by FACS. Lungs from these mice were harvested 3 weeks later, and lung metastases were counted under the dissection scope or by counting metastases from 50 **µ**m lung sections.

Lentiviral Transduction of Tumor Organoids for Tumor Transplantation

Lentiviral transduction of tumor organoids was conducted according to our published protocols (17). ~800 ROSAmT/mG;MMTV-PyMT organoids were resuspended in 100 µl of D-MEM/F12, and allowed to settle in a 96-well non-adherent dish for 1 hour at 37°C. The media was removed, and the organoids were infected with 50 µl of lentivirus (Mission® shRNA; Sigma-Aldrich) and 3 µl of ViroMag beads (VM4100; OZ Biosciences). The 96-well plate was incubated on top of a magnetic plate (MF10000; OZ Biosciences) at 37° C for 1.5 hours, then the magnetic plate was taken off and the 96-well plate was incubated overnight at 37°C. On day 2, 75 µl of media was removed and replaced with 200 µl of fresh FGF2 organoid media. On day 3, 175 µl of media was removed, and 175 µl of FGF2 organoid media supplemented with 2.5 nM bFGF and 4 µg/ml puromycin was added. After 3 days, the surviving organoids were collected for orthotopic transplantation into the #4 mammary fat pads of FVB host mice. Tumor dimensions were measured at regular intervals (1-2 times a week) using digital vernier calipers. For analysis of disseminated tumor cell clusters, tumor-stroma border of primary tumor sections were scanned for dissemination events and confirmed to be completely detached from the primary tumor by sequential z-stacks. Dissemination events were scored as single cells or clusters (2 cells or more).

Estimation of Local Mixing in the Primary Tumor

We took low-power montages of primary tumors in transplanted mice on a Zeiss 780 confocal microscope. Fiji custom scripts were written to binarize these images and extract the percentage of pixels that were green in color (%Green). We then divided images into 100x100 pixel grids (1.3mm x 1.3mm) and determined the probability of choosing two pixels of different colors in each grid. We defined %Local Mixing as two times the average probability of choosing two pixels of different colors averaged over all grids. Using robust linear regression, we then estimated the % of multicolored metastases at maximal local mixing for data in Figure 1E.

High-throughput RNA Sequencing of K14- and K14+ Tumor Cells

For each replicate, K14-actin-GFP;MMTV-PyMT tumor organoids were first dissociated into a single cell suspension, and then single K14- and K14+ cells were isolated by FACS. Four independent experiments were conducted. For each cell population, total RNA was extracted using TRizol (15596-026; Life Technologies) and RNeasy (QIAGEN). With 10-100 ng of RNA collected per sample, we generated barcoded NuGen RNA-seq v.2 libraries and ran paired end, 100-bp, 50-cycle sequencing on a HiSeq 2000 (Johns Hopkins Medical Institutions Deep Sequencing and Microarray Core Facility). Paired-end, non-strand–specific RNA-seq reads were mapped to the mouse reference genome (NCBI Build 37) using RNA-STAR version 2.3.0 (66). We achieved 80-85% read pair alignment to the reference genome and estimated the number of reads mapped to each gene using HTSeq version 0.6.1p1 (67), with gene coordinates from the reference genome Generic Feature Format file. Raw counts were normalized and p-values were calculated for paired sample differential expression using EdgeR (68). Genes were excluded which did not have at least

1 read per million in 4 of the 8 samples. This procedure yielded 12190 mapped genes, of which 11968 had gene annotation. Sequence data will be uploaded to the Sequence Read Archive. GO category enrichment was determined by DAVID Gene Set Analysis, version 6.7, using the functional annotation chart algorithm, mouse genome as background, and goterm_bp_fat, goterm_cc_fat, and goterm_mf_fat gene lists (39). P-values for module enrichment were calculated using a Fisher exact test (1561 of 11968 genes with FDR <0.05).

High-throughput RNA Sequencing of Luc-shRNA and K14-shRNA transduced tumor organoids

For each replicate, MMTV-PyMT tumor organoids were transduced with luciferase control shRNA or K14 shRNA, and selected with puromycin as we have done previously (17). Transduced organoids were embedded in 3D Matrigel and after 2 days in culture, harvested for RNA. Four independent experiments were conducted. For each condition, total RNA was extracted using RNeasy (QIAGEN). With 10–100 ng of RNA collected per sample, we generated cDNA using the SMART-Seq v4 Ultra Low Input RNA Kit for sequencing (Clontech), barcoded libraries with the Nextera XT DNA Library Preparation kit (Illumina), and ran paired end, 100-bp, 50-cycle sequencing on a HiSeq 2500 (GE Healthcare Seqwright). Paired-end, non-strand–specific RNAseq reads were mapped to the mouse reference genome (Genomic Reference Consortium build 38) using RNA-STAR (66). We achieved 73-86% read pair alignment to the reference genome and estimated the number of reads mapped to each gene using HTSeq (67), with gene coordinates from the reference genome Generic Feature Format file. Raw counts were normalized and p-values were calculated for paired sample differential expression using limma and voom (69, 70).

Genes were excluded which did not have at least 1 read per million in 4 of the 8 samples. This procedure yielded 13332 mapped genes, of which 12919 had gene annotation. For each replicate (1 to 4), the knockdown efficiency was determined by dividing the Krt14 transcript level in the K14- shRNA condition by the Krt14 transcript level in the Luc shRNA condition. A linear model was then fitted to the voomed expression data using a design matrix parameterizing batch effects and differences in knockdown efficiency between replicates. With this fitted model, genes were then ranked by p-value and FDR. The functional association network (Figure S7) was determined using the GeneMANIA web interface (71).

Mammosphere assay

For suspension mammosphere culture, MMTV-PyMT; K14-actin-GFP tumors were first dissociated into a single cell suspension, and then single K14 positive and K14 negative cells were isolated by FACS. Cells were plated on ultralow-adherence plates (Thermo Scientific) at 500 cells/cm^2 and 1000 cells/cm^2, respectively. Cells were culture in Basal Epicult-B mouse media (Stem Cell Technologies) containing B-supplement, 10ng/mL rhEGF, 10ng/mL rhbFGF, 4ug/mL heparin, and 1% penicillin/streptomycin. The number of spheres for each well was counted under the microscope on Day 7. The average number of spheres was compared across cell types and densities using the Mann Whitney test.

Statistics

Statistical analysis was conducted using the statistical program R or Graphpad Prism. For all boxplots, the whiskers represent the 5th and 95th percentiles. All tests used and P values are specified in the figure legends. $P < 0.05$ was considered significant.

Acknowledgments

We thank members of the Ewald laboratory for helpful comments on the manuscript. We thank B. Stanger and R. Maddipati for sharing unpublished data. We thank Hao Zhang of the Johns Hopkins School of Public Health Flow Cytometry Core Facility for assistance with FACS experiments. We thank Haiping Hao of the Johns Hopkins Medical Institutions Deep Sequencing and Microarray Core Facility for assistance with high throughput RNA seq experiments. K.J.C. is supported by a postdoctoral fellowship from the U.S. Department of Defense (W81XWH-12-1-0018 to K.J.C) and a Burroughs Wellcome Fund Career Award for Medical Scientists. A.J.E. is supported by a Research Scholar Grant (RSG-12-141-01-CSM) from the American Cancer Society, by funds from the NIH/NCI (P30 CA006973), by a grant from the Mary Kay Ash Foundation (036-13), by funds from the Cindy Rosencrans Fund for Triple Negative Breast Cancer Research, by a Research Leadership Award from the Metastatic Breast Cancer Network, and by an award from The Pink Agenda and The Breast Cancer Research Foundation.

Author contributions

K.J.C., V.P., V.S., K.S., A.N.F., M.A.G., K.J.P., J.S.B., and A.J.E. de- signed research; K.J.C., V.P., V.S., K.S., J.D.C., A.N.F., M.A.G., and J.E.V. performed re- search; K.J.C., J.D.C., M.A.G., J.E.V., K.J.P., and J.S.B. contributed new reagents/analytic tools; K.J.C., V.P., V.S., K.S., J.D.C., A.N.F., M.A.G., J.E.V., J.S.B., and A.J.E. analyzed data; and K.J.C. and A.J.E. wrote the paper.

References

1. Hanahan D, Weinberg RA (2011) Hallmarks of cancer: The next generation. Cell 144(5):646–674.

2. Moore GE, Sandberg AA, Watne AL (1960) The comparative size and structure of tumor cells and clumps in the blood, bone marrow, and tumor imprints. Cancer 13:111–117.

3. Liotta LA, Saidel MG, Kleinerman J (1976) The significance of hematogenous tumor cell clumps in the metastatic process. Cancer Res 36(3):889–894.

4. Hou JM, et al. (2012) Clinical significance and molecular characteristics of circulating tumor cells and circulating tumor microemboli in patients with small-cell lung cancer. J Clin Oncol 30(5):525–532.

5. Aceto N, et al. (2014) Circulating tumor cell clusters are oligoclonal precursors of breast cancer metastasis. Cell 158(5):1110–1122.

6. Maddipati R, Stanger BZ (2015) Pancreatic cancer metastases harbor evidence of polyclonality. Cancer Discov 5(10):1086–1097.

7. McFadden DG, et al. (2014) Genetic and clonal dissection of murine small cell lung carcinoma progression by genome sequencing. Cell 156(6):1298–1311.

8. Gundem G, et al.; ICGC Prostate UK Group (2015) The evolutionary history of lethal metastatic prostate cancer. Nature 520(7547):353–357.

9. Bronsert P, et al. (2014) Cancer cell invasion and EMT marker expression: A three-dimensional study of the human cancer-host interface. J Pathol 234(3):410–422.

10. Friedl P, Locker J, Sahai E, Segall JE (2012) Classifying collective cancer cell invasion. Nat Cell Biol 14(8):777–783.

11. Cheung KJ, Gabrielson E, Werb Z, Ewald AJ (2013) Collective invasion in breast cancer requires a conserved basal epithelial program. Cell 155(7):1639–1651.

12. Cheung KJ, Ewald AJ (2014) Illuminating breast cancer invasion: Diverse roles for cell- cell interactions. Curr Opin Cell Biol 30:99–111.

13. Friedl P, Zänker KS, Bröcker EB (1998) Cell migration strategies in 3-D extracellular matrix: Differences in morphology, cell matrix interactions, and integrin function. Microsc Res Tech 43(5):369–378.

14. Nguyen-Ngoc KV, et al. (2012) ECM microenvironment regulates collective migration and local dissemination in normal and malignant mammary epithelium. Proc Natl Acad Sci USA 109(39):E2595–E2604.

15. Friedl P, et al. (1995) Migration of coordinated cell clusters in mesenchymal and epithelial cancer explants in vitro. Cancer Res 55(20):4557–4560.

16. Lin EY, et al. (2003) Progression to malignancy in the polyoma middle T oncoprotein mouse breast cancer model provides a reliable model for human diseases. Am J Pathol 163(5):2113–2126.

17. Guy CT, Cardiff RD, Muller WJ (1992) Induction of mammary tumors by expression of polyomavirus middle T oncogene: A transgenic mouse model for metastatic disease. Mol Cell Biol 12(3):954–961.

18. Herschkowitz JI, He X, Fan C, Perou CM (2008) The functional loss of the retinoblastoma tumour suppressor is a common event in basal-like and luminal B breast car- cinomas. Breast Cancer Res 10(5):R75.

19. Snippert HJ, et al. (2010) Intestinal crypt homeostasis results from neutral competition between symmetrically dividing Lgr5 stem cells. Cell 143(1):134–144.
20. Tabansky I, et al. (2013) Developmental bias in cleavage-stage mouse blastomeres. Curr Biol 23(1):21–31.
21. Kim MY, et al. (2009) Tumor self-seeding by circulating cancer cells. Cell 139(7):1315–1326.
22. Kondo J, et al. (2011) Retaining cell-cell contact enables preparation and culture of spheroids composed of pure primary cancer cells from colorectal cancer. Proc Natl Acad Sci USA 108(15):6235–6240.
23. Vaezi A, Bauer C, Vasioukhin V, Fuchs E (2002) Actin cable dynamics and Rho/Rock orchestrate a polarized cytoskeletal architecture in the early steps of assembling a stratified epithelium. Dev Cell 3(3):367–381.
24. Cleary AS, Leonard TL, Gestl SA, Gunther EJ (2014) Tumour cell heterogeneity maintained by cooperating subclones in Wnt-driven mammary cancers. Nature 508(7494):113–117.
25. Gupta PB, et al. (2011) Stochastic state transitions give rise to phenotypic equilibrium in populations of cancer cells. Cell 146(4):633–644.
26. Huang W, Sherman BT, Lempicki RA (2009) Systematic and integrative analysis of large gene lists using DAVID bioinformatics resources. Nat Protoc 4(1):44–57.
27. Kang Y, et al. (2003) A multigenic program mediating breast cancer metastasis to bone. Cancer Cell 3(6):537–549.
28. Malanchi I, et al. (2012) Interactions between cancer stem cells and their niche govern metastatic colonization. Nature 481(7379):85–89.
29. Oskarsson T, et al. (2011) Breast cancer cells produce tenascin C as a metastatic niche component to colonize the lungs. Nat Med 17(7):867–874.
30. Soady KJ, et al. (2015) Mouse mammary stem cells express prognostic markers for triple-negative breast cancer. Breast Cancer Res 17:31.
31. Spike BT, et al. (2012) A mammary stem cell population identified and characterized in late embryogenesis reveals similarities to human breast cancer. Cell Stem Cell 10(2):183–197.
32. Broussard JA, Getsios S, Green KJ (2015) Desmosome regulation and signaling in disease. Cell Tissue Res 360(3):501–512.
33. Sethi N, Dai X, Winter CG, Kang Y (2011) Tumor-derived JAGGED1 promotes osteo-lytic bone metastasis of breast cancer by engaging notch signaling in bone cells. Cancer Cell 19(2):192–205.
34. Tanaka K, et al. (2000) Expression of survivin and its relationship to loss of apoptosis in breast carcinomas. Clin Cancer res 6(1):127–134.
35. Devoogdt N, et al. (2003) Secretory leukocyte protease inhibitor promotes the tumorigenic and metastatic potential of cancer cells. Proc Natl Acad Sci USA 100(10):5778–5782.
36. Goetz JG, et al. (2011) Biomechanical remodeling of the microenvironment by stromal caveolin-1 favors tumor invasion and metastasis. Cell 146(1):148–163.
37. Gupta GP, et al. (2007) Mediators of vascular remodelling co-opted for sequential steps in lung metastasis. Nature 446(7137):765–770.

38. Pan D, et al. (2015) The CBM complex underwrites NF-kappaB activation to promote HER2-associated tumor malignancy. Mol Cancer Res, 10.1158/1541-7786.MCR-15-0229-T.
39. Joyce JA, Pollard JW (2009) Microenvironmental regulation of metastasis. Nat Rev Cancer 9(4):239–252.
40. Condeelis J, Pollard JW (2006) Macrophages: Obligate partners for tumor cell migration, invasion, and metastasis. Cell 124(2):263–266.
41. Calvo F, et al. (2013) Mechanotransduction and YAP-dependent matrix remodelling is required for the generation and maintenance of cancer-associated fibroblasts. Nat Cell Biol 15(6):637–646.
42. Egeblad M, Rasch MG, Weaver VM (2010) Dynamic interplay between the collagen scaffold and tumor evolution. Curr Opin Cell Biol 22(5):697–706.
43. Stacker SA, Achen MG, Jussila L, Baldwin ME, Alitalo K (2002) Lymphangiogenesis and cancer metastasis. Nat Rev Cancer 2(8):573–583.
44. Harney AS, et al. (2015) Real-time imaging reveals local, transient vascular permeability, and tumor cell intravasation stimulated by TIE2hi macrophage-derived VEGFA. Cancer Discov 5(9):932–943.
45. Fischer KR, et al. (2015) Epithelial-to-mesenchymal transition is not required for lung metastasis but contributes to chemoresistance. Nature 527(7579):472–476.
46. Mina LA, Sledge GW, Jr (2011) Rethinking the metastatic cascade as a therapeutic target. Nat Rev Clin Oncol 8(6):325–332.
47. Muzumdar MD, Tasic B, Miyamichi K, Li L, Luo L (2007) A global double-fluorescent Cre reporter mouse. Genesis 45(9):593–605.
48. Hadjantonakis AK, Macmaster S, Nagy A (2002) Embryonic stem cells and mice expressing different GFP variants for multiple non-invasive reporter usage within a single animal. BMC Biotechnol 2:11.
49. Bruns I, et al. (2014) Megakaryocytes regulate hematopoietic stem cell quiescence through CXCL4 secretion. Nat Med 20(11):1315–1320.
50. Dobin A, et al. (2013) STAR: Ultrafast universal RNA-seq aligner. Bioinformatics 29(1):15–21.
51. Anders S, et al. (2013) Count-based differential expression analysis of RNA sequencing data using R and Bioconductor. Nat Protoc 8(9):1765–1786.
52. Smyth GK (2004) Linear models and empirical bayes methods for assessing differential expression in microarray experiments. Stat Appl Genet Mol Biol 3:Article3.
53. Warde-Farley D, et al. (2010) The GeneMANIA prediction server: Biological network integration for gene prioritization and predicting gene function. Nucleic Acids Res 38(Web Server issue):W214–W220.

Figure 3-1. Multicellular seeding is a frequent mechanism for distant metastasis.

(A) Schema of multicolor lineage tracing assay. ROSAmT/mG;MMTV-PyMT tumor organoids were treated with adenoviral Cre to induce recombination from membrane tdTomato (mTomato) to membrane eGFP (mGFP). Mosaic tumor organoids were then transplanted into nonfluorescent NSG host mice. After 6–8 wk, lungs of these mice were harvested. If metastases arise exclusively from single-cell seeding, there should be only single color metastases. In contrast, multicellular seeding should produce metastases with both colors. (B) Representative micrographs of polyclonal lung me- tastases of different sizes. n = 355 polyclonal metastases, across 16 mice and 4 independent experiments. (C) Representative micrograph of a mosaic tumor organoid treated with adeno-Cre and grown in 3D Matrigel with intermixing of red and green tumor cell clones. (D and E) Representative micrographs of primary tumors arising from mosaic tumor organoids transplanted into NSG host mice. Primary tumors varied in their local mixing of red and green tumor cell clones (local mixing %). These differences correlated with the percentage of multicolored metastases detected in the lung (% multicolored). n = 12 mice, 4 independent experiments, 4,072 metastases. Correlation determined by Spearman rank test for samples with more than five lung metastases per mouse. (Scale bars, 20 μm in B and C, and 2 mm in D.)

Figure 3-1.

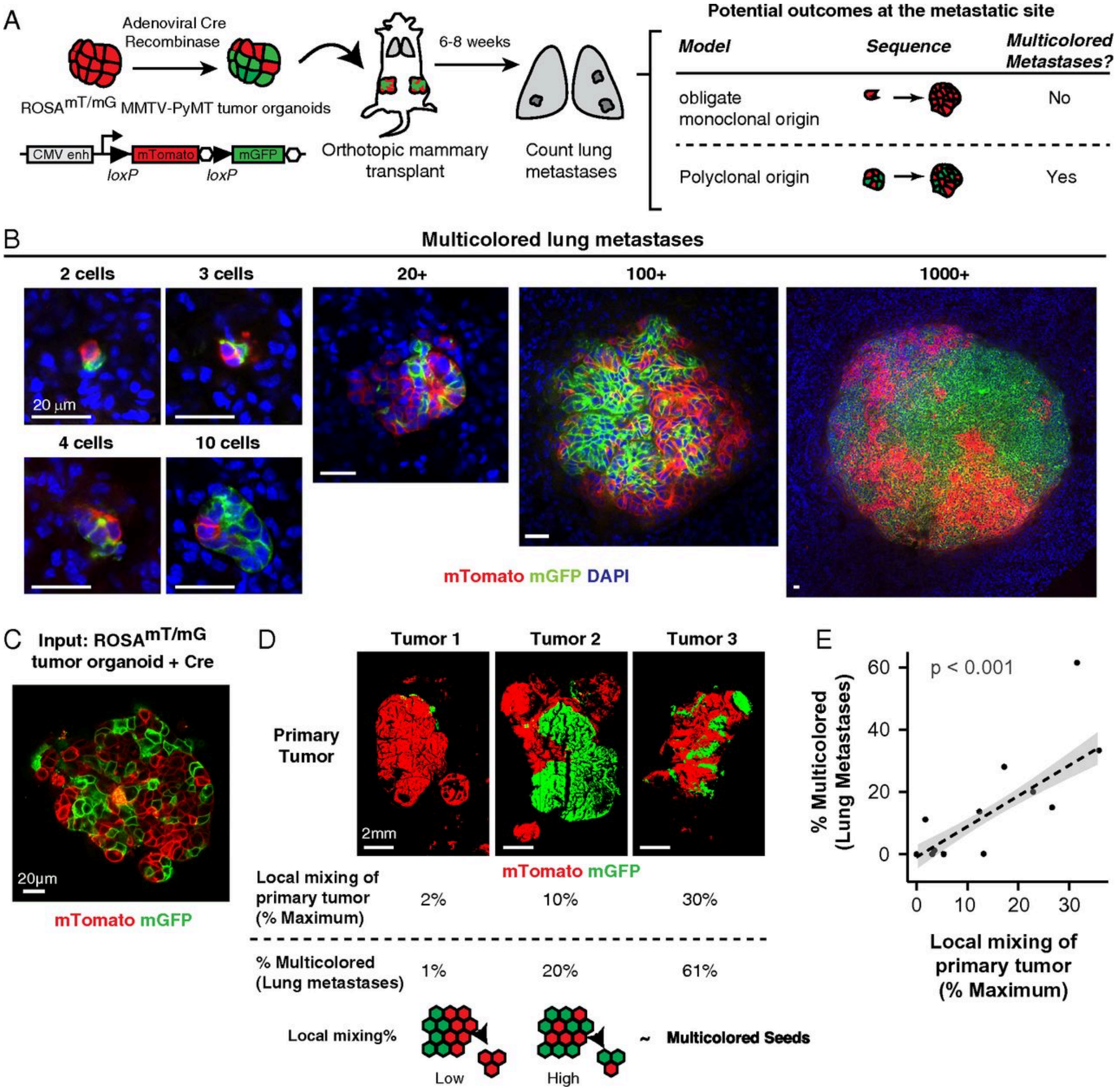
A
Adenoviral Cre Recombinase
ROSAmT/mG MMTV-PyMT tumor organoids
CMV enh
mTomato
mGFP
loxP
loxP
Orthotopic mammary transplant
6-8 weeks
Count lung metastases
Potential outcomes at the metastatic site
Model
Sequence
Multicolored Metastases?
obligate monoclonal origin
No
Polyclonal origin
Yes
B
Multicolored lung metastases
2 cells
3 cells
20+
100+
1000+
20 μm
4 cells
10 cells
mTomato mGFP DAPI
C
Input: ROSAmT/mG tumor organoid + Cre
20μm
mTomato mGFP
D
Tumor 1
Tumor 2
Tumor 3
Primary Tumor
2mm
mTomato mGFP
Local mixing of primary tumor (% Maximum)
2%
10%
30%
% Multicolored (Lung metastases)
1%
20%
61%
Local mixing%
Low
High
~ Multicolored Seeds
E
p < 0.001
60
40
20
0
% Multicolored (Lung Metastases)
0
10
20
30
Local mixing of primary tumor (% Maximum)

Figure 3-2. Direct observation of polyclonal collective invasion, polyclonal disseminated tumor emboli, and polyclonal CTC clusters.

(A) Representative micro- graph of polyclonal collective invasion arising from mosaic ROSAmT/mG;MMTV-PyMT transplanted tumors stained with phalloidin (F-actin) and DAPI (n =75 units, 5 tumors). (B) Schema of two potential outcomes for disseminated tumor cell clusters at the tumor stromal interface. (C) Representative micrographs of a polyclonal disseminated tumor cluster (yellow arrow) in the x-y plane with successive images along the z axis (Left panels) and reconstructed 3D image (Right) (n = 25 units, 5 tumors). (D) Representative micrograph of a polyclonal disseminated tumor embolus contained within a vessel. The transplanted tumor is composed of mTomato+ and CFP+ tumor cells. Injection with VE-Cadherin and CD31 fluorescently labeled antibodies marked functional vasculature. (E) Representative micrographs demonstrating E-cadherin+ polyclonal collective invasion, dissemination, intravascular embolus (from left to right). Yellow hash marks: vessel lumen. (F) Representative micrographs of CTC clusters composed of mTomato+ and CFP+ tumor cells and stained for K14 and DAPI (n = 1 multicolored cluster, n = 13 mTomato+ clusters, n = 2 CFP+ cluster). (G) The number of events for each CTC cluster size is presented as a histogram (n = 134 events, 3 transplanted mice). (H) The median percentage of cells that are K14+ in CTCs of different cluster sizes are presented as a boxplot (n = 17 clusters). [Scale bars, 2 mm (A, Left), 40 µm (A, Right), 20 µm (C–E), and 10 µm (F).]

Figure 3-2.

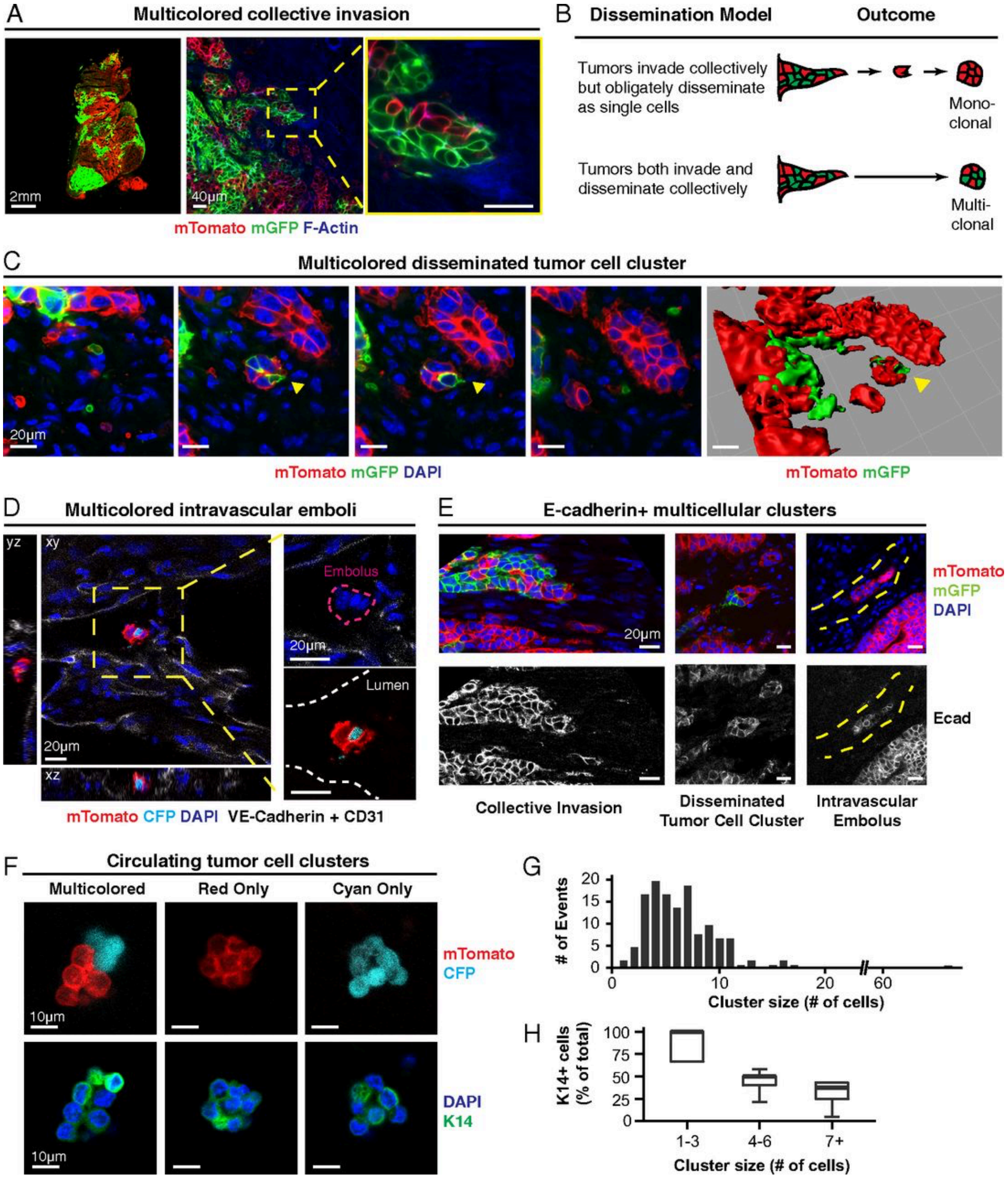
A
Multicolored collective invasion
2mm
40µm
mTomato mGFP F-Actin
B
Dissemination Model
Outcome
Tumors invade collectively but obligately disseminate as single cells
Mono-clonal
Tumors both invade and disseminate collectively
Multi-clonal
C
Multicolored disseminated tumor cell cluster
20µm
mTomato mGFP DAPI
mTomato mGFP
D
Multicolored intravascular emboli
yz
xy
xz
20µm
Embolus
20µm
Lumen
mTomato CFP DAPI VE-Cadherin + CD31
E
E-cadherin+ multicellular clusters
20µm
mTomato
mGFP
DAPI
Ecad
Collective Invasion
Disseminated Tumor Cell Cluster
Intravascular Embolus
F
Circulating tumor cell clusters
Multicolored
Red Only
Cyan Only
10µm
mTomato
CFP
10µm
DAPI
K14
G
# of Events
20
15
10
5
0
0
10
20
60
Cluster size (# of cells)
H
K14+ cells (% of total)
100
75
50
25
0
1-3
4-6
7+
Cluster size (# of cells)

Figure 3-3. Clustered Organization Significantly Promotes Colony Formation in *Ex vivo* Culture and Metastasis Formation *In-Vivo*

(A) FACS-sorted single tumor cells from MMTV-PyMT tumor organoids were either (i) immediately plated into Matrigel or (ii) first incubated in a non-adherent dish for 24 hours to promote cell re-aggregation and then subsequently plated into Matrigel. The same numbers of cells were used in each condition. Colony formation was assessed at Day 8. Representative images are shown of a single cell at Day 0 and a re-aggregated cell cluster at Day 1 and a colony formed at Day 8. (B) The median number of colonies per 10000 input cells in single cell and re-aggregated cell conditions, presented as boxplots (N=4 independent experiments). The same numbers of cells were used in each condition. Significance determined by Wilcoxon rank sum test. $P < 0.05$. (C) Schema of re aggregation tail vein assay. mTomato+ tumor organoids were dissociated as in (A) to generate two input suspensions, single cells and re-aggregated cells, for tail vein injection into NSG mice. The same numbers of cells were used in each condition. After 3 weeks, lungs were visually inspected for mTomato+ metastases. (D) Representative micrographs of lung metastases in mice injected with single cells or reaggregated cells under the dissecting scope viewed under bright light (upper panel) or for mTomato (lower panel). (E) The median number of lung metastases for mice injected with single cells or re aggregated cells with data presented as boxplots (2 independent experiments, single cell suspension, N=10 mice, aggregated cell suspension, N=13 mice). Significance determined by Wilcoxon rank sum test. $P < 0.001$. Scale bars, 20 μm in (A) and 500 μm in (D).

Figure 3-3.

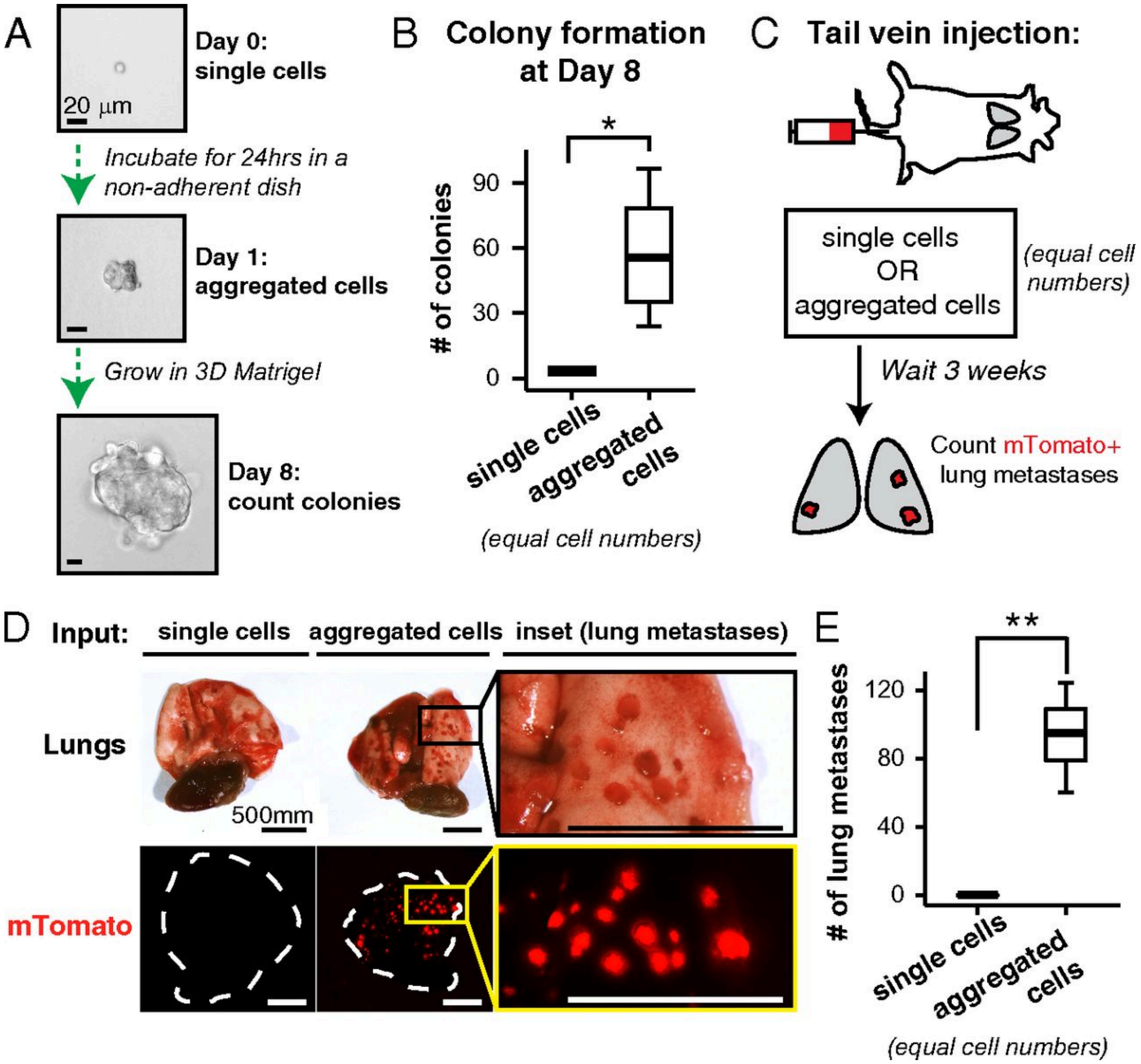
A
Day 0:
single cells
20 μm
Incubate for 24hrs in a
non-adherent dish
Day 1:
aggregated cells
Grow in 3D Matrigel
Day 8:
count colonies
B
Colony formation
at Day 8
*
# of colonies
90
60
30
0
single cells
aggregated
cells
(equal cell numbers)
C
Tail vein injection:
single cells
OR
aggregated cells
(equal cell
numbers)
Wait 3 weeks
Count mTomato+
lung metastases
D
Input:
single cells
aggregated cells
inset (lung metastases)
Lungs
500mm
mTomato
E
**
# of lung metastases
120
80
40
0
single cells
aggregated
cells
(equal cell numbers)

Figure 3-4. Micrometastases are enriched for K14+ cells relative to macrometastases. (A-C) The percentage of cells that are K14+ varies inversely with the size of the metastasis. Representative micrographs of lung micrometastases of different sizes (A) and a lung macrometastasis (B) stained for K14 and DAPI. (C) The median percentage of cells that are K14+ at each stage of metastasis presented as a boxplot ($n = 9$ primary tumors, $n = 49$ micrometastases, $n = 18$ mac- rometastases). The median percentages for each condition are denoted in red. $P < 0.05$, $P < 0.01$, $P < 0.001$. (D) Schema of in vitro model of colonization. K14+ and K14− single-cell suspensions were isolated by FACS from K14-actin-GFP;MMTV-PyMT tumors. In addition, single-cell suspensions were aggregated into clusters, using as input either (i) K14+ cells, (ii) K14− cells, or (iii) a 50:50 ratio of both K14+ and K14− cells (both). (E) The median number of colonies formed at day 8 is presented as boxplots (n = the number of independent experiments. K14− single cells: $n = 8$, K14+ single cells: $n = 8$, K14− clusters: $n = 3$, K14+ clusters: $n = 3$, mixtures of both cell types: $n = 3$). $P < 0.005$. (F) K14+ and K14− cells and clusters generate colonies that are morphologically similar. Representative images of colonies of different sizes formed at day 8, stained for K14 and F-actin. (G) The median percentage of cells that are K14+ in different dissociated tumor cell clusters grown in Matrigel presented as a boxplot ($n = 4{,}547$ cells in 103 colonies). The median percentages for each condition are denoted in red. $P < 0.001$. $P < 10-7$. (Scale bars, 10 μm in A, 100 μm in B, and 20 μm in F.)

Figure 3-4.

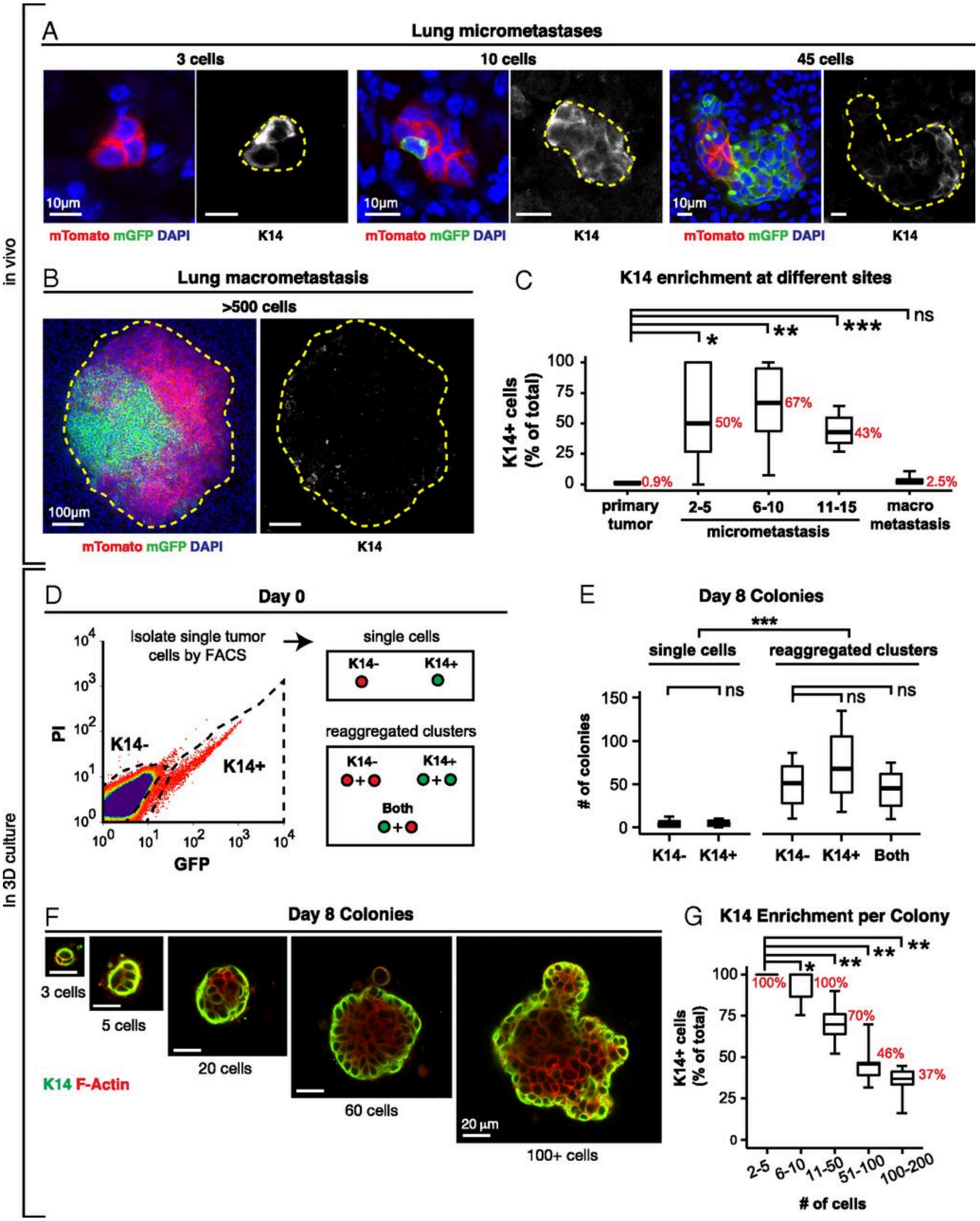
in vivo
In 3D culture
A
Lung micrometastases
3 cells
10 cells
45 cells
10μm
mTomato mGFP DAPI
K14
B
Lung macrometastasis
>500 cells
100μm
C
K14 enrichment at different sites
K14+ cells (% of total)
100
75
50
25
0
*
**
***
ns
0.9%
50%
67%
43%
2.5%
primary tumor
2-5
6-10
11-15
micrometastasis
macro metastasis
D
Day 0
Isolate single tumor cells by FACS
PI
GFP
10^0
10^1
10^2
10^3
10^4
K14-
K14+
single cells
reaggregated clusters
K14-
K14+
Both
E
Day 8 Colonies
***
single cells
reaggregated clusters
# of colonies
150
100
50
0
ns
K14-
K14+
Both
F
Day 8 Colonies
3 cells
5 cells
20 cells
60 cells
100+ cells
20 μm
K14 F-Actin
G
K14 Enrichment per Colony
K14+ cells (% of total)
100
75
50
25
0
*
**
**
**
100%
100%
70%
46%
37%
2-5
6-10
11-50
51-100
100-200
# of cells

Figure 3-5. The transcriptional program of K14+ tumor cells is enriched for desmosome and hemidesmosome adhesion complex genes, and depleted for genes involved in MHC class II immunosurveillance.

(A) K14- and K14+ cells were isolated by FACS from K14-actin-GFP;MMTV-PyMT tumors and the relative mRNA expression of K14 relative to GAPDH was determined by quantitative RTPCR. The relative mRNA expression is presented as a boxplot (N=4 independent experiments). P-value determined by Wilcoxon rank sum test. (B) Heatmap of the most differentially expressed genes determined by RNA sequencing of K14- and K14+ cells at a genome-wide significance of $P < 10^{-6}$. (C-C') Genes that encode for desmosome, hemidesmosome, and MHC class II antigen presentation protein complexes are differentially expressed and co-regulated in K14+ cells.

Figure 3-5.

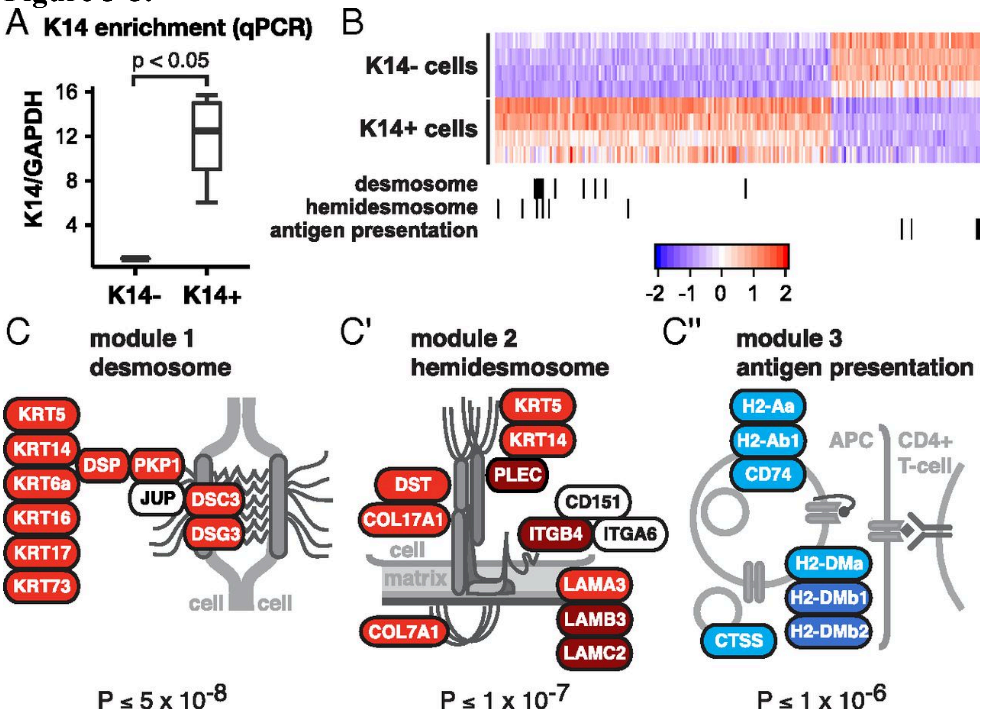
A
K14 enrichment (qPCR)
p < 0.05
K14/GAPDH
16
12
8
4
K14-
K14+
B
K14- cells
K14+ cells
desmosome
hemidesmosome
antigen presentation
-2
-1
0
1
2
C
module 1
desmosome
KRT5
KRT14
KRT6a
KRT16
KRT17
KRT73
DSP
PKP1
JUP
DSC3
DSG3
cell
cell
P ≤ 5 x 10-8
C'
module 2
hemidesmosome
KRT5
KRT14
PLEC
DST
COL17A1
CD151
ITGB4
ITGA6
cell
matrix
LAMA3
LAMB3
LAMC2
COL7A1
P ≤ 1 x 10-7
C''
module 3
antigen presentation
H2-Aa
H2-Ab1
CD74
APC
CD4+
T-cell
H2-DMa
H2-DMb1
H2-DMb2
CTSS
P ≤ 1 x 10-6

Figure 3-6. K14 is required for distant metastasis and regulates the expression of multiple metastasis effectors.

(A) Schema to test the in vivo requirement for K14 in metastasis. Fluorescent mTomato+ tumor organoids were transduced with either lentiviral Luc-shRNA or K14-shRNA, selected with puromycin, and transplanted into the cleared mammary fat pads of nonfluorescent congenic hosts. Mice were harvested from 6 to 8 wk and lungs were sectioned and counted for mTomato+ lung metastases. (B and C) Median tumor size in cubic millimeters and number of lung metastases for Luc-shRNA and K14-shRNA tumors, with data presented as boxplots ($n = 11$ mice for Luc-shRNA, $n = 10$ mice for K14-shRNA). $P < 0.05$. (D) Heatmap of the most differentially expressed genes determined by RNA se- quencing of luciferase control knockdown and K14 knockdown tumor organoids at an FDR < 0.05. (D′) Scatterplot of correlation of transcript expression of top ranked genes versus Krt14. (E) Scatterplot of the most differentially expressed genes with twofold or greater significant enrichment in K14+ cells or K14− cells and whose gene expression was significantly associated with K14 transcript levels (FDR < 0.05 for both datasets). Krt14 is highlighted in green. Published metastasis genes reported in red. (F) Schema of metastasis genes enriched in K14+ cells and regulated by Krt14 expression.

Figure 3-6.

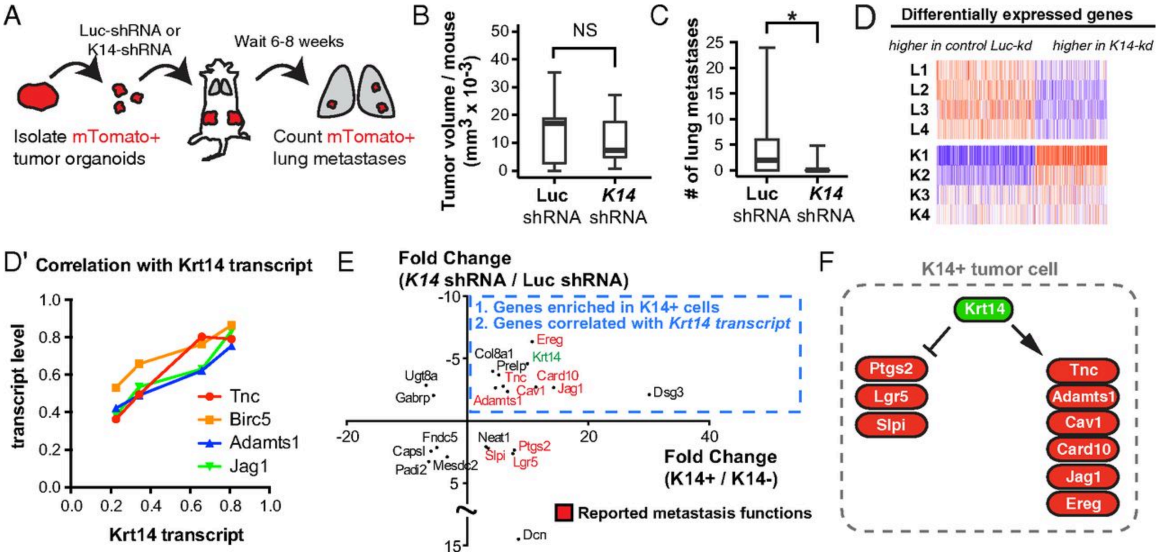
A
Luc-shRNA or
K14-shRNA
Wait 6-8 weeks
Isolate mTomato+
tumor organoids
Count mTomato+
lung metastases
B
Tumor volume / mouse
(mm3 x 10-3)
50
40
30
20
10
0
NS
Luc
shRNA
K14
shRNA
C
# of lung metastases
25
20
15
10
5
0
*
Luc
shRNA
K14
shRNA
D
Differentially expressed genes
higher in control Luc-kd
higher in K14-kd
L1
L2
L3
L4
K1
K2
K3
K4
D'
Correlation with Krt14 transcript
transcript level
1.0
0.8
0.6
0.4
0.2
0.0
0.0
0.2
0.4
0.6
0.8
1.0
Krt14 transcript
Tnc
Birc5
Adamts1
Jag1
E
Fold Change
(K14 shRNA / Luc shRNA)
-10
-5
5
15
-20
20
40
1. Genes enriched in K14+ cells
2. Genes correlated with Krt14 transcript
Ereg
Col8a1
Krt14
Prelp
Ugt8a
Tnc
Card10
Cav1
Jag1
Dsg3
Gabrp
Adamts1
Fndc5
Neat1
Capsl
Ptgs2
Slpi
Padi2
Mesdc2
Lgr5
Fold Change
(K14+ / K14-)
Reported metastasis functions
Dcn
F
K14+ tumor cell
Krt14
Ptgs2
Lgr5
Slpi
Tnc
Adamts1
Cav1
Card10
Jag1
Ereg

Supplemental Figure 3-1. Lineage tracing in Confetti and Rainbow mice identify multicolored lung metastases in the MMTV-PyMT model.

(A, Left) Schema of multicolor lineage-tracing assay to determine clonality of metastases using the Confetti reporter. Confetti;MMTV-PyMT tumor organoids were treated with adeno-Cre to induce recombination to one of four colors: nuclear-GFP, membrane CFP, cytoplasmic YFP, or cytoplasmic RFP. Mosaic tumor organoids were then transplanted into nonfluorescent NSG host mice. After 6–8 wk, the lungs were harvested, and the number of multicolored lung metastases was counted. (Right) Representative Adeno-Cre treated Confetti tumor organoid grown in 3D Matrigel. (B, Left) Representative micrograph of no-color dominance in a transplanted Confetti;MMTV-PyMT tumor stained with phalloidin (F-actin) and DAPI. (Lower) Inset of region denoted by star in Upper panel, showing solid boundary between RFP+ and no-colored cells. (Right) Median percentage area of the primary tumor occupied by no-color tumor cells presented as a dot plot (n = 30 tumors, 15 mice, 3 independent experiments). (C, Left) Representative multicolored lung metastasis in a transplanted Confetti;MMTV-PyMT mouse. Lung sections were stained with phalloidin (F-actin) and DAPI. (Right) Bar graph of color distribution of lung metastases (n = 11 metastases, 2 mice). (D, Left) Schema of multicolor lineage-tracing assay to determine clonality of metastases using the Rainbow reporter. Rainbow; MMTV-PyMT tumor organoids were treated with adeno-Cre to induce recombination to 1 of 21 potential colors. Mosaic tumor organoids were then transplanted into nonfluorescent NSG host mice. After 6-8 wk, the lungs were harvested and the number of multicolored lung metastases were counted. (Right) representative Adeno-Cre treated Rainbow tumor organoid grown in 3D Matrigel. (E, Left) Representative micrograph of no-color dominance in Rainbow;MMTV-PyMT transplanted tumor stained with phalloidin (F-actin) and DAPI. (Lower) Inset of region marked with star in Upper panel, showing solid boundary between RFP+ and no-colored cells. (Right) Median percentage area of the primary tumor occupied by no-color tumor cells presented as a dot plot (n = 26 tumors, 13 mice, 2 independent experiments). (F, Left) Representative multicolored lung metastasis identified in a Rainbow;MMTV-PyMT transplanted mouse. Lung sections were stained with phalloidin (F-actin) and DAPI. (Right) Bar graph of color distribution of lung metastases (n = 83 metastases, 6 mice, 2 independent experiments). [Scale bars, 50 µm (A, B, Lower, D, E, Lower), 2 mm (B, Upper, and E, Upper), and 100 µm (C and F).]

Supplemental Figure 3-1.

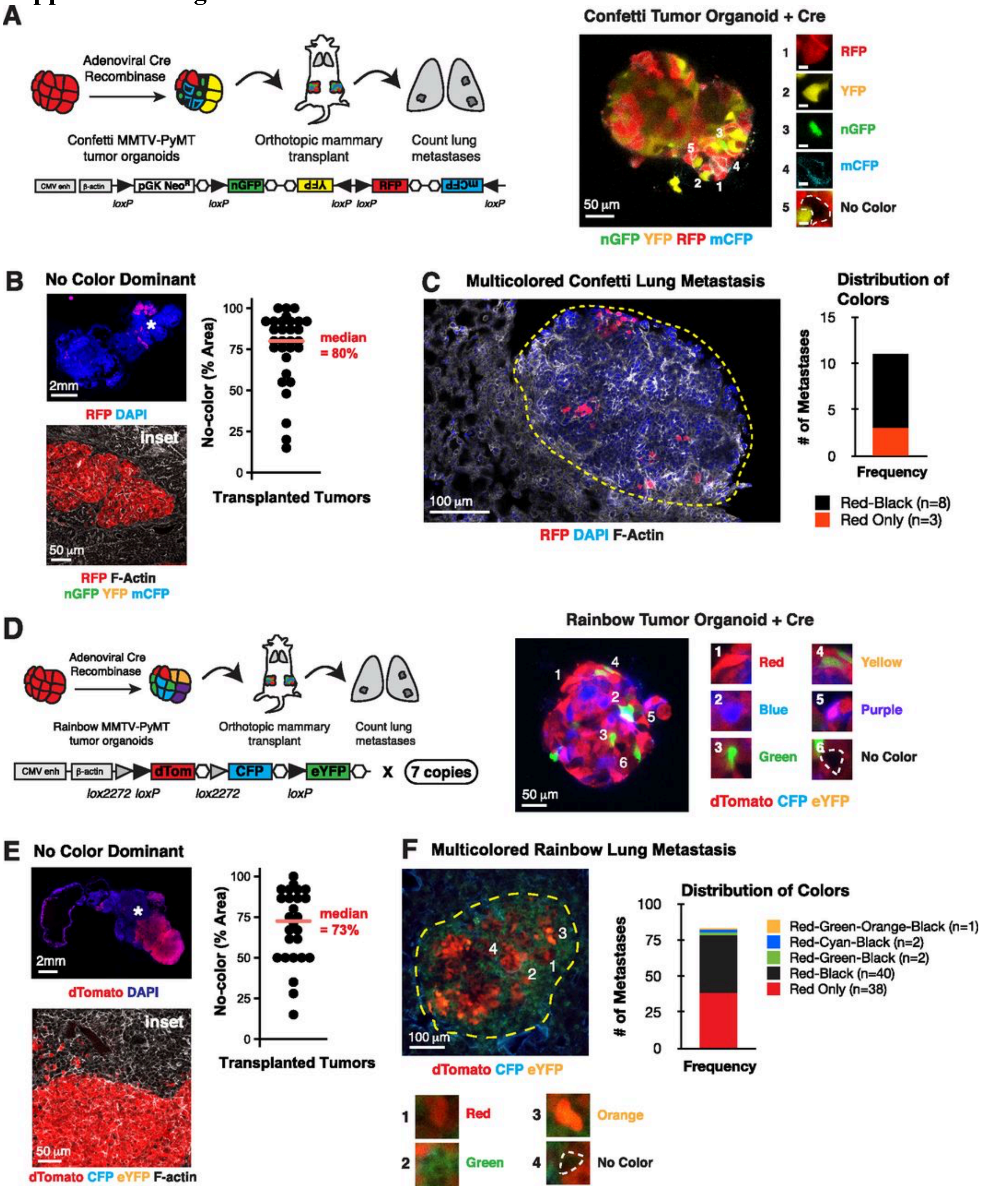

Supplemental Figure 3-2. Polyclonal metastases arise from multicellular seeds not by serial seeding of single tumor cells.

(A) Schema of transplant assay to model the contribution of serial seeding to polyclonal metastases. mTomato+ tumor organoids were isolated from ROSAmT/mG;MMTV-PyMT tumors and transplanted to the right flank of a nonfluorescent NSG mouse. Tumor organoids were isolated from β-actin-CFP;MMTV-PyMT tumors and transplanted to the left flank of the same mouse. After 6-8 wk, lungs of these mice were harvested and examined for multicolor metastases. There are two potential outcomes at the metastatic site. If metastases arise exclusively from a single seeding event, there should be only single-color metastases. In contrast, serial seeding by single cells should produce multicolored metastases. (B) Representative micrograph of transplanted tumors arising from either mTomato+ or CFP+ tumor organoids transplanted into NSG host mice (n = 22 tumors, 11 mice, 2 independent experiments). mTomato+ tumor cells were observed in 5 of 11 CFP+ tumors and accounted for 1–5% of the total tumor area. (C and C′) Representative micrographs of CFP+ tumor colonized by a large mTomato+ metastasis (C) and a small mTomato+ tumor cell cluster (C′). The tumor was stained with phalloidin (F-actin) and DAPI. (D) Representative micrographs of single colored CFP+ or mTomato+ lung metastases. Multicolored metastases were not observed (n = 0 of 75 metastases, 7 mice, 2 independent experiments). (E) Schema of tail vein assay that models serial waves of disseminated single tumor cells. 2 Å~ 105 FACS-sorted mTomato+ single cells were injected into nonfluorescent NSG host mice and 2 d later, 2 Å~ 105 FACSsorted CFP+ single cells were injected into the same mice. Three weeks later, lungs were collected and analyzed. Multicolored metastases were not observed (n = 0 of 64 metastases, 4 mice). (Scale bars, 1 mm in B, 500 µm in C, 1 mm in C′, and 50 µm in D.)

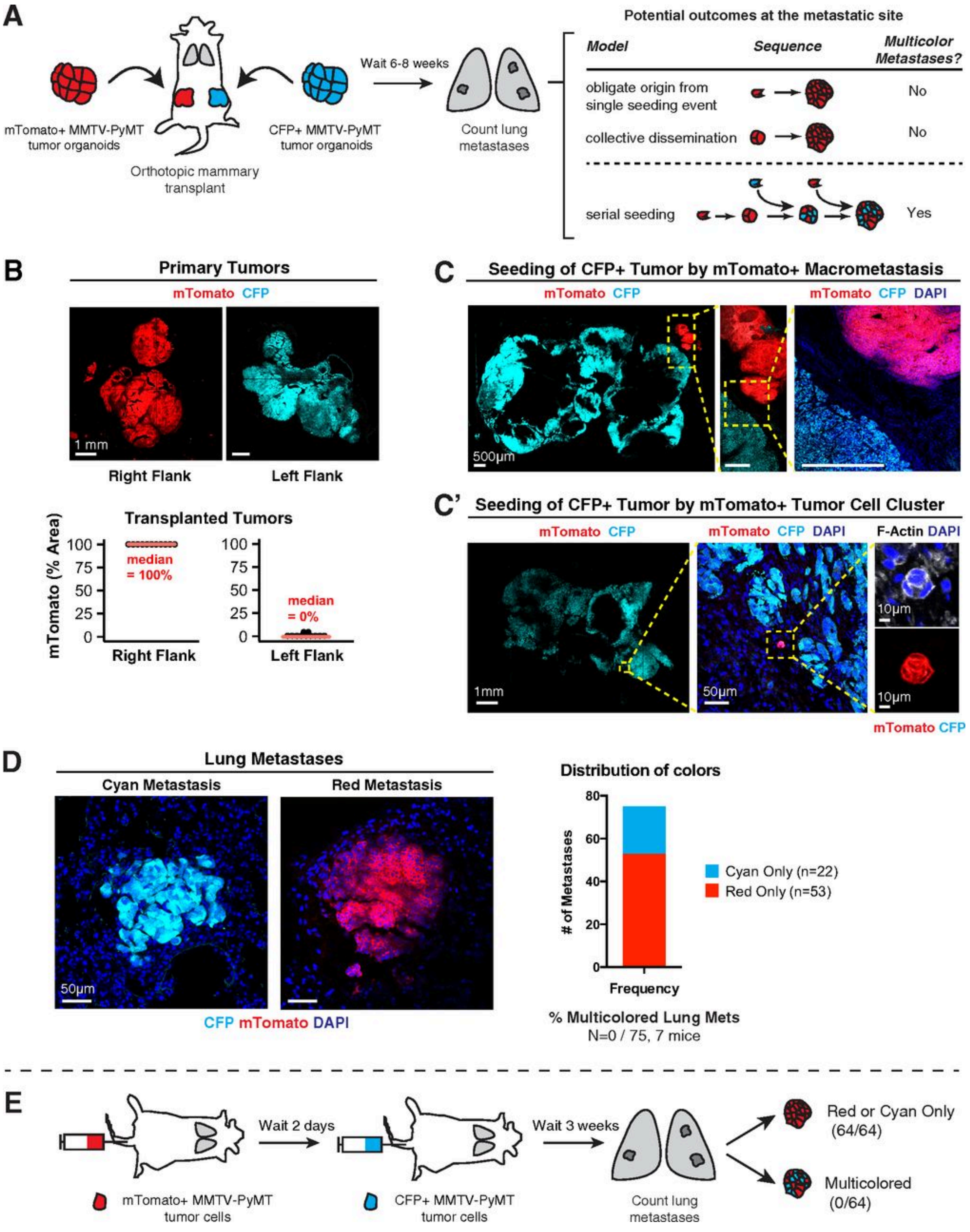

Supplemental Figure 3-3. Multicolored disseminated tumor emboli are observed. (A) Representative micrograph of a multicolored disseminated tumor cell cluster invading into an adjacent vessel. The transplanted tumor is composed of mTomato+ and CFP+ tumor cells. Injection with fluorescently labeled VE-Cadherin and CD31 antibodies marked functional vasculature. Tumors were also stained with DAPI to mark nuclei. Leftmost panel demonstrates a collective cluster (cc) of tumor cells invading into a nearby vessel lumen (L). Inset shows CFP+ blebs in close proximity to the vessel (n = 12 units, 6 tumors). (B) Representative micrographs of multicolored disseminated tumor cell cluster intercalated into adjacent blood vessel wall. A mosaic mTomato+, CFP+ tumor was stained with DAPI. The mouse was injected with fluorescent VE-Cadherin + CD31 antibodies before sacrifice. White hash marks: vessel lumen. Magenta harsh marks: cell cluster. (C) Representative micrographs demonstrating intercalation of disseminated tumor cell clusters into vessels of varying caliber. Mosaic MMTV-PyMT;mT/mG ;MMTVPyMT transplanted tumors were stained with phalloidin (F-actin) and DAPI. Yellow hash marks: vessel lumen. (D) Representative micrographs demonstrating intravascular dissemination units of different sizes in vessels adjacent to primary tumor. Mosaic MMTV-PyMT;mT/mG transplanted tumors were stained with phalloidin (F-actin) and DAPI. Yellow hash marks: vessel lumen. (Scale bars, 20 μm in A, B, and D, Left, and 10 μm in C.)

Supplemental Figure 3-3.

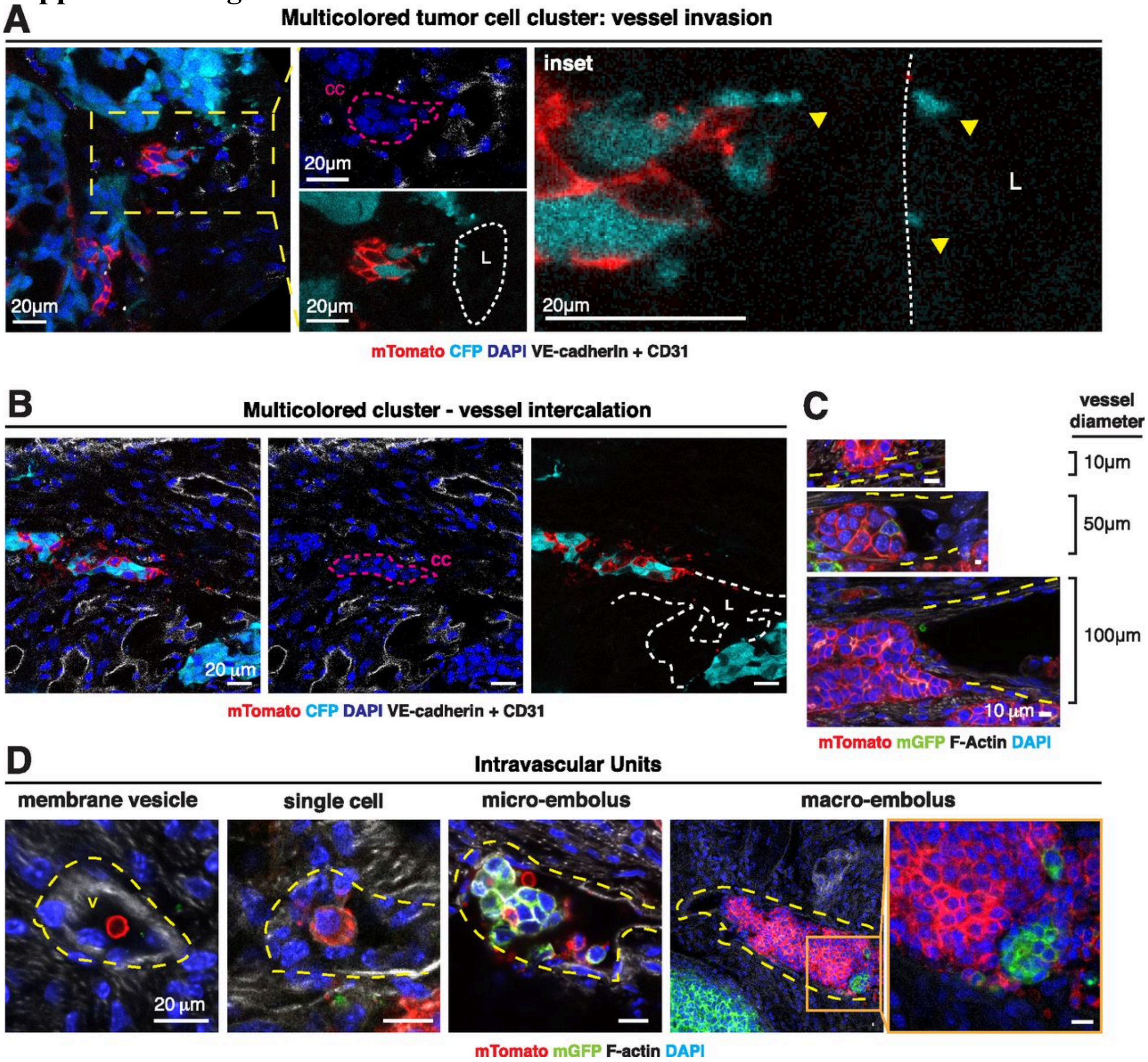

Supplemental Figure 3-4. Single tumor cells aggregate into tumor cell clusters in a nonadherent dish.

(A) Single tumor cells were isolated by FACS and either immediately plated into Matrigel or first incubated in a nonadherent dish for 24 h and then subsequently plated into Matrigel. The same numbers of cells were used in each condition. (B and B′) Single cells and clusters were counted and the percentage of events that were clusters was determined. (B) Twenty-four–hour incubation increases the percentage of cell clusters by >15-fold. n = 402 events, 5 independent experiments. P value determined by Wilcoxon rank sum test. $P < 0.05$. (B′) Cluster size distribution of aggregated clusters, median: 2 cells, range: 2–60 cells (n = 80 clusters, 4 independent experiments). (C and C′) Single red or green tumor cells were isolated by FACS and either immediately plated into Matrigel or first incubated in a nonadherent dish for 24 h and then subsequently plated into Matrigel. The same numbers of cells were used in each condition. (C) Clusters resulting at day 1 consisted of both red and green cells, confirming that they were generated by aggregation, rather than by clonal expansion of a single tumor cell. (Scale bar, 20 μm.) (C′) The percentage of multicolored clusters formed postincubation stratified by cluster size. The predicted distribution was determined from binomal expectation. R^2 was determined by Pearson correlation coefficient (n = 41 clusters, 2 independent experiments).

Supplemental Figure 3-4.

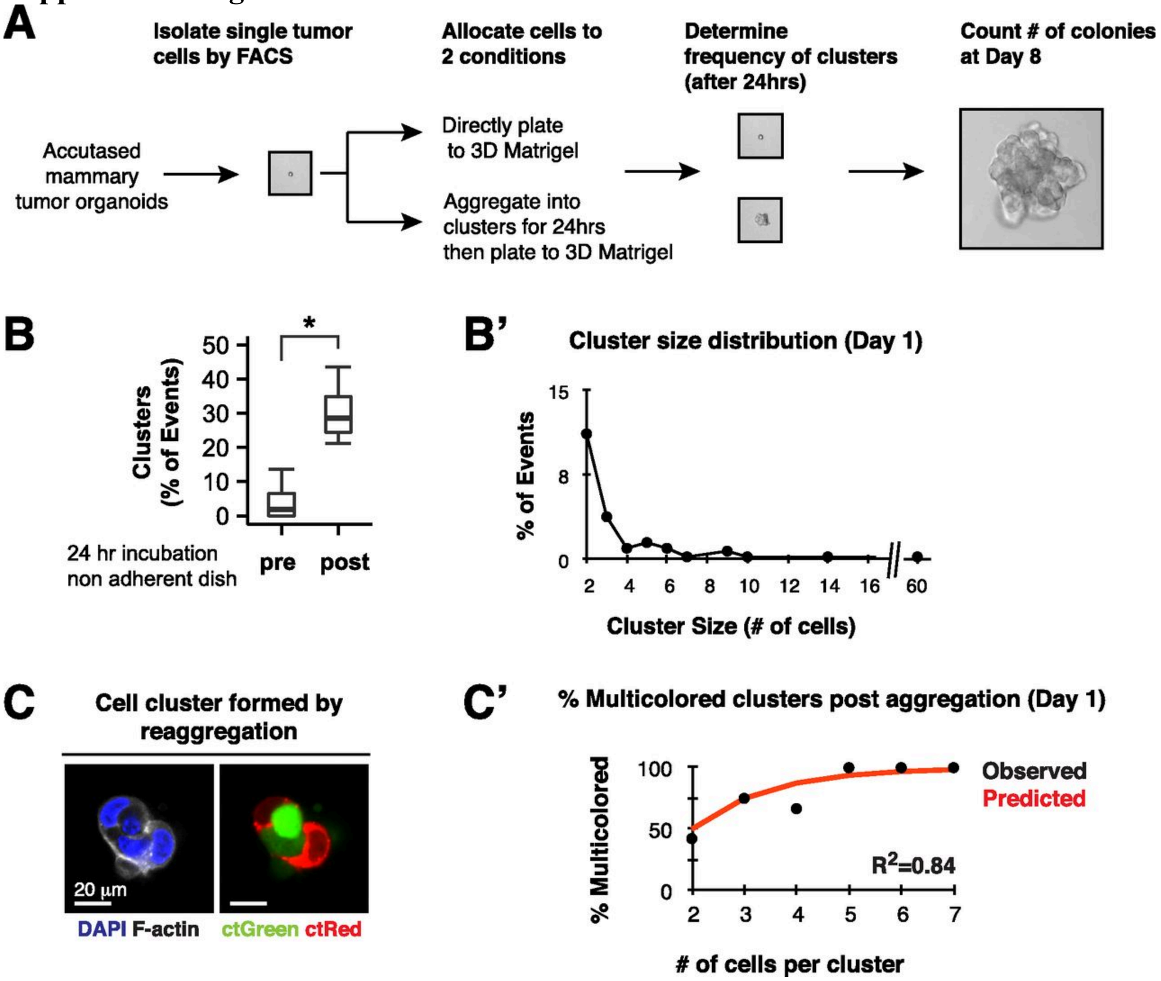

Supplemental Figure 3-5. Disseminated tumor cells are enriched for K14+ and FACS-sorted single K14+ and K14− tumor cells Interconvert to form uniformly K14+ clusters.

(A) Representative micrographs demonstrating K14+ polyclonal collective invasion, dissemination, and intravascular embolus (from left to right). Mosaic ROSAmT/mG;MMTV-PyMT transplanted tumors were stained with DAPI and K14. Yellow hash marks: vessel lumen. (B) The percentage of disseminated single tumor cells and disseminated tumor cell clusters that are K14+ presented as a bar-graph (n = 45 single cells, n = 17 clusters, across 5 tumors). P value determined by Fisher's exact test. (C) Single K14+ and K14− tumor cells were isolated by FACS from K14-actin-GFP;MMTV-PyMT tumors, and then subsequently stained for K14, phalloidin (F-Actin), and DAPI. (Right) The median intensity of K14 staining for each cell presented as a boxplot (n = 317 cells, 3 independent experiments). P value determined by Mann–Whitney test. (D, Left) Cell clusters formed at day 1 postaggregation were stained for K14, DAPI, and phalloidin (F-actin). (Right) Bar graph shows the percentage of clusters composed of only K14− cells, only K14+ cells, or both cell types (n = 119 clusters, 3 independent experiments). (E, Left) Colonies formed at day 8 were stained for K14 and phalloidin (F-actin). (Right) Bar graph shows the percentage of colonies composed of only K14− cells, only K14+ cells, or both cell types (>10 cells per colony, n = 55 colonies, 3 independent experiments). (Scale bars, 10 µm in A, Center, C, and D; 20 µm in A, Left and Right, and E.)

Supplemental Figure 3-5.

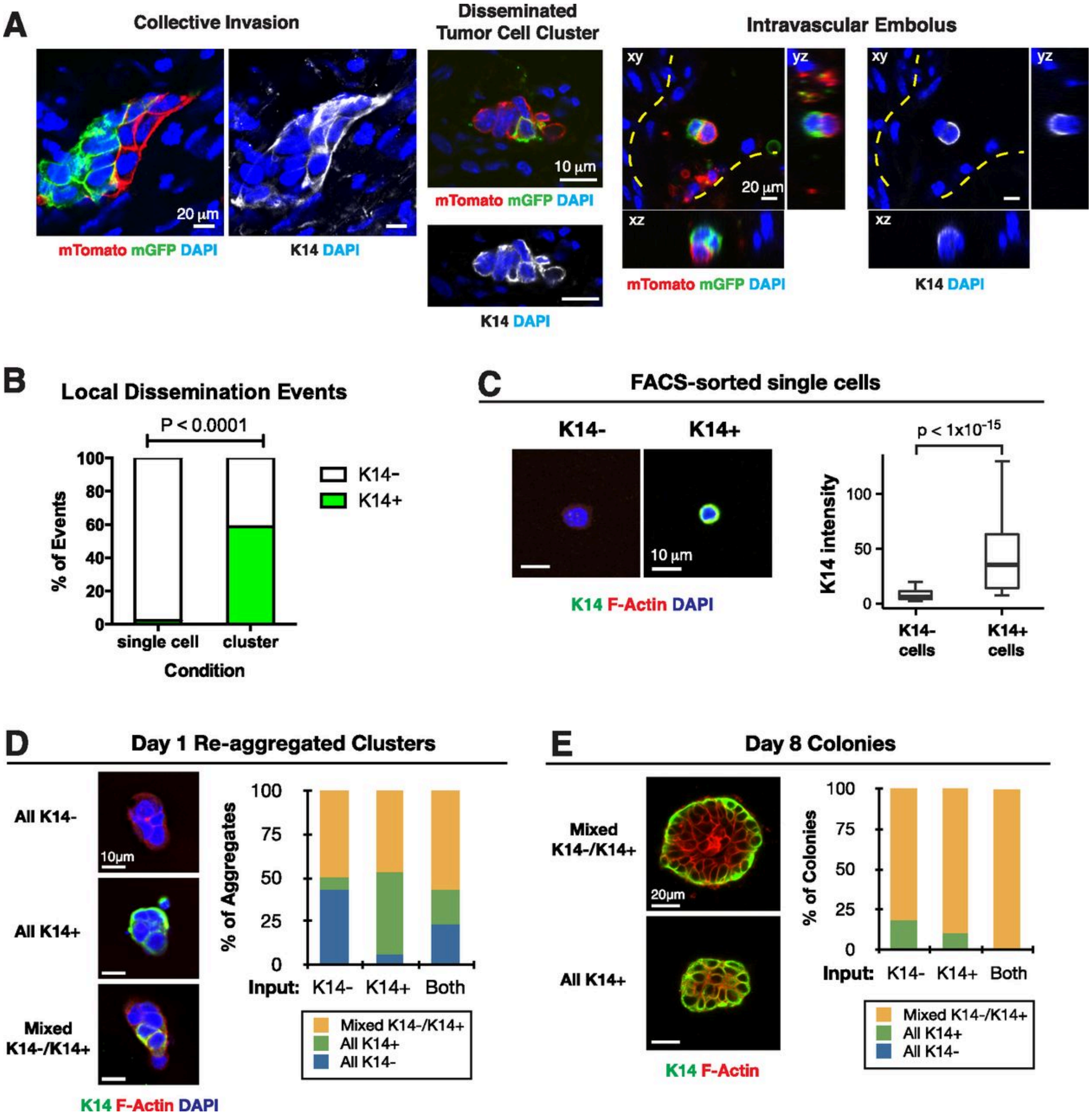

Supplemental Figure 3-6. K14+ cells and K14− cells are enriched for different stemness genes and are not significantly different in their mammosphere forming ability.

(A) Relative expression of different stem cell-associated genes presented as a dot-plot. P-value determined by Mann–Whitney test. (B) Enrichment in K14+ and K14− cells was determined by Wilcoxon gene set testing using published stem cell gene sets identified by transcriptome profiling of mouse mammary gland. (C) Representative micrographs of mammospheres generated from K14− and K14+ single cells in suspension culture. (Scale bars, 100 μm.) (D) The median number of mammospheres is presented as a dot plot for K14− and K14+ single tumor cells isolated by FACS and plated at two different densities. P value determined by the Mann–Whitney test.

Supplemental Figure 3-6.

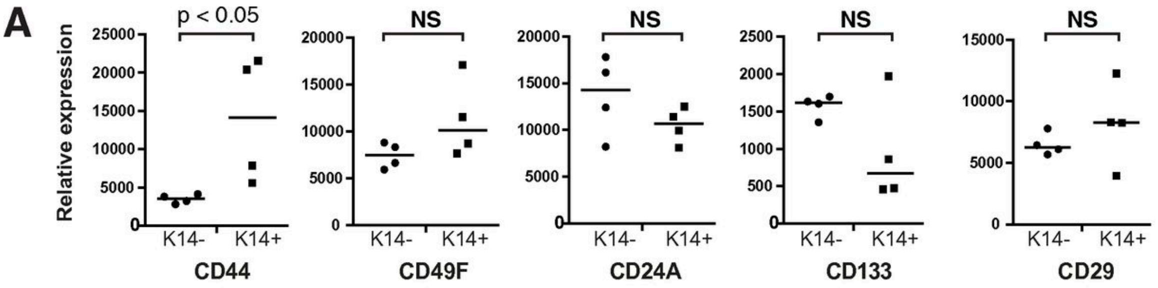

B

Source	Geneset	Size of Gene List	P-values	
			ENRICHED in K14- cells	ENRICHED in K14+ cells
Spike et al. Cell 2012	Myoepithelial cells	856	1.0E+00	2.1E-78
Spike et al. Cell 2012	fetal mammary stem cells	869	6.3E-03	9.9E-01
Spike et al. Cell 2012	adult mammary stem cells	1388	9.9E-01	1.1E-02
Soady et al. Breast Cancer Research 2015	Mammary stem cells	323	1.0E+00	4.6E-15
Kendrick et al. BMC Genomics 2008	Myoepithelial	861	1.0E+00	1.8E-78
Kendrick et al. BMC Genomics 2008	Luminal ER neg	326	3.5E-08	1.0E+00
Kendrick et al. BMC Genomics 2008	Luminal ER pos	488	3.1E-04	1.0E+00

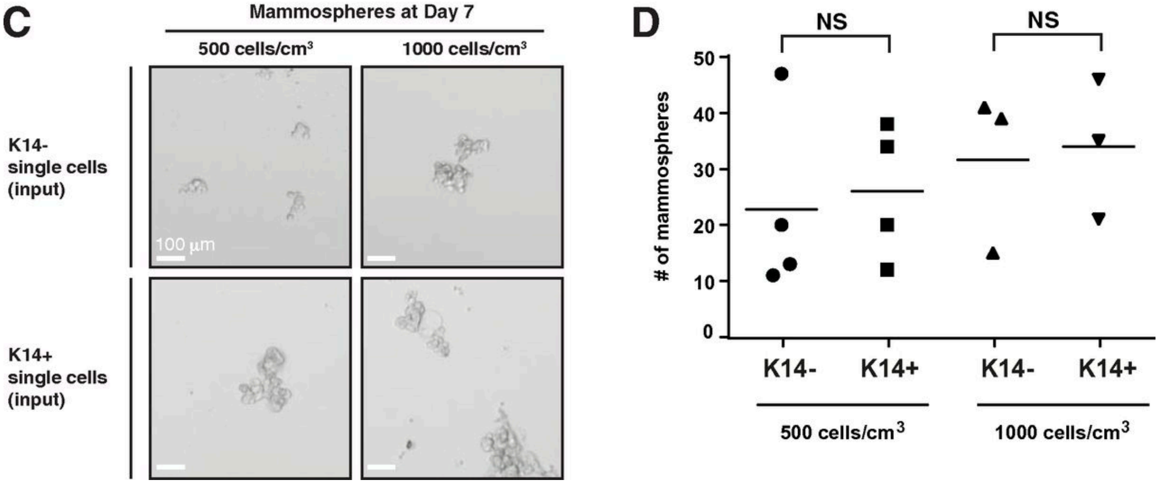

Supplemental Figure 3-7. Gene network of K14+ metastasis genes. The network of coregulated genes seeded using the most differentially expressed genes in Fig. 6E. Seed genes in black, neighbor genes in gray. Physical interactions, genetic interactions, and common pathway interactions were included in the network.

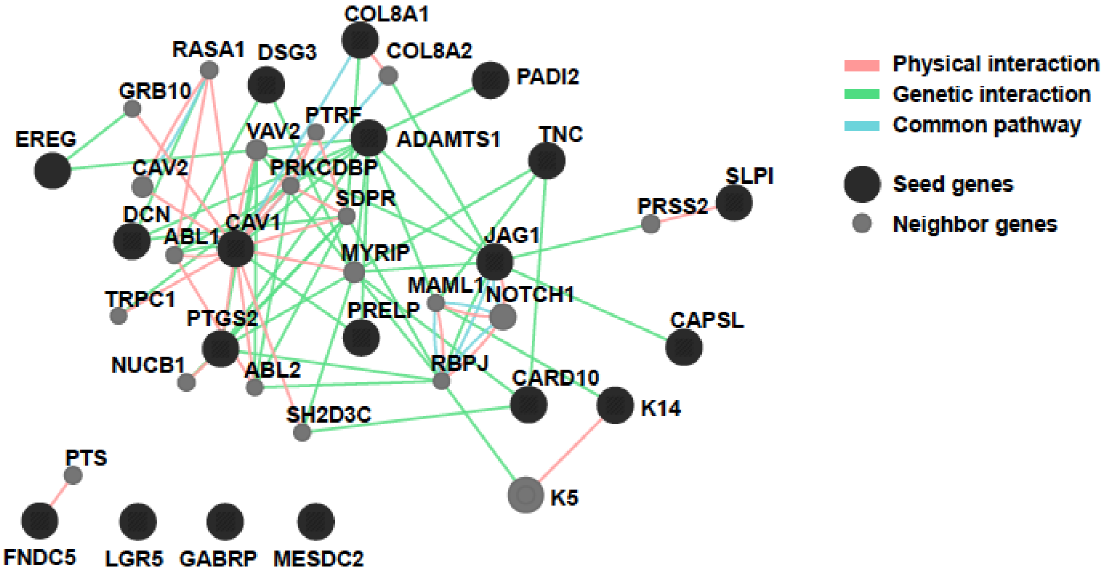

Supplemental Figure 3-8. Polyclonal metastasis occurs through collective dissemination of K14+ tumor cell clusters. Primary tumors invade and disseminate collectively into surrounding tissue. This disseminated unit efficiently colonizes distant sites to form polyclonal metastasis. In MMTV-PyMT tumors, the traveling unit is composed of multiple K14+ epithelial tumor cells. Our model is supported by multiple lines of experiments in our study: the high frequency of multicolored metastases arising from well mixed multicolored primary tumors in which clonality can most readily be assessed (Fig. 1 and Fig. S1), the lack of multicolored metastases when the different colored cells are deployed at different locations or at different times (Fig. S2), the observation of polyclonal clusters across major stages of metastasis (Fig. 2), the large survival advantage conferred by multicellular organization both in culture and in vivo (Fig. 3), the enrichment for K14 expression in disseminated tumor cells and micrometastases (Fig. 4), the expression of epithelial desmosome and hemidesmosome gene programs in K14+ cells (Fig. 5), and the requirement for K14 expression for both distant metastasis and the expression of multiple metastasis effectors, crucial for remodeling of the metastatic niche, including Tnc, Adamts1, Jag1, and Ereg (Fig. 6).

Supplemental Figure 3-8.

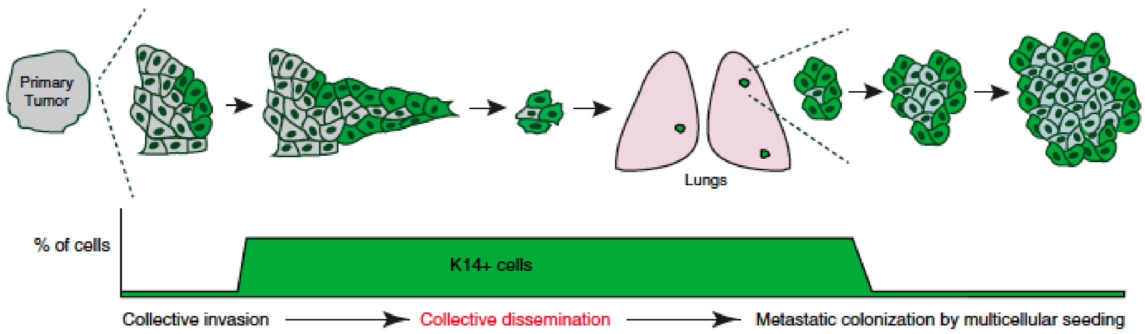

CHAPTER 4

An engineered 3D vessel model reveals the dynamics of mosaic vessel formation

Abstract

In a solid tumor, vascular structure and function varies from the core to the periphery and this heterogeneity can influence the mechanisms employed by tumor cells to enter circulation. In the core, blood vessels can have defects in endothelial coverage, leaving cancer cells directly exposed to flow and potentially promoting intravasation. Consistent with prior reports, we observed that approximately 6% of vessels in a mouse model of breast cancer exhibited a mosaic morphology *in vivo*. The mechanisms by which mosaic vessels form remain incompletely understood, in part because of the challenges associated with observing tumor-vessel interactions deep within tumors in real-time. To overcome this challenge, we developed a tissue engineered tumor model which contains a physiologically and morphologically realistic microvessel in co-culture with mammary tumor organoids. This approach allows real-time and quantitative assessment of tumor-vessel interactions under conditions that recapitulate many *in vivo* features. We observed mosaic vessel formation in real-time and found that it was the most frequent type of tumor-vessel interaction *in vitro* compared to vessel constriction and vessel pull. Moreover, our model reveals that tumor cells invade the vessel wall by integrating with the endothelial cell lining, suggesting the formation of a tumor-endothelial cell junction. Furthermore, we observed in real-time an intravasation event that followed the formation of a mosaic vessel. Our assay enables future studies that could reveal mechanisms to target mosaic vessel formation and intravasation and limit metastatic recurrence.

Introduction

Metastasis is responsible for approximately 90% of cancer patient mortality (1, 2). Cancer progression is a highly dynamic multi-step process, by which cancer cells escape the primary tumor, intravasate, circulate, seed distant sites, and form secondary tumors. The initial steps in cancer metastasis involve the invasion of tumors cells into the surrounding stroma and intravasation into the vasculature. Single circulating tumor cells (CTCs) and circulating tumor microemboli (CTM) have been detected in circulation in mouse models as well as cancer patients (3, 4). Furthermore, though rare, CTM have been shown to have a higher metastatic potential compared to single tumor cells (5, 6). However, the mechanisms of tumor-vessel interactions that enable tumor cell entry into circulation are poorly understood (7).

Intravasation is an early step in the metastatic cascade and is accomplished when cancer cells gain access to circulation (8, 9). Intravital imaging within primary tumors has offered insights into intravasation by revealing single cancer cells migrating into vessels, in a process termed transendothelial migration (TEM, 10). However, as solid tumors grow, they expand beyond the capacity of pre-existing vessels and develop their own vascular supply (10-12). These newly formed vessels are diverse in their structure and permeability ("leakiness"), and vary from the tumor core to its periphery (12-14). These changes could enable alternate mechanisms or rates of intravasation. The recent emphasis on collective dissemination and metastasis of CTMs (5, 6, 15, 16), has raised new questions about how groups of adherent cells could access the circulation.

Most of our understanding of tumor-vessel structure and function has been derived from static images of fixed tissues. Structural studies have revealed tumor vessels with defective organization and loosely connected endothelial cells (17). Immunohistological sections of varying primary tumor xenografts from different mice and human tumor cell lines have revealed that tumor vasculature exhibits intercellular openings up to 4.7 μm in size allowing the local extravasation of both drug delivery systems and red blood cells, a phenomenon known as the enhanced permeation and retention (EPR) effect (17, 18). In addition to intercellular gaps, tumor vasculature in colon carcinoma xenografts has been shown to exhibit a hybrid structure, with both tumor cells and endothelial cells contributing to the vessel wall (termed "mosaic vessels") (19, 20). This loss of endothelial coverage presents a mechanism by which tumor cells could access the circulation without the need for TEM (19).

Despite these intriguing observations very little is known about the dynamics of tumor-vessel interactions and their effect on intravasation. To approach this problem, we developed a 3D tissue-engineered model of the tumor microenvironment in which we co-cultured primary tumor organoids with functional microvessels and visualized the cellular interactions in real time (21). This microfluidic approach enabled us to observe three different types of tumor-vessel interactions: mosaic vessels, vessel constriction, and vessel pull. We found that mosaic vessels formed rapidly and were the most frequent type of interactions observed *in vitro*. Moreover, we observed mosaic vessel formation in real-time leading to collective intravasation of CTMs. Although rare, we observed vascular constriction due to engulfment by a growing organoid that can contribute to the formation of vascular defects such as dead-ends. In addition, we observed organoids “pulling” on microvessels, termed vessel pull, which could be a mechanism for vessel co-option by highly adherent tumor cells. We found an increase in endothelial cell proliferation and cell death in the presence of tumor organoids within the microvessels which can influence the type of tumor-vessel interaction that will be formed, and, consequently, the mechanism by which CTCs and/or CTMs enter circulation.

Results

Primary tumors are exposed to the lumen of vessels partially lined with endothelial cells *in vivo*

To establish the prevalence of mosaic vessels, we first sought to characterize their frequency in a commonly used and highly metastatic mouse model of breast cancer, in which the MMTV LTR is used to drive the polyoma virus middle T oncogene (22). We crossed this cancer model with a fluorescent reporter mouse in which all cells are labeled with a membrane localized red fluorescence protein (mTomato) (23). To unambiguously identify tumor tissue in contact with the lumen of mosaic blood vessels, we performed orthotopic transplants of $ROSA^{mTmG}$*; MMTV-PyMT* tumor organoids into non-fluorescent NSG host mice. We assayed for mosaic vessels by staining for platelet-endothelial cell adhesion molecule (PECAM-1/CD31, green) with immunofluorescence, and scanned the entire sections (16 μm total tissue depth) in 1 μm steps. Microvessels were considered for analysis if they intersected the tissue section with an approximately circular cross-section (i.e. orthogonal to the tissue section). We defined potential mosaic vessels by the presence of tumor cells in apparent contact with the vessel lumen in 2D, as indicated by the absence of CD31 staining (Fig 1AB). We then confirmed the mosaic vessel structure in 3D optical reconstructions (Fig. 1 DE). This method ensured that we did not miss-classify vessels due to variations in staining or loss of cell fragments during preparation of the tissue sections. We also assessed the completeness of the endothelial lining based on differences in nuclei morphology (DAPI staining, blue) between tumors and endothelial cells. Tumor nuclei appeared more rounded compared to the elongated shape of endothelial nuclei. Based on these criteria, mosaic vessels could be readily distinguished from intact vessels in these 3D volumes (Fig 1B' vs. C'). In total, we examined 2681 vessels in 20 whole tissue sections from three tumors derived from independent transplant mice and identified 168 mosaic vessels (6.3%). The average luminal vessel diameter was 103 ± 50 μm. While we did not have sufficient sections for quantitative analysis of the spatial distribution, we observed that mosaic vessels were generally located close to the core of the tumor with none at the periphery.

A perfusable 3D tissue-engineered microvessel platform for examining mosaic vessel formation

We next sought to understand the cellular dynamics underlying mosaic vessel formation. To accomplish this goal, we developed a tissue engineered model for real-time imaging of tumor-vessel interactions (21, 26). The goal was to build a functional microvessel surrounded by tumor organoids from the *ROSA*^{mTmG}*; MMTV-PyMT* model (Fig. 2A). The microvessel platform consists of a cylindrical channel lined with a confluent monolayer of endothelial cells. Initially, the tumor organoids were embedded in a collagen type I matrix within a PDMS housing surrounding a central metal rod which provides a template for the vessel (Fig. 2B). The rod was then removed leaving behind a cylindrical channel that was seeded with endothelial cells, which were allowed to settle and adhere to the channel walls to form an intact vessel (Fig 2B). The vessel was then perfused with endothelial cell medium at a physiologically relevant shear stress and a steady laminar flow. The microvessels were generated using GFP expressing human umbilical vein endothelial cells (HUVEC-GFP).

For direct visualization of tumor-vessel interactions, we typically imaged at the mid plane of the vessel (Fig. 2C). Immunofluorescent staining for β-catenin revealed a complete lining of endothelial cells, arranged in a cylindrical geometry and with extensive intercellular adhesions (Fig. 2D). The tissue-engineered microvessels contained a single intact lumen, as demonstrated by the mid-plane and cross-section images (Fig. 2D). Barrier function was verified by measurement of the permeability of fluorescent probes introduced into the lumen. Tumor organoids were cultured in close proximity to the microvessel (Fig. 2E, F) and exhibited a 3-fold increase in area over three days of culture with constant vessel perfusion, consistent with survival and extensive proliferation (Supplemental Fig. 1H, I). Co-cultures require that media conditions are acceptable to all cell types. Accordingly, we compared the growth of organoids isolated from the same mouse in three different media conditions: "organoid medium" supplemented with FGF2 (16, 25), HUVEC medium, and HUVEC medium supplemented with dibutyryl-cAMP (db-cAMP; Supplemental Fig. 1A-G). We used cAMP as a means to verify vessel integrity and function (30, 31). Tumor organoid growth and circularity were determined by measuring the projected surface area at day 0 and day 5 in the microvessel model. We observed a significant increase in growth and circularity of tumor organoids compared to control in all media conditions (Supplemental Fig. 1F-G). In addition, organoids in HUVEC media exhibited a more cystic morphology than in organoid media (Supplemental Fig. 1B-G).

Co-culture with tumor organoids increases vessel permeability and induces transient focal leaks

We first sought to determine the functional properties of the tissue-engineered microvessels in the presence and absence of tumor organoids. Endothelium integrity and barrier function were determined by measuring permeability (P_{3D}, cm s^{-1}), which describes the rate of transport of a solute from the vessel lumen across the endothelium and into the surrounding ECM (26, 29). We measured vessel permeability by simultaneously perfusing three different fluorescent molecular weight probes through the vessel lumen: 3 kDa dextran (Alexa Flour-488-conjugated), 10 kDa dextran (Alexa Flour-647-conjugated) and 70 kDa dextran (Texas Red). Using three different size probes enabled assessment of the size of defects in the endothelium. From time-lapse fluorescence microscopy we identified the time prior to the arrival of the fluorescent probe (designated 0 min; Fig 3A-D), luminal filling (typically 20 min, Fig 3A'-D'), and the kinetics with which the fluorescence probes perfused out of the vessel and into the ECM (Fig 3A''-D''). For all three molecular weight dextrans, co-culture with tumor organoids increased vessel permeability by about 10-fold to $3 – 6 \times 10^{-5}$ cm s^{-1} (Fig. 3E, Supplemental Fig. 3E, C). There was not statistical difference between the permeabilities for 3 kDa, 10 kDa, and 70 kDa dextrans showing that the defects in the endothelium were sufficiently large to allow extravasation of relatively large molecules: the diameter of 70 kDa dextran is approximately 12 nm (32). In contrast, treatment with 400 µM dibutyryl-cAMP (db-cAMP) decreased permeability in both control and tumor co-culture microvessels (Fig. 3B-B'', D-D'', E, Supplemental Fig. 2). We also found that luminal filling is delayed in vessels treated with db-cAMP suggesting a tighter barrier function.

Our dynamic imaging of vessel permeability also revealed transient focal leaks of labeled dextrans (Fig. 3F-H). To unambiguously identify regions of excess fluorescence intensity along the length of the microvessels, we used the 10 kDa dextran (Alexa Flour-647-conjugated) probe. We observed a higher number of focal leaks in co-cultures with tumor organoids and, conversely, a reduced number of focal leaks in both control and tumor co-culture microvessels following treatment with db-cAMP (Fig. 3G). In addition to the increase in vessel permeability in the presence of tumor organoids, we found a positive correlation with the increase in number of focal leaks (Fig. 3H). Consistent with our results, transient focal leaks have been detected in the tumor vasculature of mouse brains and mammary glands (33-35) and cAMP agonists have previously been shown to suppress focal leaks and decrease the macromolecular permeability coefficients (30, 31).

Tumor organoids actively replace the endothelial lining to form mosaic vessels

Having established that our tissue-engineered microvessels were functional and that their permeability was regulated by co-culture with tumor organoids, we next sought to analyze the cellular basis of tumor-vessel interactions in real time. To accomplish this goal, we co-cultured *ROSA*^{mTmG}*; MMTV-PyMT* organoids within the ECM of our microvessel model. We used wide-field fluorescence microscopy, focused on the mid plane of the vessel, to follow cell behaviors (Fig. 1C). We observed three different types of tumor-vessel interactions: (1) cancer cells integrating with the endothelial lining to form mosaic vessels (Fig. 4A-A'), (2) cancer cells wrapping around the vessel and constricting the lumen (Fig. 4B-B'), or (3) cancer cells pulling on the microvessel and displacing its position (Fig. 4C-C'). The geometry of each type of tumor-vessel interaction was confirmed in cross-section (Fig. 4A'-C').

For quantification purposes, we identified mosaic vessels using two criteria: (i) clear visible retention of fluorescent dye at the site of tumor-vessel contact, and (ii) no interruption of flow following tumor-vessel interactions. In contrast, vessel constriction resulted in diminished or abolished downstream flow. Quantification of 19 devices revealed that mosaic vessel formation was the most frequent type of tumor-vessel interaction (Fig. 4G). We next tested the functional status of the mosaic vessels from measurements of solute permeability. We observed dye retention in the lumens of the vessels at the sites of tumor-endothelial cell contact, revealing that the cancer cells contributed to barrier function (Fig. 4D-F, D'-F').

Mosaic vessels as a route for intravasation of tumor cells

The presence of tumor cells in the vessel lining exposes them directly to flow and represents a potential mechanism for intravasation. Once mosaic vessels are formed, individual CTCs or CTMs can be released into circulation. We next assayed for intravasation in mosaic regions along the microvessel. As above, we visualized tumor-vessel interactions using wide-field fluorescence microscopy focused at the mid-plane of the microvessel (Fig. 5A-B). We observed an organoid approaching a microvessel, making contact with and incorporating into the endothelium, then releasing a tumor microemboli into circulation (Fig. 5A'-B'). The tumor microemboli appears to roll on the luminal side of the endothelium as it moved in the direction of flow (Fig. 5A'-B').

A perfusable 3D microvessel platform for modeling mosaic vessel formation

We next sought to design a microvessel platform that would enable reproducible placement of tumor cells relative to the engineered microvessel. In our previous model, tumor organoids were seeded randomly throughout the collagen matrix and the likelihood of interacting with the vessel was dependent on the initial location of the organoids. To fix the distance between the tumor organoid and the microvessel, we introduced a modification in the microfluidic platform. A second cylindrical template channel was introduced within the PDMS housing parallel to the first microvessel channel (Fig. 6A-B). Once the two template rods were placed into the PDMS housing, the collagen solution was introduced and allowed to gel. We first introduced the tumor organoids into one of the channels by slowly removing one rod leaving the other in place. The second cylindrical rod was then removed following the steps previously described for vessel formation. Using wide-field fluorescence microscopy focused at the mid-plane of the microvessel (Fig. 6C), we observed tumor invasive strands initiate and grow in the direction of the vessel incorporating into the endothelial lining (Fig. 6D-E).

Endothelial proliferation and cell death in response to tumor organoids

To analyze the influence of tumor organoids on the endothelium, we quantified endothelial cell proliferation and cell death. We measured the frequency of cell proliferation and cell death within the microvessels using time-lapse phase-contrast microscopy imaging focused at the vessel poles (i.e., top and bottom) (Supplemental Fig. 3A). Endothelial cell divisions were visualized by the increase in cell’s light refraction and cell rounding followed by the integration of the two daughter cells back into the endothelium (Supplemental Fig. 3B). The proliferation rate was calculated as the percentage of endothelial cells dividing per hour (%/h). We found that tumor organoids increased endothelial cell proliferation by approximately 2-fold compared to control. In contrast, treatment with 400 μM db-cAMP decreased endothelial cell proliferation in both control and tumor co-culture microvessels (Supplemental Fig. 3C). Similarly, cell death was observed by the pronounced cell contraction and removal from the endothelium in the direction of flow (Supplemental Fig. 3D). We found that tumor organoids increased cell death by 4-fold compared to control and decreased upon treatment with db-cAMP (Supplemental Fig. 3E). Based on these results, we found that the net change in the number of endothelial cells was -1.3 %/h in the presence of tumor organoids. In particular, the negative sign in the net change demonstrates that endothelial turnover is dominated by cell death in the presence of tumor organoids.

Discussion

The goal of this work was to study the cellular dynamics of tumor-vessel interactions using a 3D microvessel model of the tumor microenvironment combined with 3D organotypic culture of a highly metastatic breast cancer model. While the initial steps in the metastatic cascade involve interactions of cancer cells with blood vessels, little is known about the dynamics of this process. Prior studies have reported a vast heterogeneity in tumor vessel architecture ranging from intact endothelium to complex network structures (19, 36). Furthermore, tumor-vessel heterogeneity has been shown to vary from the periphery to the tumor core. Typically, tumor vessels are found to be intact in the periphery, however, the tumor core presents a range of vascular abnormalities including loops, dead-ends, partial (i.e., mosaic vessels), or an absence of endothelial cell lining (i.e., vasculogenic mimicry), among other defects (13, 37). The range of these defects can dictate the mode and frequency of CTCs and CTMs entering circulation. Irregularities in endothelial cell coverage have been suggested to have important implications in intravasation. Studies of fixed tissue sections have shown the presence of tumor cells within the vessel wall in many cancer types; however, the dynamics of this process has not been studied. This challenging task has been hindered due to the difficulties in establishing tumor models in which tumor-vessel interactions can be visualized and characterized.

To study the cellular dynamics of tumor-vessel interactions used a 3D tumor-microvessel model that incorporates a functional vasculature within an extracellular matrix material. This reductive model combines a perfusable microvessel with freshly isolated mammary gland tumor organoids embedded in the surrounding matrix (21). In this way, we recapitulated both the microvessel cylindrical geometry, endothelium-matrix interactions, and shear stress and flow, along with the 3D structure of tumors (Fig. 2) (25). This approach enables visualization of tumor-vessel interactions in real time, recapitulating many aspects of the spatial organization and structure of the *in vivo* microenvironment.

From extensive imaging, we observed three types of tumor-vessel interactions: mosaic vessels, vessel constrictions, and vessel pull (Fig. 4 and Fig. 7B). We found that mosaic vessels were the most frequent type of tumor-vessel interactions observed *in vitro*. Interestingly, in patient biopsy samples from varying malignancies, such as glioblastoma, melanoma, gastric cancers and sarcomas, the partial or complete absence of endothelial cell lining has been associated with distant metastasis and poor patient survival (38-40). The presence of tumor cells in vessel walls has been suggested as a mechanism for bulk and high rate intravasation events since it gives tumor cells greater access to systemic circulation. However, the mechanisms of formation of vascular defects and subsequent intravasation remain poorly understood. Using our tumor organoid-microvessel platform, we show for the first time the formation of mosaic vessels in real time (Fig. 4).

Following mosaic vessel formation, we observed the detachment of CTMs that rolled on the luminal side of the endothelium in the direction of the vessel flow. Previous animal and clinical studies have shown that CTCs and CTMs can be shed into the circulation during tumor resection and, consequently, soft tumor manipulation decreased the risk of metastatic lesions (41-44). Recent studies in mice have demonstrated that CTMs, as opposed to CTCs, have increase survival and higher metastatic potential (5, 6, 15, 16).

CTMs are thought to originate from clusters of polyclonal cells arising directly from the primary tumor and not by aggregation of CTCs in circulation (5, 6), however, the mechanisms by which CTMs gain access to the systemic circulation remain unknown. Using our tumor-microvessel model, we show a mechanism for CTM intravasation at mosaic vessels that bypasses the need for TEM.

Additionally, the size of the CTMs entering circulation has been suggested to be regulated by vessel diameter (45). Our results show a CTM of 50 μm in diameter that detached from a microvessel of approximately 150 μm in diameter. Moreover, our *in vivo* analysis showed an average mosaic vessel diameter of approximately 100 μm. Our results are in line with observations in brain tumors where vascular invasion was more prevalent in vessels >200 μm in diameter which correlated with increased risk of metastasis and poor patient survival (45).

In addition to mosaic vessel formation, we observed, vascular constriction and vessel pull. Previous work has shown that tumors induce a mechanical stress on nearby vessels due to an uncontrolled growth within a confined space (46, 47). Here, we suggest vascular constriction as a mechanism for the formation of vascular defects such us dead-ends. Furthermore, vascular constriction can generate hypoxic regions that may increase the imbalance in pro- and anti- angiogenic signals further increasing tumor vascularization. We also observed tumors pulling on the vessel wall which may indicate sites of vessel co-option (i.e., the use of pre-existing vessels) by adherent tumor cells (21). For example, brain metastatic lesions from human melanoma cell lines have been shown to use vessel co-option as a mechanism to obtain nutrients without the need of an angiogenic switch which has high implications on anti-angiogenic therapies (48). This type of tumor-vessel interaction has been confirmed in fixed tissue section of brain biopsies from cancer patients (48).

Our tumor-microvessel model recapitulates many aspects of the intratumoral vasculature which lacks many of the features of healthy vasculature, such as smooth muscle cells and pericyte coverage, and poor lymphatic drainage. Tumor vasculature is leakier than normal vasculature, termed the enhanced permeation and retention (EPR) effect. This effect is widely exploited in systemic delivery of therapeutic agents to solid tumors. Here we show an approximately 10-fold increase in permeability of 3, 10 and 70 kDa dextrans in organoid-containing microvessel models, recapitulating the increase in leakiness associated with the EPR effect (49). In addition, the measured permeabilities of the three dextrans are not statistically different, as expected for paracellular transport at vascular defects (18, 50). In xenograft mouse models, the EPR effect results in extravasation of large particles into the tumor (51). The cutoff size is typically between 0.2 - 1 μm in diameter, depending on the tumor type. 70 kDa dextran, the largest solute used here (12 nm diameter), is within this cut-off range (32).

Until now, tumor-vessel interactions have been mostly studied using fixed tissue sections. Here we showed the dynamics of tumor-vessel interactions using a 3D microvessel model along with 3D organotypic culture of primary breast cancer tissue. We were able to model three types of interactions: mosaic vessel, vessel constriction and vessel pull, each of which may have important implications for cancer metastasis (Fig. 7A-B). Tumors that generate sufficient force on the endothelium to disrupt cell-cell junctions can enable the formation of mosaic vessel structures facilitating shedding of CTCs and/or CTMs exposed to the vessel flow and shear forces, without the need of TEM. While vessel constriction may give rise to other vascular defects such as dead-ends, vessel pull could be a mechanism used by highly adherent tumor cells to co-opt pre-existing vessels. Additionally, the state of the endothelium may contribute to the formation of any of these tumor-vessel structures. For example, if the endothelium had a net increase in cell death rate, it could facilitate the integration of tumors within the vasculature. On the other hand, if the rate of proliferation was higher and the overall state of the vessel was intact, tumors could interact with the endothelium by constricting or pulling on the vessel wall. Our experimental approach enables a convenient way to study multiple steps in the metastatic cascade that are otherwise very difficult to observe *in vivo*. Moreover, this tumor-microvessel model could also be adapted and customized to reflect other aspects of the tumor microenvironment to further study the metastatic process.

Materials and methods

Mice and cell lines

Mice used in this study were backcrossed onto and maintained on the FVB/n background in a specific pathogen-free facility. FVB/N-Tg(MMTV-PyVT)634Mul/J (MMTV-PyMT) mice and NOD.Cg-Prkdcscid Il2rgtm1Wjl/SzJ (NSG) mouse lines were acquired from the Jackson Laboratory (22). Mouse husbandry and procedures were all conducted according to an animal protocol approved by the Johns Hopkins University School of Medicine Institutional Animal Care and Use Committee. For confocal time-lapse experiments, MMTV-PyMT mice were crossed with *FVB/NJ*, *mT/mG* mice (23).

VeraVec HUVEC-TURBO-GFP (HUVEC-GFP) (HVERA-UMB-202100; Angiocrine Bioscience, New York, NY) were seeded in the cylindrical channel of the microvessel platform (24). Endothelial cells were grown in “normal growth medium” (NGM): MCDB 131 (Caisson Labs, Carlsbad, CA) supplemented with 10% heat inactivated fetal bovine serum (F0926; Sigma), 25 mg/mL endothelial mitogen (BT-203, Biomedical Technologies), 2 U/mL heparin (Sigma), 1 μg/mL hydrocortisone, 0.2 mM ascorbic acid 2-phosphate (Sigma), and 1% penicillin-streptomycin-glutamine (Life Tech). All culture conditions were in humidified environments with 5% CO_2 at 37°C. All cell lines were authenticated by their respective manufacturers and tested negative for mycoplasm.

Isolation of primary mammary tumor organoids

Primary tumor organoids were isolated from mammary tumors by a combined mechanical and enzymatic digestion using collagenase (C2139; Sigma-Aldrich) and trypsin (27250-018; Gibco Life Technologies) as previously described (16, 25). In brief, tumors were harvested from 8- to 10-wk-old mice, minced with a scalpel, and digested for 1 h at 37°C in collagenase solution: DMEM (10565-018; Gibco Life Technologies) with 2 mg/mL collagenase, 2 mg/mL trypsin (27250-018; Gibco LifeTechnologies), 5 %(vol/vol) FBS (F0926; Sigma-Aldrich), 5 μg/mL insulin (I9278; Sigma-Aldrich), and 50 μg/mL gentamicin (15750; Gibco Life Technologies). The suspension was centrifuged at 1500 rpm for 10 min to remove cellular debris, and the pellet was treated with 2 U/μL DNase (D4263; Sigma-Aldrich). Tumor organoids were separated from single cells by differential centrifugation. For control experiments, tumor organoids were embedded in 7mg/mL rat tail collagen-I (354249, Corning) gels at 2-3 organoids/μL as 150μL suspensions an plated in a 24-well multiwell glass bottom plate (662892; Greiner Bio-One). Each well was cultured with "organoid media": DMEM/F12 (10565-018, Gibco), 1% v/v insulin, transferrin, selenium (51500, ThermoFisher) and 1% v/v penicillin/streptomycin (15140-122, Gibco) supplemented with 2.5 nM FGF2 (F0291, Sigma).

Fabrication of perfusable microvessel device

The microvessel platform is fabricated as previously described (21). Briefly, high concentration of rat tail collagen I (354249, Corning) is diluted to 7 mg/mL and neutralized with DI water, 10x PBS, and 1 N sodium hydroxide. After neutralization, tumor organoids are embedded into the collagen gel solution to a final concentration of 5 organoids/μL and randomly seeded surrounding a 150 μm diameter super-elastic nitinol wire (Malin Co.) within a Sylgard 184 polydimethylsiloxane (PDMS; Dow Corning) housing which is patterned using a custom-made aluminum mold. After 45 min gelation at 37°C, the rod is removed, leaving behind a cylindrical channel within the collagen gel. The channel is subsequently coated with fibronectin (50 μg/mL, F2006; Sigma) to promote endothelial adhesion and spreading. Endothelial cells in suspension are introduced into the channel at a concentration of 5 x 10^{-7} cells/mL and allowed to settle and actively adhere to the channel walls. After the endothelial cells have spread for about 2 h, NGM is perfused through the vessel at a physiological relevant shear stress of approximately 4 dynes/cm^2 under a steady laminar flow at a rate of 1 mL/h (Fig. 2). The devices are then tested for functional properties, such as vessel permeability and expression of relevant junctional proteins.

In order to fix the distance of the tumor to the vessel, a slight modification was added to the platform described above. A second cylindrical template rod is introduced within the PDMS housing parallel to the first template rod (Fig. 6). Once the two rods are placed into the PDMS housing, the collagen solution is introduced and allowed to gel for 45 min at 37°C. Tumor organoids are then embedded at high concentration in 3mg/mL collagen I gels (354236, Corning) and introduced into the inlet. One of the rods is then slowly removed allowing the introduction of the tumor suspension into the cylindrical channel. The devices are then incubated for 15-20 min at 37°C. The second channel is then removed following the steps described above for vessel formation.

Microscopy and image analysis

Whole slide tissue scan for *in vivo* analysis was performed on 40 µm sections of orthotopic tumors mounted onto positively-charged slides. Stained slides were mounted with Fluoromount Aqueous Mounted Medium (Sigma; F4680) and covered with rectangular #1.5 High Precision 24x50mm, 170µm-thick Microscope Cover Glasses (Thor Labs; CG15KH). Mounted slides were then scanned with AxioScan.Z1 (Zeiss) using Zen Blue 2.1 with the following configurations: Fluar 5x/0.27NA M27 objective for coarse focus mapping, Plan-Apochromat 20x/0.80NA M27 objective for fine focus mapping, Hamamatsu Orca Flash 4.0 (fluorescence) camera for image capture, and Colibri 7 VIS-

LED fluorescent light source. To detect DAPI, mGFP, mTomato, and AlexaFluor 647, the following light sources and filter sets were used, respectively: 96 HE BFP (LED module 385nm) at 50% intensity and 1.004ms exposure, Excitation BP 390/40 and Emission BP 450/40 filter; 38 HE GFP (LED module 475nm) at 50% intensity and 31.504ms exposure, Excitation BP 470/40 and Emission BP 525/50 filter; 43 HE DsRed (LED module 567nm) at 50% intensity and 17.204ms exposure, Excitation BP 550/25 and Emission BP 605/70 filter; 50 Cy5 (LED module 630nm) at 50% intensity and 123.404 ms exposure, Excitation BP 640/30 and Emission BP 690/50 filter. Z-stacks were taken at every 1µm for a range of 16µm (15 stacks), with scaling-per-pixel at 0.163µm x 0.163µm x 1µm, and stored in raw (.czi file) format with JpgXr lossless compression. ImageJ and Imaris software (Bitplane Scientific, Zurich, Switzerland) were used for image analysis and to adjust brightness and contrast across entire images to maximize image clarity.

Microvessels were imaged on a Nikon TE-2000 U microscope (Nikon Instruments Inc., Melville, NY). Time-lapse fluorescence and phase-contrast images, tracer molecules for vessel permeability measurements and fluorescent proteins were excited with a Nikon Intensilight epifluorescence illuminator, detected with an ET Sedat Quad band 89000 filter set (Chroma Technology Corp, Bellows Falls, VT), using a 10x phase-contrast objective (N.A. 0.3), and captured with a Nikon DS-Qi1Mc camera. Confocal images were captured on a Zeiss 780 laser-scanning confocal microscope (Carl Zeiss Microscopy). Differential interference contrast (DIC) microscopy images were captured with an LD Plan-Neofluar 20×/0.4 Korr Ph2 objective lens and a Cell Observer system with an AxioObserver Z1 and an AxioCam MRM camera (Carl Zeiss).

Measurement of permeability and focal leaks

Upon formation and maturation of endothelial vessels, and tumor-vessel interactions, permeability was simultaneously measured for three different fluorescent molecular weight probes introduced into the input port through the vessel lumen at a final concertation of 5ug/mL 3 kDa dextran (Alexa Flour-488-conjugated), 62.5 ug/mL 10 kDa dextran (Alexa Flour-647-conjugated) and 10 ug/mL 70 kDa dextran (Texas Red), respectivley. All fluorescently labeled dextran molecules were diluted in NGM prior to perfusion through the platform. Widefield epifluorescence images capturing fluorophores introduced through the microvessels and leakage into the ECM were acquired with a 4x objective over at least 1 h time period at 2 min intervals. Calibration experiments were performed to optimize image acquisition such that a linear relation between concentration and fluorescence intensity was present at least 10 times above and below the perfused concentrations of tracer molecules.

To measured permeability using 3D engineered microvessel devices, the following equation was used: $P_{3D} = (1/\Delta I_f)\ (dI_f/dt)\ (d/4)$, where ΔI_f is the initial increase in fluorescence intensity (when the vessel is being filled with the fluorescent probe), (dI_f/dt) is the rate of increase in fluorescence intensity as the solute is being transported from the vessel to the ECM and d is the diameter of the vessel (26). Permeability coefficients were calculated in cm/s. The fluorescent intensity values obtained over time were divided in 3 regions: (i) the "noise region" (prior to the vessel being filled with the fluorescent probe), (ii) when the vessel is being filled with the fluorescent probe (ΔI_f), and iii) when the fluorescent probe permeates into the ECM (Fig. 3). In order to automate the calculation of permeability an algorithm was developed to calculate permeability coefficients for all fluorescent molecular probes. Each microvessel time-lapse image was divided in ten region of interest (ROI) of equal size and the fluorescent intensity values were calculated over time for the different fluorescent probes using Fiji. Once all data values were obtained, the strategy was to find the inflection point marking the transition where the vessel has been completely filled with fluorescent dye and starts the diffusion towards the ECM. In order to properly find the relevant inflection point, a polynomial of degree six was used to fit the data for each of the ROIs and each fluorescent probe. The "noise region" was excluded from the original data to ensure a good fit of the polynomial and to better estimate the relevant inflection point. To properly identify the "noise region" the following iterative approach was used. This step starts by using all data available and continues excluding data by applying the absolute value of the growth rate of the fluorescent intensity (using 1% increments). Following this procedure in an iterative manner, the data that was finally used to fit the polynomial was selected after the inflection points identified became stable after at least three iterations. In case one or more inflection point(s) was/were identified, the relevant inflection point for our analysis was determined as the first one where the second derivate changed from negative to positive (concave down to concave up). If the inflection point of interest was not found the data for such ROI was not used. Once the relevant infection point was identified, the ΔI_f was determined and (dI_f/dt) was calculated after the relevant inflection point using all available data stopping if a subsequent inflection point was found.

Focal leaks were calculated as previously described (26). Briefly, the contrast in the fluorescence images taken for the permeability assay was maximized to examine for any nonuniformities (i.e., excess of fluorescence intensity regions) in the length of the microvessel. Focal leaks (FL) were quantify overtime using the following equation: FL=

$n_{leaks} / (n_{images} \quad l\ L)$, where n_{leaks} is the total number of focal leaks counted overtime, n_{images} is the number of time points imaged, and L is the length of the microvessel imaged.

Orthotopic transplantation to mammary fat pad

Tumor organoids from MMTVPyMT;ROSAmT/mG, were resuspended in a 50% (vol/vol) DMEM/50% (vol/vol) Matrigel (354230; Corning) solution at a density of 25-40 organoids/μL and kept at 4°C during transplantation. We conducted orthotopic transplantations into 3- to 4-week-old NSG mice in a sterile hood. In brief, the mice were anesthetized with 2.5% isoflurane, immobilized and the surgical site was made sterile using ethanol. The mammary gland was exposed by a 1-cm mid-sagittal cut followed by a 0.5-cm oblique cut from the initial incision to one hip. The skin was then retracted to expose the number 4 mammary gland. The number 5 gland and the lymph node in the number 4 gland were removed. 10-20 μL of organoid suspension was injected into the number 4 gland using a syringe (702RN(7636–01); Hamilton; custom 1-in needles, 26 gauge). The skin was then locally infiltrated with 5–10 μL of 0.25% bupivacaine. The same procedure was repeated in the contralateral mammary gland. The surgical wounds were closed using 9-mm autoclips and tissue glue. Triple antibiotic ointment was applied to the incision. The mice were closely monitored, and autoclips were removed 10 days postsurgery. Tumors were harvested between 6 and 10 weeks.

Immunofluorescence staining

Orthotopic primary tumors were collected, fixed, and stained as previously described (6). Briefly, whole orthotopic primary tumors were fixed in 4% paraformaldehyde for 4 h and incubated in a 25% sucrose solution overnight. Whole tumors were then embedded in Tissue Tek Optimal Cutting Temperature compound (OCT, Sakura) and frozen at −80 °C.

OCT blocks were sectioned at 40 µm thickness using a Leica cryostat (Leica Biosystems) set to −27 °C. Sections were placed on Superfrost Plus Gold microscope slides (15-188-48; Fisherbrand) and stored at -80°C. For antibody staining, slides were thawed at ambient temperature, rinsed twice with PBS to remove OCT and permeabilized with 0.5% Triton X-100 for 1 h. Samples were then blocked with 10% FBS/ 1% BSA in PBS for 2-3 h and incubated with primary antibody solution overnight at 4°C in 1% FBS/ 1%BSA in PBS. Slides were then rinsed twice in PBS with 10% FBS/1% BSA and then incubated with secondary antibodies diluted in PBS with 1%FBS/ 1% BSA overnight at 4°C. Slides were rinsed twice in PBS with 1% FBS/1% BSA for 10 min and once in PBS for 10 min. Slides were mounted using Fluoromount Aqueous Mounted Medium (Sigma; F4680) and covered with rectangular #1.5 High Precision 24x50 mm, 170 µm-thick Microscope Cover Glasses (Thor Labs; CG15KH). Immunofluorescent staining for each antibody was done for at least three independent biological replicates. Rabbit anti-CD31 (Abcam; ab28364; 1:100) were used as primary antibodies. Goat anti-rabbit AlexaFluor 647 (ThermoFisher; A32733; 1:200) were used as secondary antibodies. Nuclei were stained with DAPI (Roche; 10236276001; 1:1000).

Immunofluorescence staining for microvessel devices was performed within the vessel platform. The vessels were washed with PBS for 5 min, fixed with 3.7% paraformaldehyde (Sigma) for 15 min, permeabilized with 0.1% Triton X-100 (Sigma) for 15 min, and blocked with 10% FBS overnight at 4 °C. Microvessels were incubated overnight at 4 °C with anti-β-catenin (E-5) primary antibody (Santa Cruz, sc-7963,1:300) and for 20 min at room temperature with goat anti-Mouse IgG (H+L), Alexa Fluor Plus 488 (ThermoFisher Scientific, A32723, 1:100). Nuclei was stained using DAPI solution (Invitrogen, D3571, 1:1000). Confocal z-stack images were captured on a Zeiss 780 laser-scanning confocal microscope (Carl Zeiss Microscopy). To fully reconstruct microvessels, approximately four hundred 0.5 μm slices were acquired using a 40X objective.

Endothelial cell proliferation and cell death analysis

Phase-contrast and fluorescence time-lapse images were captured every 20 min and analyzed using Fiji. Endothelial monolayers located at the top and bottom regions of the vessel were analyzed for proliferation and cell death events (27-29). Proliferating cells were distinguished by the increased rounding in the cell shape prior to cell division that generates a visible halo around the cell body that can be follow until the two daughter cells reincorporate into the monolayer (Supplemental Fig. 3, Supplemental Movie 8). The number of endothelial cell divisions was counted along three different regions per vessel overtime and was divided by the total number of cells within the assessed region of the monolayer at the beginning of the time-lapse. The rate of cell proliferation is calculated as percent per hour (% cell division/h). Endothelial cell death was also detected by direct observation of individual cells within the monolayer detaching and producing a cellular debris that is taken by the flow during the preceding frames. Similar to the endothelial cell proliferation the rate of cell death is calculated as percent per hour (% cell death/h; Supplemental Fig. 3)

Statistics

All statistical analyses were conducted using STATA or Graphpad Prism. STATA was used to create the algorithm to calculate permeability. Data was evaluated for normality using D'Agostino-Pearson omnibus test. P value was determined by one-way ANOVA or

Mann-Whitney test if the data did not present a normal distribution. $P < 0.05$ was considered significant. Column plots report s.e.m. All data represent at least three biological replicates.

Acknowledgements

We thank members of the Ewald and Searson laboratories for helpful comments. We thank Venna Padmanaban for help with *in vivo* work and Seyvonne Ip for help with image analysis. A.J.E. is supported by a Research Scholar Grant (RSG-12-141-01-CSM) from the American Cancer Society, by funds from the NIH/NCI (P30 CA006973), by funds from the Cindy Rosencrans Fund for Triple Negative Breast Cancer Research, by a Research Leadership Award from the Metastatic Breast Cancer Network, and by an award from The Pink Agenda and The Breast Cancer Research Foundation.

References

1. Hanahan, D. and R.A. Weinberg, *Hallmarks of cancer: the next generation.* Cell, 2011. 144(5): p. 646-74.
2. Reddy, B.Y., et al., *The Microenvironmental Effect in the Progression, Metastasis, and Dormancy of Breast Cancer: A Model System within Bone Marrow.* Int J Breast Cancer, 2012. 2012: p. 721659.
3. Liotta, L.A., M.G. Saidel, and J. Kleinerman, *The significance of hematogenous tumor cell clumps in the metastatic process.* Cancer Res, 1976. 36(3): p. 889-94.
4. Moore, G.E., A.A. Sandberg, and A.L. Watne, *The comparative size and structure of tumor cells and clumps in the blood, bone marrow, and tumor imprints.* Cancer, 1960. 13: p. 111-7.
5. Aceto, N., et al., *Circulating tumor cell clusters are oligoclonal precursors of breast cancer metastasis.* Cell, 2014. 158(5): p. 1110-1122.
6. Cheung, K.J., et al., *Polyclonal breast cancer metastases arise from collective dissemination of keratin 14-expressing tumor cell clusters.* Proc Natl Acad Sci U S A, 2016. 113(7): p. E854-63.
7. Wirtz, D., K. Konstantopoulos, and P.C. Searson, *The physics of cancer: the role of physical interactions and mechanical forces in metastasis.* Nat Rev Cancer, 2011. 11(7): p. 512-22.
8. Chambers, A.F., A.C. Groom, and I.C. MacDonald, *Dissemination and growth of cancer cells in metastatic sites.* Nat Rev Cancer, 2002. 2(8): p. 563-72.
9. Steeg, P.S., *Tumor metastasis: mechanistic insights and clinical challenges.* Nat Med, 2006. 12(8): p. 895-904.
10. Carmeliet, P., *Mechanisms of angiogenesis and arteriogenesis.* Nat Med, 2000. 6(4): p. 389-95.
11. Folkman, J., et al., *Induction of angiogenesis during the transition from hyperplasia to neoplasia.* Nature, 1989. 339(6219): p. 58-61.
12. Ziyad, S. and M.L. Iruela-Arispe, *Molecular mechanisms of tumor angiogenesis.* Genes Cancer, 2011. 2(12): p. 1085-96.
13. Katt, M.E., A.D. Wong, and P.C. Searson, *Dissemination from a Solid Tumor: Examining the Multiple Parallel Pathways.* Trends Cancer, 2018. 4(1): p. 20-37.
14. Siemann, D.W., *The unique characteristics of tumor vasculature and preclinical evidence for its selective disruption by Tumor-Vascular Disrupting Agents.* Cancer Treat Rev, 2011. 37(1): p. 63-74.
15. Maddipati, R. and B.Z. Stanger, *Pancreatic Cancer Metastases Harbor Evidence of Polyclonality.* Cancer Discov, 2015. 5(10): p. 1086-97.
16. Cheung, K.J., et al., *Collective invasion in breast cancer requires a conserved basal epithelial program.* Cell, 2013. 155(7): p. 1639-51.
17. Hashizume, H., et al., *Openings between defective endothelial cells explain tumor vessel leakiness.* Am J Pathol, 2000. 156(4): p. 1363-80.
18. Wong, A.D., et al., *Quantitative Analysis of the Enhanced Permeation and Retention (EPR) Effect.* PLoS One, 2015. 10(5): p. e0123461.
19. Chang, Y.S., et al., *Mosaic blood vessels in tumors: frequency of cancer cells in contact with flowing blood.* Proc Natl Acad Sci U S A, 2000. 97(26): p. 14608-13.
20. Willis, R.A., *Tumor seminar.* Tex State J Med, 1950. 46(8): p. 611-38.

21. Wong, A.D. and P.C. Searson, *Live-cell imaging of invasion and intravasation in an artificial microvessel platform.* Cancer Res, 2014. 74(17): p. 4937-45.

22. Guy, C.T., R.D. Cardiff, and W.J. Muller, *Induction of mammary tumors by expression of polyomavirus middle T oncogene: a transgenic mouse model for metastatic disease.* Mol Cell Biol, 1992. 12(3): p. 954-61.

23. Muzumdar, M.D., et al., *A global double-fluorescent Cre reporter mouse.* Genesis, 2007. 45(9): p. 593-605.

24. Seandel, M., et al., *Generation of a functional and durable vascular niche by the adenoviral E4ORF1 gene.* Proc Natl Acad Sci U S A, 2008. 105(49): p. 19288-93.

25. Nguyen-Ngoc, K.V., et al., *3D culture assays of murine mammary branching morphogenesis and epithelial invasion.* Methods Mol Biol, 2015. 1189: p. 135-62.

26. Chrobak, K.M., D.R. Potter, and J. Tien, *Formation of perfused, functional microvascular tubes in vitro.* Microvasc Res, 2006. 71(3): p. 185-96.

27. Bogorad, M.I., et al., *Tissue-engineered 3D microvessel and capillary network models for the study of vascular phenomena.* Microcirculation, 2017. 24(5).

28. DeStefano, J.G., et al., *Real-time quantification of endothelial response to shear stress and vascular modulators.* Integr Biol (Camb), 2017. 9(4): p. 362-374.

29. Huxley, V.H., F.E. Curry, and R.H. Adamson, *Quantitative fluorescence microscopy on single capillaries: alpha-lactalbumin transport.* Am J Physiol, 1987. 252(1 Pt 2): p. H188-97.

30. Adamson, R.H., et al., *Microvascular permeability and number of tight junctions are modulated by cAMP.* Am J Physiol, 1998. 274(6 Pt 2): p. H1885-94.

31. He, P., M. Zeng, and F.E. Curry, *Dominant role of cAMP in regulation of microvessel permeability.* Am J Physiol Heart Circ Physiol, 2000. 278(4): p. H1124-33.

32. Armstrong, J.K., et al., *The hydrodynamic radii of macromolecules and their effect on red blood cell aggregation.* Biophys J, 2004. 87(6): p. 4259-70.

33. Dreher, M.R., et al., *Tumor vascular permeability, accumulation, and penetration of macromolecular drug carriers.* J Natl Cancer Inst, 2006. 98(5): p. 335-44.

34. Harney, A.S., et al., *Real-Time Imaging Reveals Local, Transient Vascular Permeability, and Tumor Cell Intravasation Stimulated by TIE2hi Macrophage-Derived VEGFA.* Cancer Discov, 2015. 5(9): p. 932-43.

35. Price, G.M., et al., *Effect of mechanical factors on the function of engineered human blood microvessels in microfluidic collagen gels.* Biomaterials, 2010. 31(24): p. 6182-9.

36. Jain, R.K., *Molecular regulation of vessel maturation.* Nat Med, 2003. 9(6): p. 685-93.

37. Tong, R.T., et al., *Vascular normalization by vascular endothelial growth factor receptor 2 blockade induces a pressure gradient across the vasculature and improves drug penetration in tumors.* Cancer Res, 2004. 64(11): p. 3731-6.

38. El Hallani, S., et al., *A new alternative mechanism in glioblastoma vascularization: tubular vasculogenic mimicry.* Brain, 2010. 133(Pt 4): p. 973-82.

39. Hendrix, M.J., et al., *Vasculogenic mimicry and tumour-cell plasticity: lessons from melanoma.* Nat Rev Cancer, 2003. 3(6): p. 411-21.

40. Yang, J.P., et al., *Tumor vasculogenic mimicry predicts poor prognosis in cancer patients: a meta-analysis.* Angiogenesis, 2016. 19(2): p. 191-200.

41. Atkin, G., A. Chopada, and I. Mitchell, *Colorectal cancer metastasis: in the surgeon's hands?* Int Semin Surg Oncol, 2005. 2(1): p. 5.

42. Park, S.Y., et al., *Influence of surgical manipulation and surgical modality on the molecular detection of circulating tumor cells from colorectal cancer.* J Korean Surg Soc, 2012. 82(6): p. 356-64.

43. Li, W., et al., *Laparoscopic surgery minimizes the release of circulating tumor cells compared to open surgery for hepatocellular carcinoma.* Surg Endosc, 2015. 29(11): p. 3146-53.

44. Fan, Z.C., et al., *Real-time monitoring of rare circulating hepatocellular carcinoma cells in an orthotopic model by in vivo flow cytometry assesses resection on metastasis.* Cancer Res, 2012. 72(10): p. 2683-91.

45. Nagakawa, Y., et al., *Histologic features of venous invasion, expression of vascular endothelial growth factor and matrix metalloproteinase-2 and matrix metalloproteinase-9, and the relation with liver metastasis in pancreatic cancer.* Pancreas, 2002. 24(2): p. 169-78.

46. Helmlinger, G., et al., *Solid stress inhibits the growth of multicellular tumor spheroids.* Nat Biotechnol, 1997. 15(8): p. 778-83.

47. Padera, T.P., et al., *Pathology: cancer cells compress intratumour vessels.* Nature, 2004. 427(6976): p. 695.

48. Kienast, Y., et al., *Real-time imaging reveals the single steps of brain metastasis formation.* Nat Med, 2010. 16(1): p. 116-22.

49. Fang, J., H. Nakamura, and H. Maeda, *The EPR effect: Unique features of tumor blood vessels for drug delivery, factors involved, and limitations and augmentation of the effect.* Adv Drug Deliv Rev, 2011. 63(3): p. 136-51.

50. Wong, A.D., et al., *Chemotherapeutic Drug Delivery and Quantitative Analysis of Proliferation, Apoptosis, and Migration in a Tissue-Engineered Three-Dimensional Microvessel Model of the Tumor Microenvironment.* ACS Biomaterials Science & Engineering, 2019. 5(2): p. 633-643.

51. Yuan, F., et al., *Vascular permeability in a human tumor xenograft: molecular size dependence and cutoff size.* Cancer Res, 1995. 55(17): p. 3752-6.

52. Aaboud, M., et al., *Search for the Dimuon Decay of the Higgs Boson in pp Collisions at sqrt[s]=13 TeV with the ATLAS Detector.* Phys Rev Lett, 2017. 119(5): p. 051802.

53. Veitenhansl, M., et al., *40(th) EASD Annual Meeting of the European Association for the Study of Diabetes : Munich, Germany, 5-9 September 2004.* Diabetologia, 2004. 47(Suppl 1): p. A1-A464.

Figure 4-1. Identification of mosaic vessels in primary metastatic breast cancer tumors. *ROSA*^{mTmG}*; MMTV-PyMT* tumor organoids were transplanted into nonfluorescent NSG host mice to unambiguously identify tumor tissue in contact with vessels stained with anti-CD31 (green). (A) Representative 2D projection of a fluorescence z-stack image of a primary tumor section showing vessels stained with anti-CD31 (green) and DAPI (52). (B) 2D projection of a fluorescence z-stack image of a primary tumor section showing a partially lined vessel in which tumor cells are in apparent contact with the vessel lumen (arrowheads mark a region lacking detectable CD31 immunoreactivity) and, (C) a fully lined vessel. Scale bar: 30 μm. (D) Representative 3D projection of a fluorescence z-stack image of a primary tumor section stained with PECAM-1/CD31 (green) and DAPI. (E) 3D projection of a fluorescence z-stack image of a primary tumor section showing a mosaic vessel in which tumor cells are in apparent contact with the vessel lumen (arrowheads mark a region lacking detectable CD31 immunoreactivity) and, (F) a fully lined vessel. Scale bar: 30 μm. Tissue depth between each section, 1μm. Total tissue depth, 16 μm.

Figure 4-1.

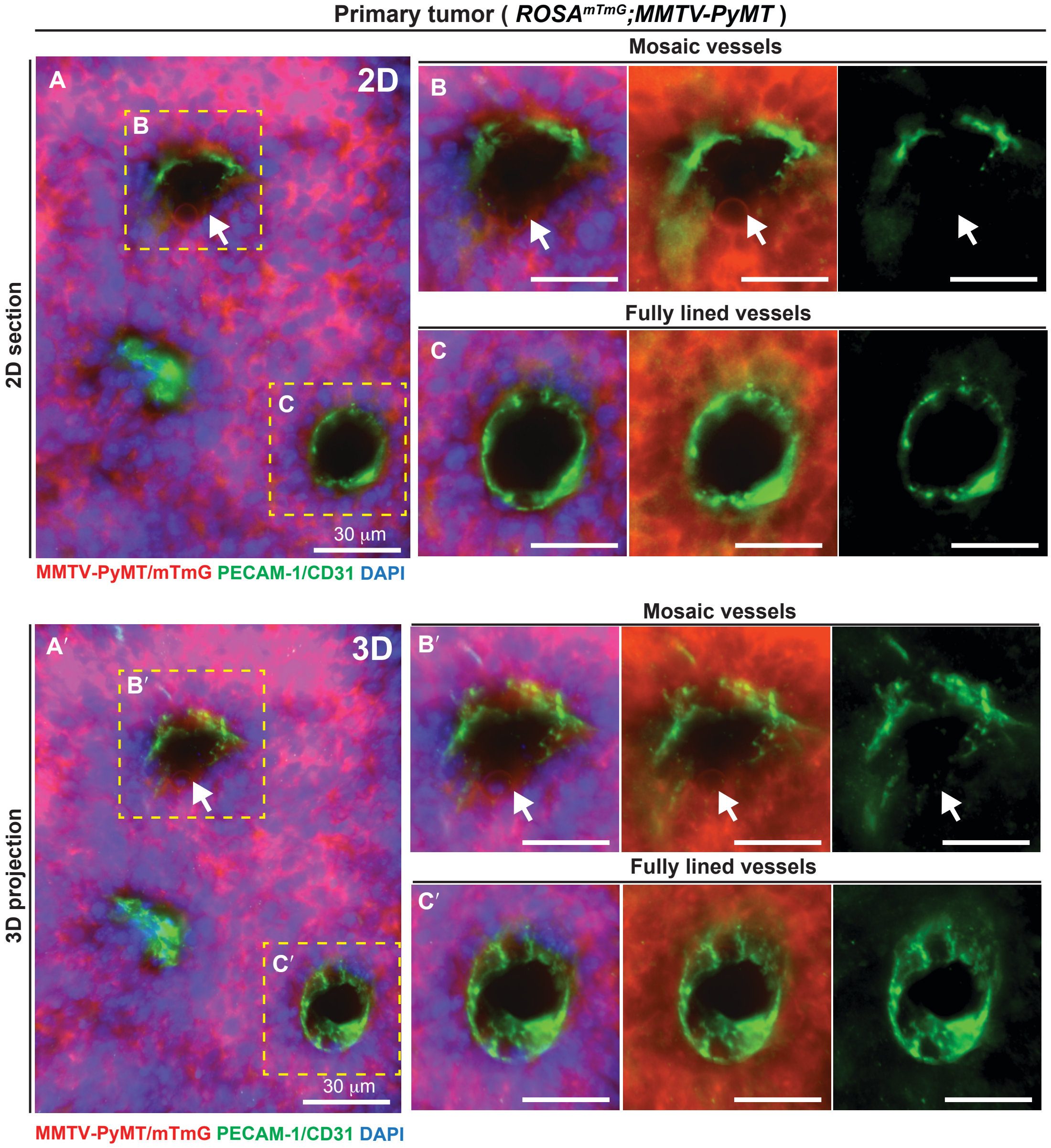

Table 1. Quantification of mosaic vessels in orthotopic primary tumors

Tumor mice	Total no. of vessels	No. of mosaic vessels	% mosiac vessels	Av. mosaic vessel diameter (µm)
1	783	75	9.6	157.9
2	845	43	5.1	91.1
3	1221	50	4.1	60.2
Total	2681	168	Mean 6.3	103.1
			SD 2.9	49.9

Figure 4-2. Coculture of mammary gland tumor organoids into a perfusable 3D microvessel platform.

(A) Schematic representation of 3D organotypic culture of *ROSA*^{mTmG}*; MMTV-PyMT* tumor organoids seeded into a vessel device. (B) Schematic illustration of the side- and end-view of a 150 μm diameter microvessel design and fabrication. Tumor organoids embedded in collagen-I gels are seeded surrounding a cylindrical metal rod. After the tumor/collagen solution gels, the rod is removed resulting in a bare channel which is perused with media and coated with fibronectin. Endothelial cells are then seeded resulting in a confluent 3D microvessel. The perfusion system is by gravity flow by differential pressure. Flow is kept at 1 mL/hour and a shear stress of 4 dynes/cm^2. (C) Schematic illustration of imaging focused at the mid-plane of the vessel and the resulting 2D projected image (right). The vessel appears hollow and media through the vessel lumen can diffuse out into the ECM (D) Confocal image of a vessel stained with b-catenin (green) and DAPI. Images show three focal planes: side view, mid-plane and a cross-section (end-view) of a z-stack image. (E) Fluorescence microscopy image of tumor organoids (red) embedded in collagen-I solution surrounding a vessel (green). (F) Inset showing a 3D cross-section of a confocal z-stack image of tumor organoids near a vessel. Arrow, direction of flow. Scale bar: 150 μm.

Figure 4-2.

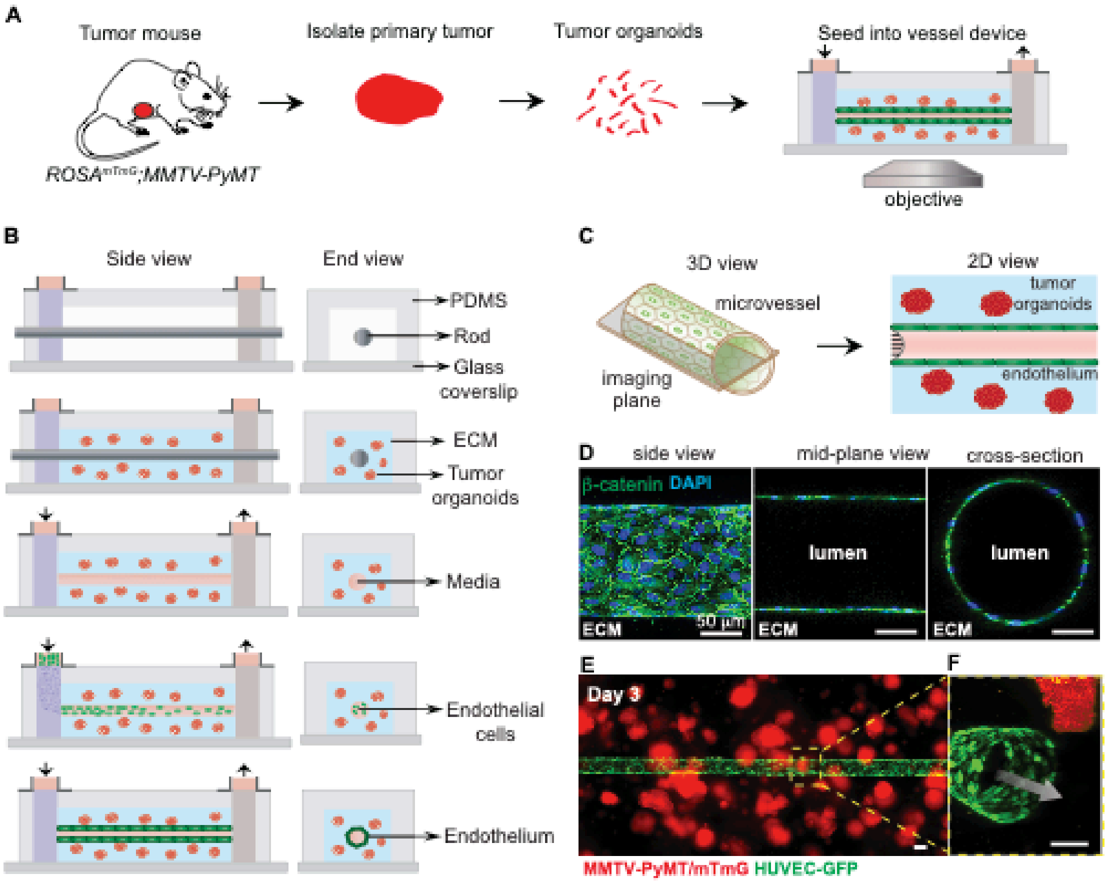
A
Tumor mouse
Isolate primary tumor
Tumor organoids
Seed into vessel device
ROSA^mTmG;MMTV-PyMT
objective
B
Side view
End view
PDMS
Rod
Glass coverslip
ECM
Tumor organoids
Media
Endothelial cells
Endothelium
C
3D view
microvessel
imaging plane
2D view
tumor organoids
endothelium
D
side view
mid-plane view
cross-section
β-catenin DAPI
lumen
lumen
ECM
50 μm
ECM
ECM
E
Day 3
F
MMTV-PyMT/mTmG HUVEC-GFP

Figure 4-3. Microvessel integrity and functionality in the presence of tumor organoids. Representative fluorescence time-lapse microscopy images of a microvessel co-cultured with *ROSAmTmG; MMTV-PyMT* tumor organoids and control without tumor organoids. Permeability was assessed by simultaneously perfusing three different fluorescent molecular weight probes through the vessel lumen. (A-D) 70 kDa dextran (Texas Red). Time = 0 min represents the frame prior to luminal filling (A'-D') which occurs on average at 20 min. (A"-D") After luminal filing the fluorescence probes perfuse out of the vessel into the ECM. (E) Permeability of 70 kDa dextran molecular probe increases in the presence of tumor organoids compared to control vessel devices without tumor organoids and decreases when treated with 400 μM dibutyryl-cAMP (db-cAMP) for 24 h. n= number of permeability values calculated for at least 3 biological replicates. Error bars indicate s.e.m. P values were determined by the Mann-Whitney test. Differences were considered statistically significant for $p < 0.05$. Images and analysis of the other two molecular probes in Supplemental Fig. 2. (F-F') Representative fluorescence time-lapse microscopy images of a vessel cocultured with tumor organoids with poor barrier function showing transient focal leaks of 10 kDa dextran(Alexa Flour-647-conjugated) probe after luminal vessel filling. The arrows indicate focal leaks along the vessel wall through time. These transient leaks are likely due to temporary disruption at cell-cell junctions, which is consistent with a molecular cut off size larger than 3 kDa suggesting paracellular transport. The flow rate is kept at 1mL/hour and at a shear stress of 4 dynes/cm2. The direction of the flow is from the left to the right of the images. (G) The average number of focal leaks per mm of microvascular vessel increases in the presence of tumor organoids compared to control vessel devices and decreases upon treatment with db-cAMP. n= number of vessel devices for 3 biological replicates. Error bars indicate s.e.m. P values were determined by the Mann-Whitney test. Differences were considered statistically significant for $p < 0.05$. (H) Positive correlation between focal leaks and permeability. The measure Corr(P3D, Focal leaks) indicates the so called Pearson's correlation coefficient which is a measure of the strength and direction of association that exists between two continuous variables. It ranges between -1 (perfect negative association) to 1 (perfect positive association). A value of 0 would indicate no association between two continuous variables. Representative images and results for permeability of 3 and 10 kDa dextrans are shown in Supplemental Fig. S3.

Figure 4-3.

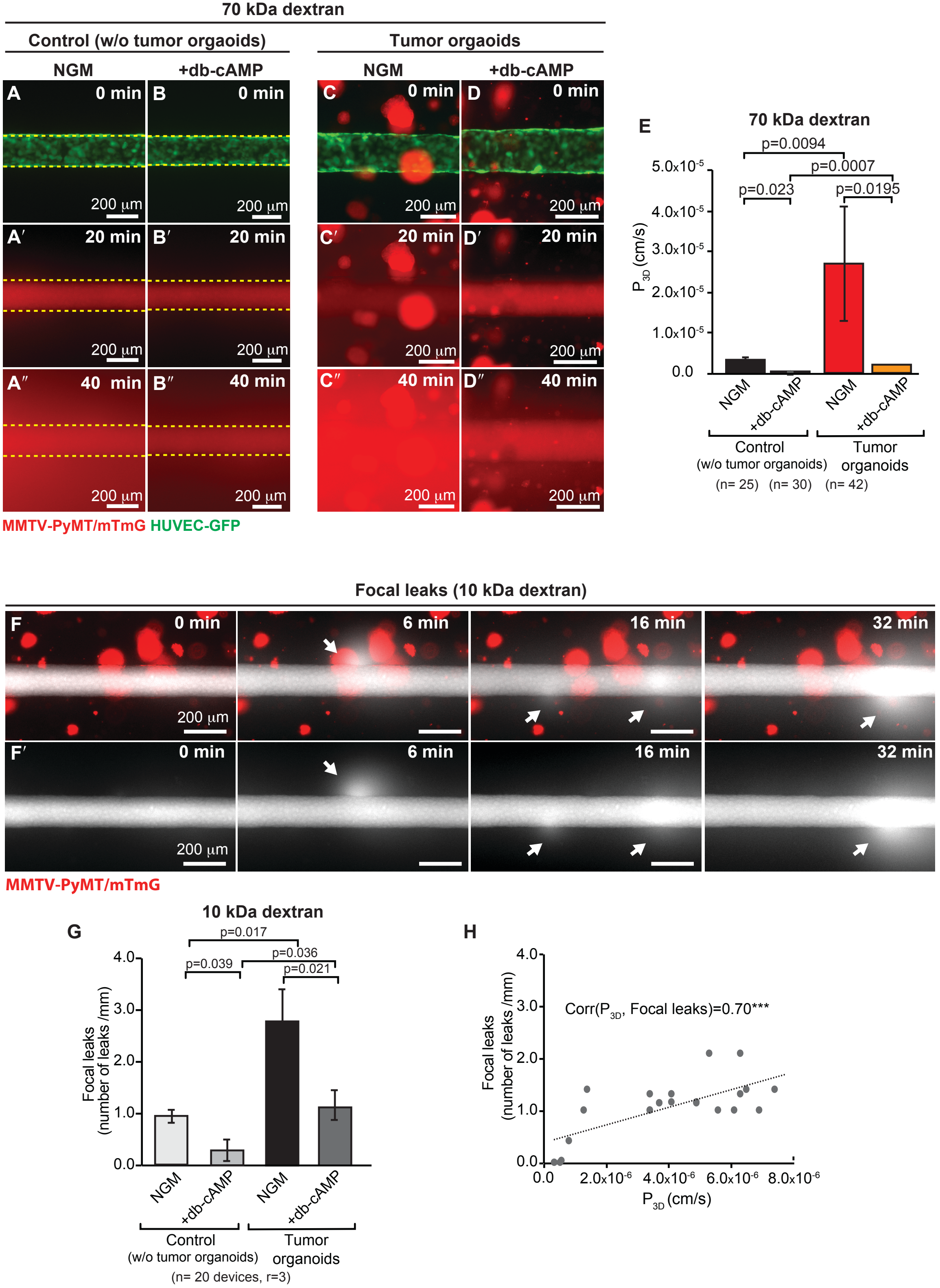
70 kDa dextran
Control (w/o tumor orgaoids)
Tumor orgaoids
NGM
+db-cAMP
A 0 min
B 0 min
C 0 min
D 0 min
A′ 20 min
B′ 20 min
C′ 20 min
D′ 20 min
A″ 40 min
B″ 40 min
C″ 40 min
D″ 40 min
200 μm
MMTV-PyMT/mTmG HUVEC-GFP
E
70 kDa dextran
p=0.0094
p=0.0007
p=0.023
p=0.0195
P3D (cm/s)
5.0x10-5
4.0x10-5
3.0x10-5
2.0x10-5
1.0x10-5
0.0
NGM
+db-cAMP
Control (w/o tumor organoids)
Tumor organoids
(n= 25) (n= 30) (n= 42)
Focal leaks (10 kDa dextran)
F 0 min
6 min
16 min
32 min
F′ 0 min
200 μm
MMTV-PyMT/mTmG
G
10 kDa dextran
p=0.017
p=0.039
p=0.036
p=0.021
Focal leaks (number of leaks /mm)
4.0
3.0
2.0
1.0
0.0
NGM
+db-cAMP
Control (w/o tumor organoids)
Tumor organoids
(n= 20 devices, r=3)
H
Corr(P3D, Focal leaks)=0.70***
Focal leaks (number of leaks /mm)
0.0
2.0x10-6
4.0x10-6
6.0x10-6
8.0x10-6
P3D (cm/s)

Figure 4-4. Tumor organoids integrate with the endothelial vessel wall and are the most frequent type of tumor-vessel interactions *in vitro*. Representative fluorescence time-lapse images of a *ROSA*^{mTmG}*; MMTV-PyMT* tumor organoid growing near a microvessel (green). Direction of the flow is from left to right of the images. (A) Tumor organoid integrates with the vessel wall forming a mosaic vessel by day 6 in culture. The tumor cells are exposed to the vessel flow which is kept at 1mL/hour and at a shear stress of 4 dynes/cm^2. (A') 3D cross-section at the site of mosaic vessel formation. Scale bar: 100 µm. Arrowhead marks a region lacking endothelial cell lining. (B) Tumor organoid growing near a microvessel (behind the vessel in the image) completely constricts the vessel. By day 5 the flow rate decreased to less than 0.1 mL/h, resulting in increased intraluminal pressure reflected by upstream vessel expansion (B') 3D cross-section at the site of vessel constriction. Scale bar: 50 µm. Arrowhead marks a region of vessel contriction. (C) Tumor organoid deforms vessel wall by pulling on the endothelium by day 2 in culture. (C') 3D cross-section of a vessel pull. Scale bar: 100 µm. (D) Fluorecence time-lapse images showing retention of barrier function at site of tumor organoid contact with vessel wall. Vessel barrier function was assessed by perfusing two different fluorescent molecular weight probes through the vessel lumen: (D-F) 3 kDa dextran (Alexa Flour-488-conjugated), (D'-F') 10 kDa dextran (Alexa Flour-647-conjugated). Time= 0 min represents the frame prior to luminal filling. At 20 min. of luminal filling we observe retention of the tracer molecules at the site where the tumor organoid is in contact with the vessel wall suggesting the formation of a tumor-endothelial cell junction. Scale bar: 50 µm. (H) Quantification of tumor-vessel interactions showing mosaic vessels as the most frequent type observed *in vitro* compared to vessel constriction and vessel pull. Treatment with db-cAMP for 24 h decreases the number of interactions observed. Mosaic vessel number was determined by the retention of 10 kDa dextran (Alexa Flour-647-conjugated) as described in D-F. NGM: Normal growth medium. n= number of vessel devices for at least 3 biological replicates. Error bars indicate s.e.m. P values were determined by the Mann-Whitney test. Differences were considered statistically significant for $p< 0.05$.

Figure 4-4.

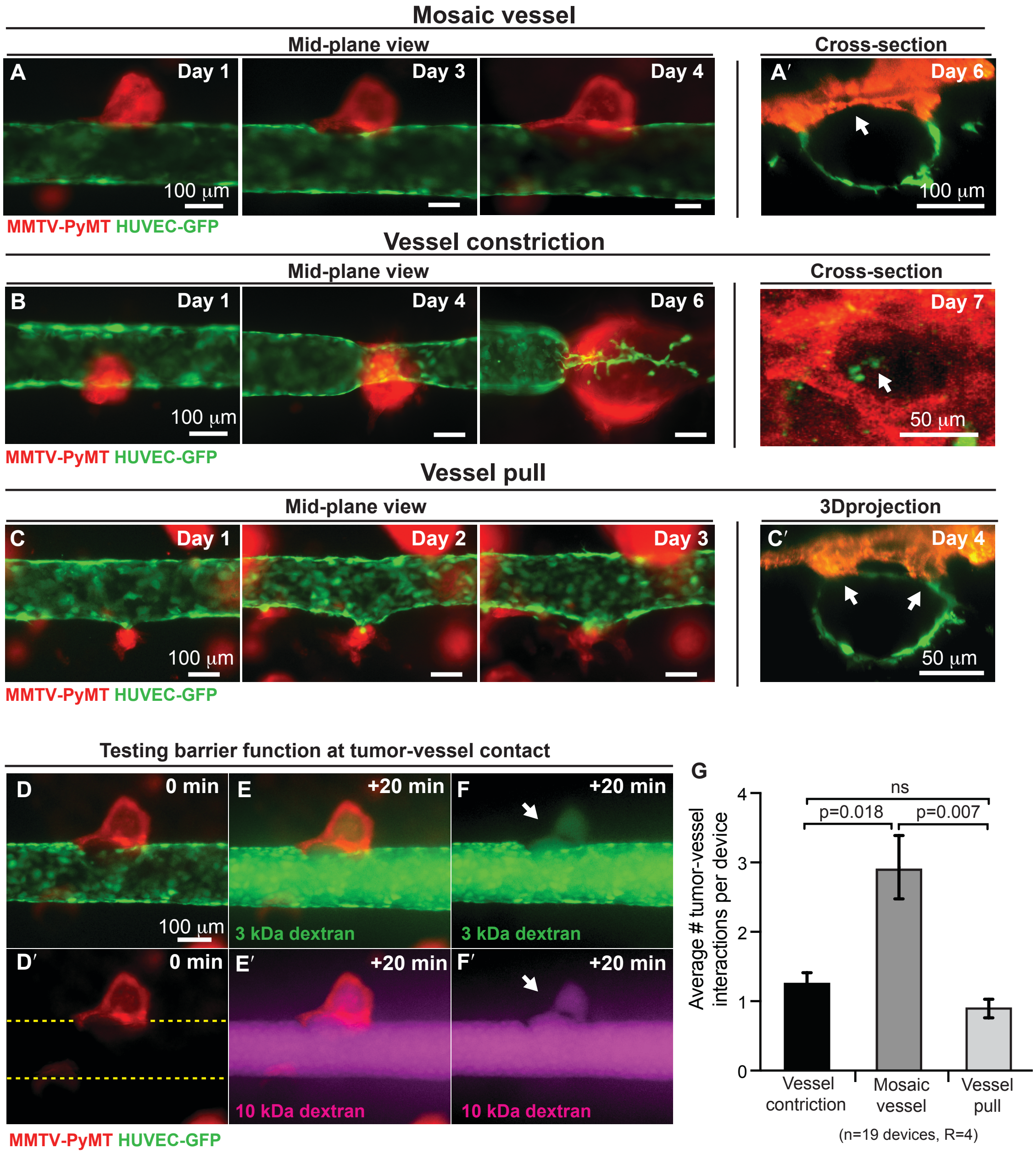
Mosaic vessel
Mid-plane view
Cross-section
A
Day 1
Day 3
Day 4
100 µm
A′
Day 6
100 µm
MMTV-PyMT HUVEC-GFP
Vessel constriction
Mid-plane view
Cross-section
B
Day 1
Day 4
Day 6
100 µm
Day 7
50 µm
MMTV-PyMT HUVEC-GFP
Vessel pull
Mid-plane view
3Dprojection
C
Day 1
Day 2
Day 3
100 µm
C′
Day 4
50 µm
MMTV-PyMT HUVEC-GFP
Testing barrier function at tumor-vessel contact
D
0 min
100 µm
E
+20 min
3 kDa dextran
F
+20 min
3 kDa dextran
D′
0 min
E′
+20 min
10 kDa dextran
F′
+20 min
10 kDa dextran
MMTV-PyMT HUVEC-GFP
G
Average # tumor-vessel interactions per device
0
1
2
3
4
ns
p=0.018
p=0.007
Vessel contriction
Mosaic vessel
Vessel pull
(n=19 devices, R=4)

Figure 4-5. Intravasation of a tumor cluster preceded by mosaic vessel formation. Frames from a representative (A) phase contrast and (B) fluorescent microscopy time-lapse movie of a *ROSA*^{mTmG}*; MMTV-PyMT* tumor organoid and a HUVEC microvessel (GFP). (A') Insets of phase and (B') fluorescent microscopy time-lapse images showing a tumor cluster shedding into the vessel lumen under continuous flow (yellow arrows). The flow rate is kept at 1mL/hour and at a shear stress of 4 dynes/cm^2. The direction of the flow is from the left to the right of the images. Scale bars: (A-B) 200 µm, (A'-B')

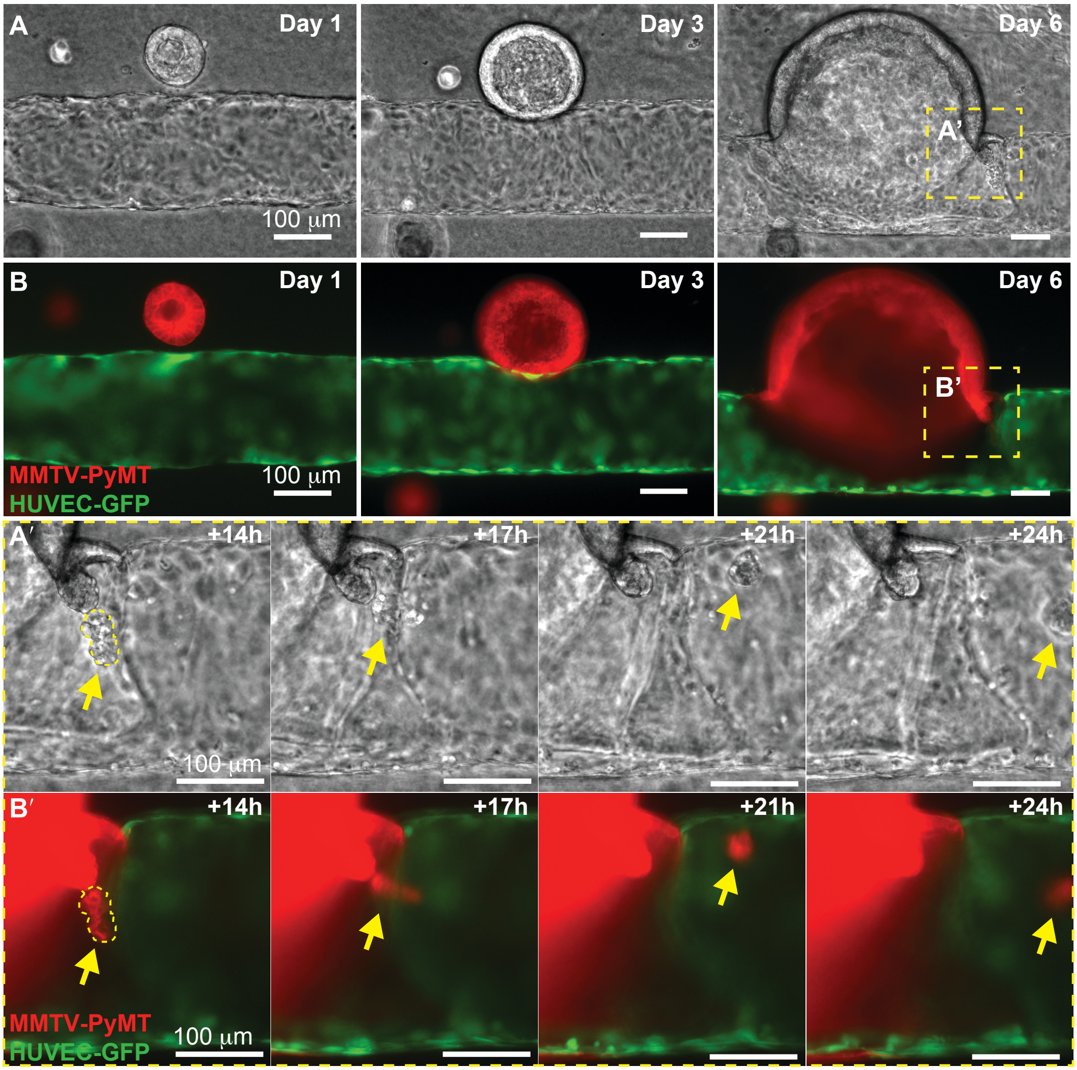

Figure 4-6. Tumors integrate with the endothelial vessel wall in a perfusable 3D microvessel platform with a parallel tumor-vessel arrangement.

(A) Schematic representation of 3D organotypic culture of *ROSAmTmG; MMTV-PyMT* tumor organoids seeded into a vessel device using a parallel tumor-vessel arrangement. (B) Schematic illustration of the side- and end-view of a 150 µm diameter microvessel design and fabrication. In order to fix the distance of the tumor to the vessel, a second cylindrical template rod is introduced into the microvessel platform and the collagen solution is introduced surrounding both rods. Tumor organoids at a high concertation are embedded in lower density collagen-I gels and are introduced into one of the inlets. One of the rods is then slowly removed allowing the introduction of the tumor/collagen gel suspension into the cylindrical channel. After the tumor/collagen solution gels, the second rod is removed resulting in a bare channel which is perfused with media and coated with fibronectin. Endothelial cells are then seeded resulting in a confluent 3D microvessel. The perfusion system is by gravity flow by differential pressure. Flow is kept at 1 mL/h and a shear stress of 4 dynes/cm^2. (C) Schematic illustration of imaging focused at the mid-plane of the vessel and the resulting 2D projected image (right). (D) Fluorescence microscopy image of a *ROSAmTmG; MMTV-PyMT* tumor filled channel and a HUVEC microvessel (GFP) focusing at mid-plane. (E) Frames from a representative fluorescent microscopy time-lapse movie of a collective tumor strand that integrates with the vessel wall forming a mosaic vessel. The tumor cells are exposed to the vessel flow which is kept at 1mL/hour and at a shear stress of 4 dynes/cm^2. Scale bars: (D) 200 µm, (E) 100 µm.

Figure 4-6.

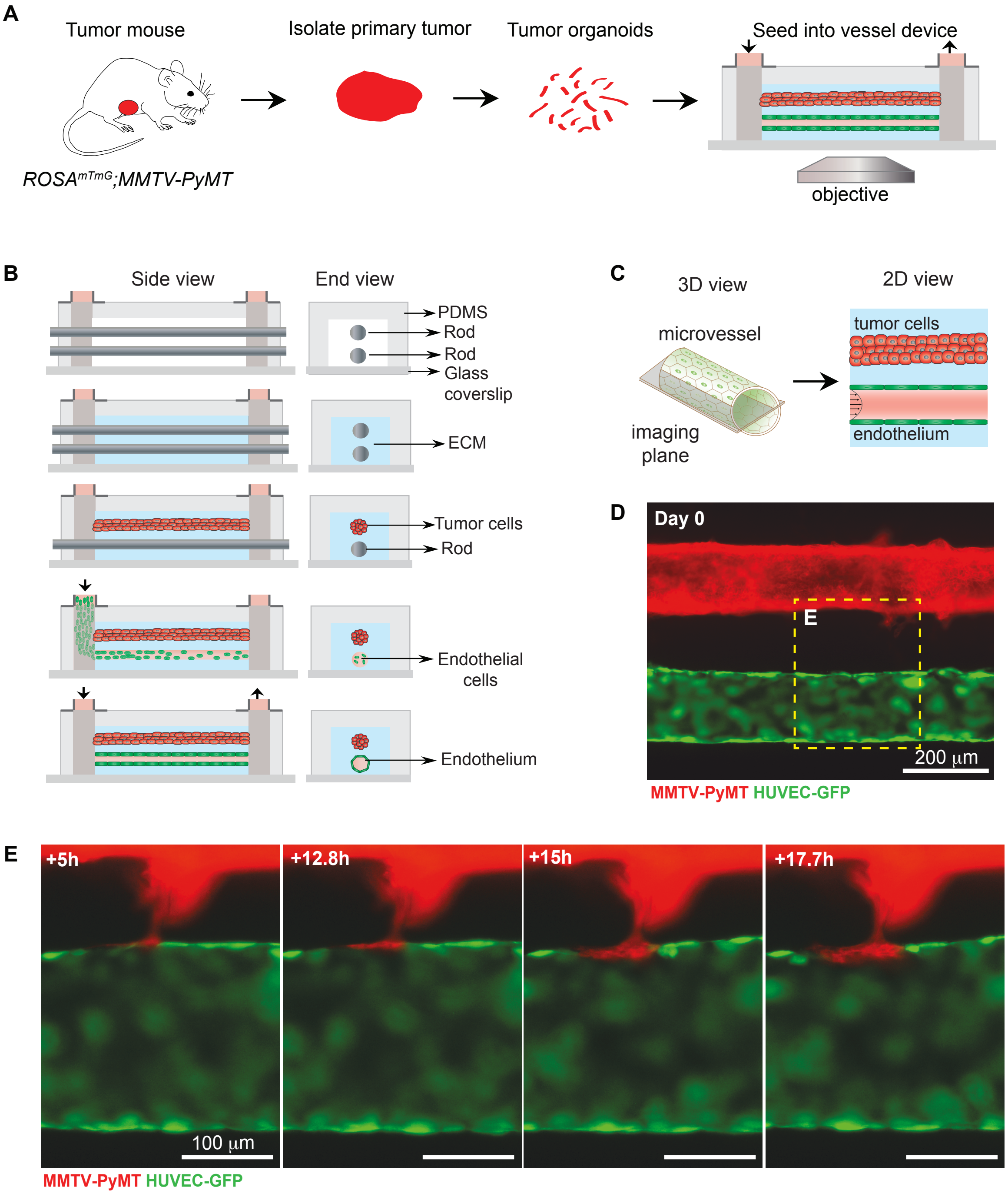
A
Tumor mouse
Isolate primary tumor
Tumor organoids
Seed into vessel device
ROSA^{mTmG};MMTV-PyMT
objective
B
Side view
End view
PDMS
Rod
Rod
Glass coverslip
ECM
Tumor cells
Rod
Endothelial cells
Endothelium
C
3D view
2D view
microvessel
imaging plane
tumor cells
endothelium
D
Day 0
E
200 μm
MMTV-PyMT HUVEC-GFP
E
+5h
+12.8h
+15h
+17.7h
100 μm
MMTV-PyMT HUVEC-GFP

Figure 4-7. Applications of the co-culture of tumor organoids into a perfusable 3D microvessel platform.

(A) Tumor-microvessels model represent a reductive approach to analyze the metastatic process in the context of a 3D platform that introduces physiological relevant geometry and multicellular dimensionality to study the tumor microenvironment. Tumor organoids only or coculture with varying stromal cells can be introduced into a 3D microvessel platform that has a functional vessel lined with endothelial cells with perfusion adapted for live cell imaging. This model can be used to study many aspects of cancer progression, including tumor-vessel interactions (mosaic vessel, vessel constriction and vessel pull) over time, imaging, collecting and analyzing intravasated tumor cells/clusters, and the changes in endothelium homeostasis. (B) Cartoon representations of the three tumor-vessel interactions that can be model using the 3D microvessel platform and the possible implications on the formation of vascular defects and intravasation.

Figure 4-7.

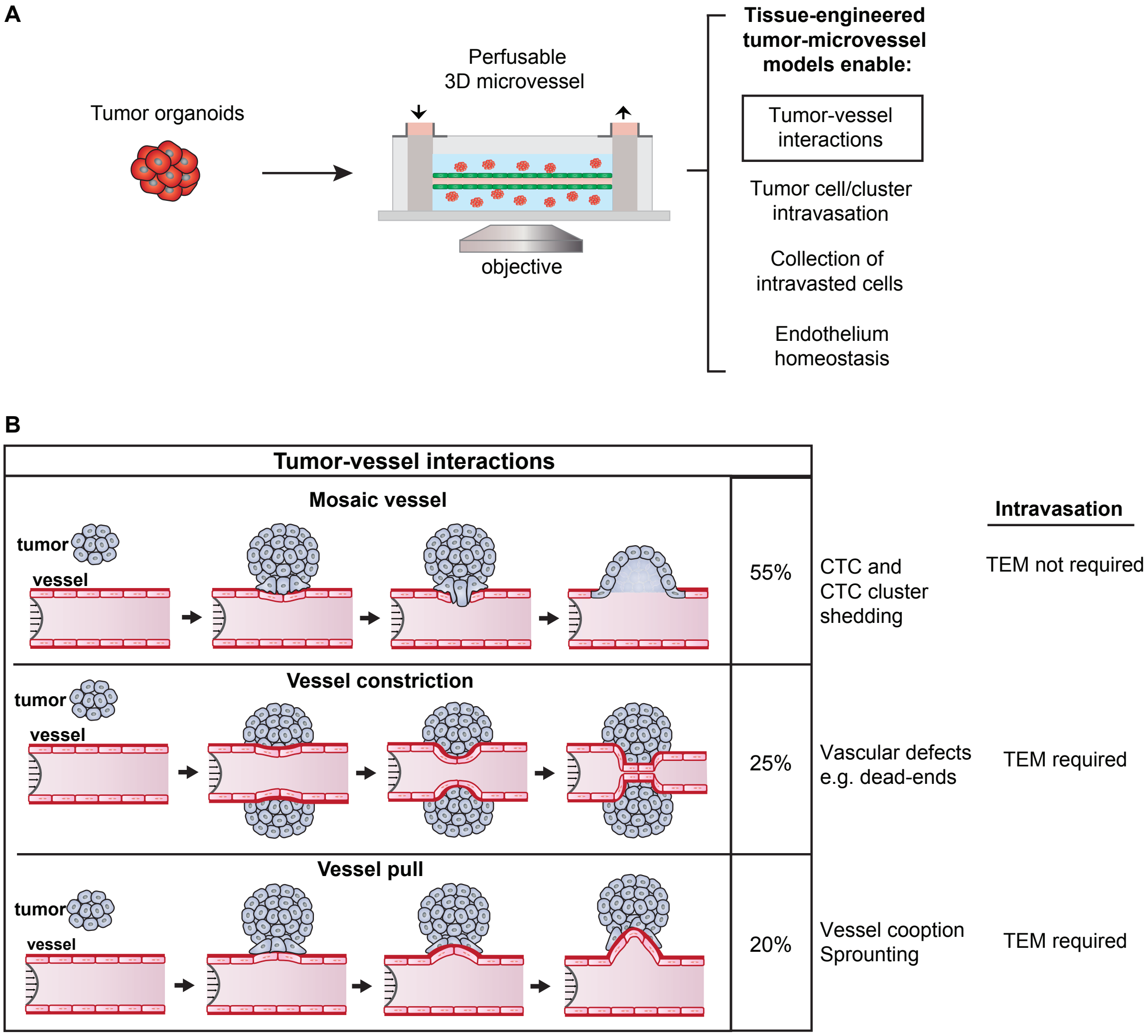
A
Tumor organoids
Perfusable
3D microvessel
objective
Tissue-engineered tumor-microvessel models enable:
Tumor-vessel interactions
Tumor cell/cluster intravasation
Collection of intravasted cells
Endothelium homeostasis
B
Tumor-vessel interactions
Mosaic vessel
tumor
vessel
55%
CTC and CTC cluster shedding
Intravasation
TEM not required
Vessel constriction
tumor
vessel
25%
Vascular defects e.g. dead-ends
TEM required
Vessel pull
tumor
vessel
20%
Vessel cooption Sprounting
TEM required

Supplemental Figure 4-1. Effects of endothelial medium on tumor organoid growth and structure.

(A) Schematic representation of 3D organotypic culture of *ROSA^{mTmG}; MMTV-PyMT* tumor organoids using the same culture conditions in the 3D microvessel device. Organoids from the same mouse were culture either with "organoid media" or endothelial medium with or without dibutyryl-cAMP (db-cAMP) for 5 days. (B-E) Representative still images of tumor organoids for Day 0 (control) and, Day 5 in culture for organoid media supplemented with bFGF, endothelial medium and endothelial medium with db-cAMP, respectively. Scale bar: 50 µm. (F) Tumor organoid growth was evaluated by measuring the projected surface area at Day 0 and Day 5. (G) Mean circularity score. n= number of tumor organoids, r= 2 biological replicates. Error bars indicate s.e.m. P values were determined by the Mann-Whitney test. Differences were considered statistically significant for $p< 0.05$ (H) representative fluorescence still images of tumor organoids cultured in a microvessel device at Day 1 and Day 3 in culture. Flow is kept at 1 mL/hour and a shear stress of 4 dynes/cm$^{2.}$ The direction of the flow is from left to right of the image. Scale bar: 50 µm. (I) Tumor organoid growth within microvessel devices were evaluated by fold increase in projected surface area of organoid at Day 5 divide by Day 1 in culture. n= number of tumor organoids for at least 3 biological replicates. Error bars indicate s.e.m. P values were determined by the Mann-Whitney test. Differences were considered statistically significant for $p< 0.05$.

Supplemental Figure 4-1.

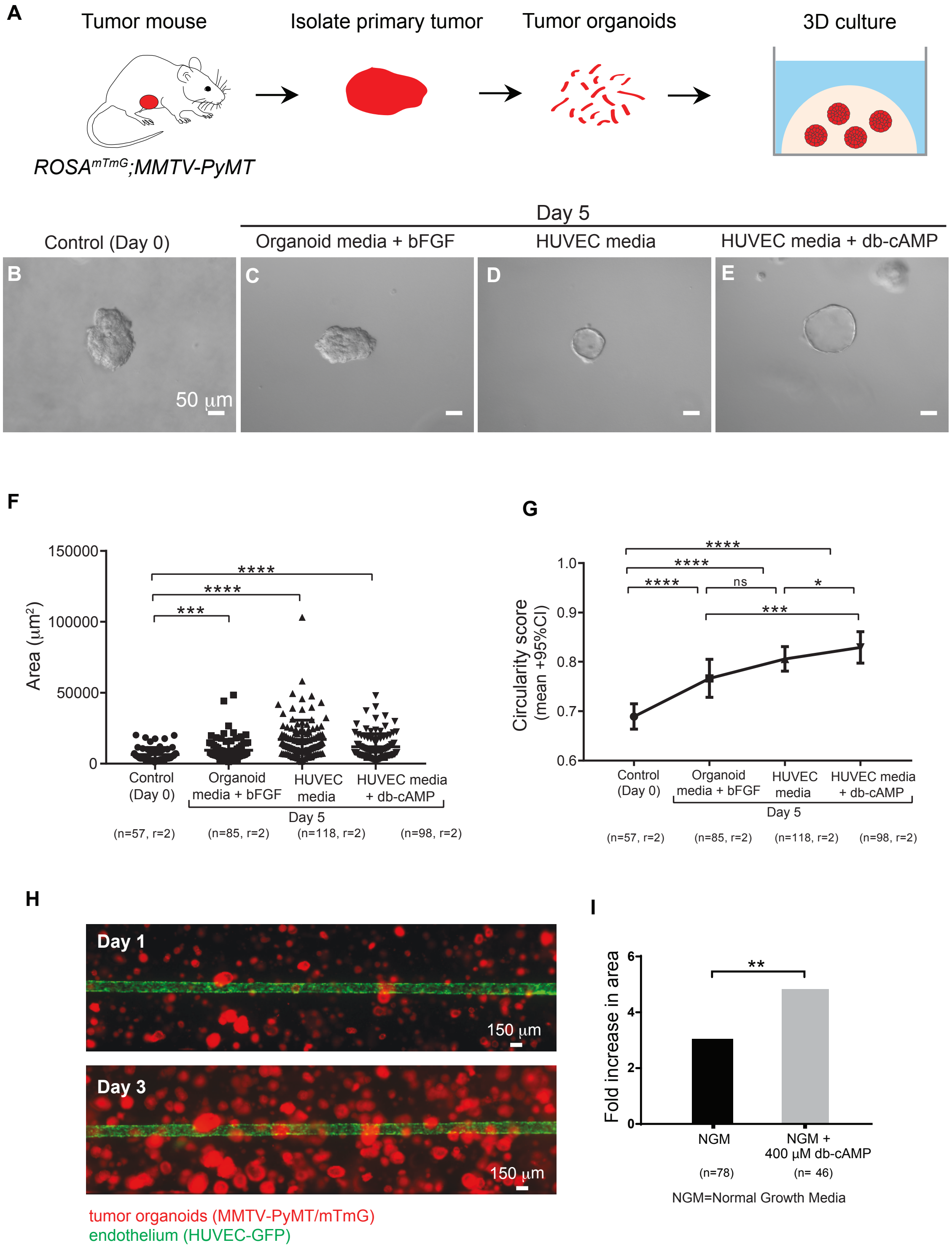

Supplemental Figure 4-2. Microvessel integrity and functionality in the presence of tumor organoids.

Representative fluorescence time series microscopy images of a vessel device cocultured with *ROSAmTmG; MMTV-PyMT* tumor organoids. Permeability was assessed by simultaneously perfusing three different fluorescent molecular weight probes through the vessel lumen: (A-D) 3 kDa dextran (Alexa Flour-488-conjugated), (53)10 kDa dextran (Alexa Flour-647-conjugated). Time = 0 min represents the frame prior to luminal filling (A'-D' and F'-I') which occurs on average at 20 min. (A''-D'' and F''-I'') After luminal filing the fluorescence probes perfuse out of the vessel into the ECM. (E and J) Permeability of 3 kDa and 10 kDa dextran molecular probes increases in the presence of tumor organoids compared to control vessel devices without tumor organoids and decreases when treated with 400 μM dibutyryl-cAMP (db-cAMP) for 24 h. n= number of permeability values calculated for at least 3 biological replicates. Error bars indicate s.e.m. P values were determined by the Mann-Whitney test. Differences were considered statistically significant for $p < 0.05$

Supplemental Figure 4-2.

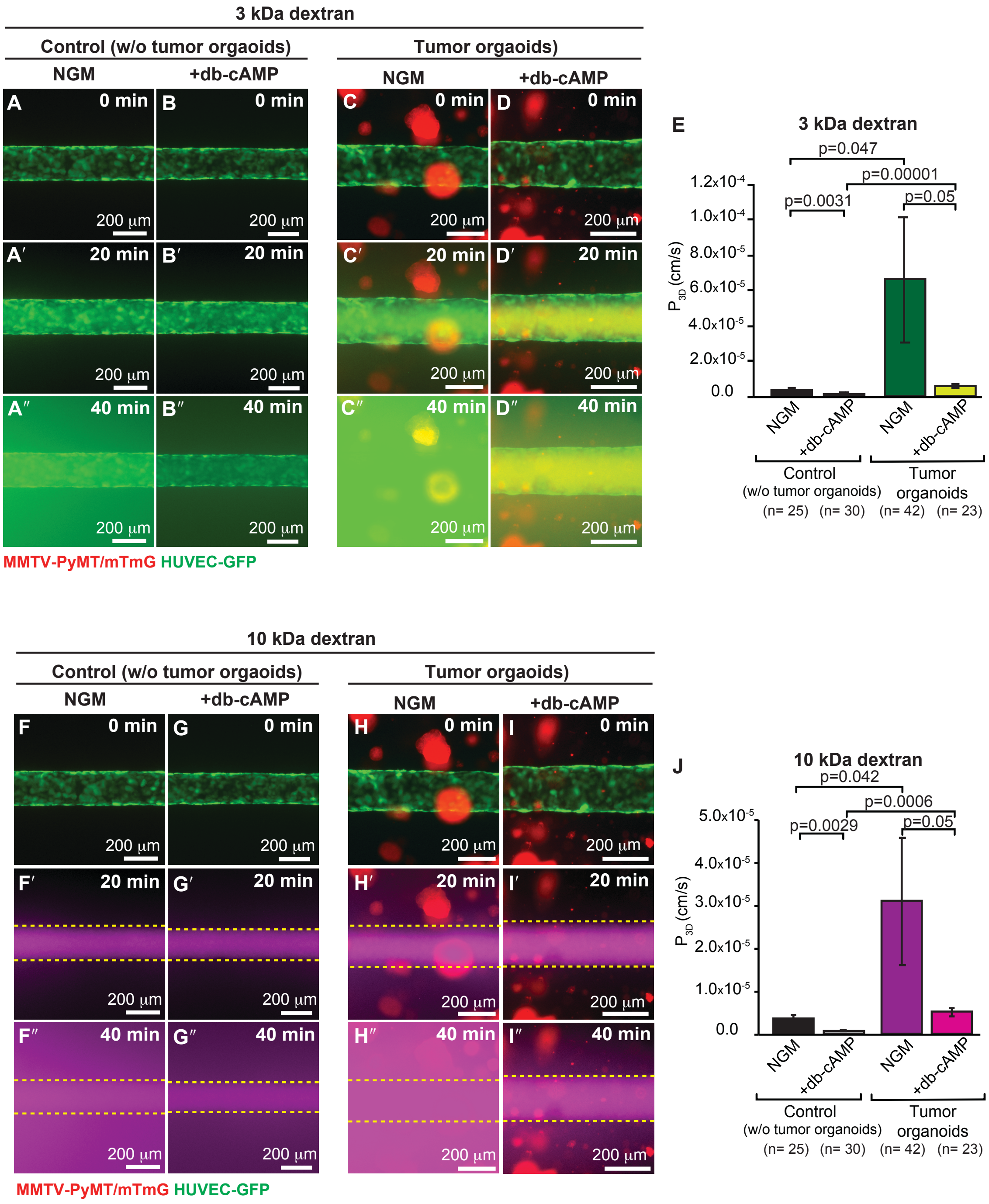

Supplemental Figure 4-3. Endothelial cell proliferation and cell death within a 3D tumor-microvessel model in the presence of tumor organoids.

(A) Schematic illustration of imaging focused at the side view of the microvessel. Individual cell mitosis and death can be visualized and analyzed within the projected endothelium. (B) Representative time-lapse movie of phase-contrast images of an enothelial cell undergoing mitosis. (C) endothelial cell proliferation rates within the microvessel. (D) Representative time-lapse movie of phase-contrast images of an endothelial cell undergoing cell death. (E) endothelial cell death rates within the microvessel. Proliferation and cell death rates are reported as %/h. Scale bar: 30 µm. n= number of devices for at least three biological replicates. Error bars indicate s.e.m. P values were determined by the Mann-Whitney test. Differences were considered statistically significant for $p< 0.05$

Supplemental Figure 4-3.

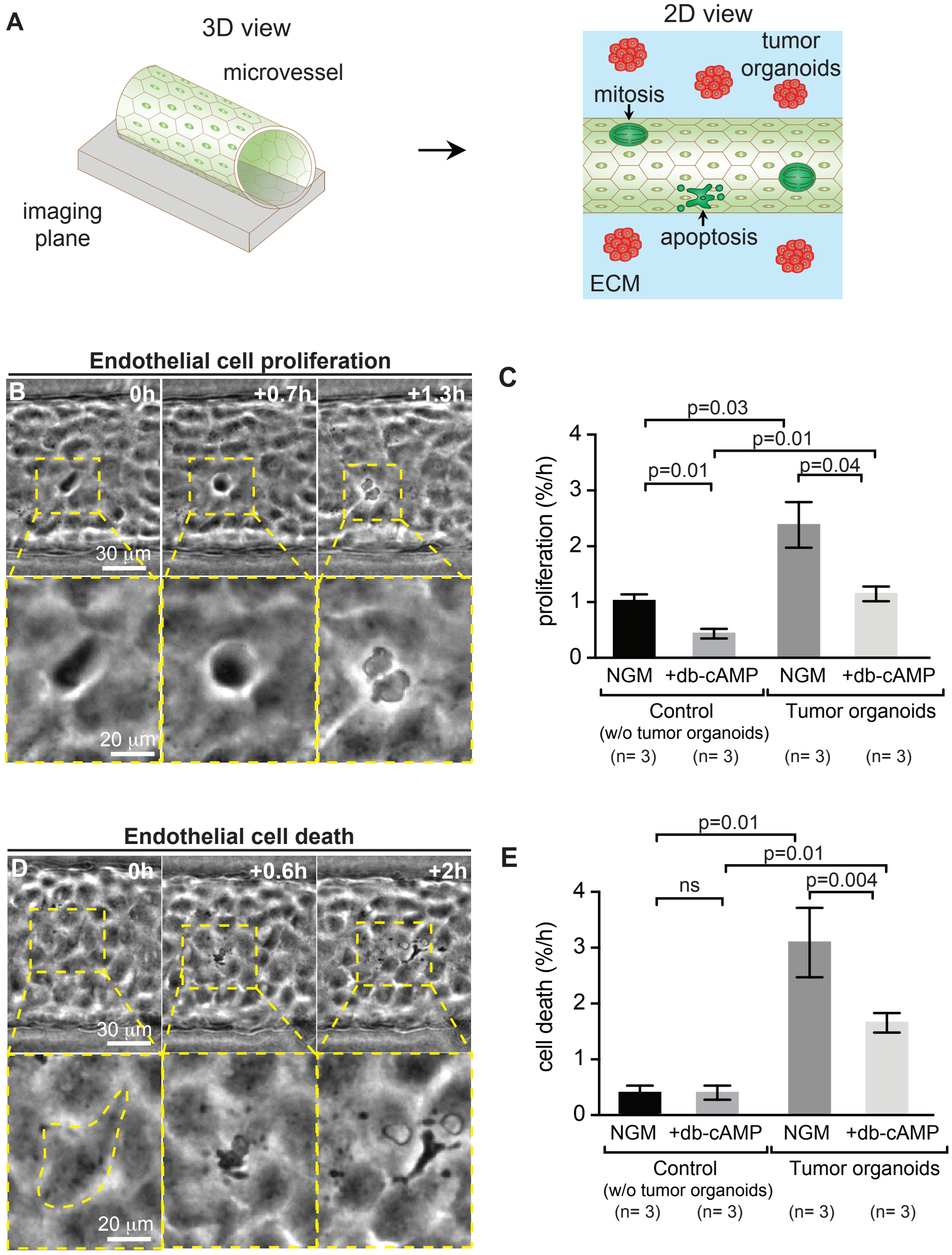

CHAPTER 5

Conclusions related to modeling breast cancer metastasis using a 3D microvessel model of the tumor microenvironment

Concluding remarks

Breast cancer is the second leading cause of cancer-related mortality in women, predicted to cause about 40,000 death in women in the US (American Cancer Society. Breast Cancer Facts & Figures 2015-2016). This, in part, is the result of a lack of a clear understanding of the mechanisms that govern the metastatic process. Cancer metastasis is a complex process that involves a series of steps including invasion, dissemination, intravasation and colonizing a secondary site. One of the challenges in studying metastasis is that certain steps, like tumor cell/cluster intravasation are difficult to observe or manipulate *in vivo*. To overcome this challenge, we developed a microfluidic device that enabled co-culture of tumor organoids with a functional vessel in the context of an ECM that models the relevant tumor microenviroment.

This work aimed to analyze the dynamics of tumor invasion and intravasation using a 3D microvessel platform that allows visualization and real-time monitoring of tumor-vessel interactions (1, 2). The motivation for this work started with a collaboration with Dr. Kevin Cheung (described in Chapter 3) were we found that polyclonal breast cancer metastases originated form the invasion and dissemination of collective tumor epithelium (3). This result challenged the conventional model of cancer metastasis where dissemination, intravasation and colonization of distant sites is described to occur through a single tumor cell intermediate. Although we found tumor cell clusters to be rare in our tumor mouse model, we found that tumor clusters have a higher metastatic potential (>100-fold) compared to single tumor cells *in vivo*. Furthermore, aggregating tumor cells into clusters showed > 15-fold increase in colony formation *in vitro*. These findings are in agreement with clinical studies linking circulating tumor cell clusters with worse patient survival (4).

Previous animal and clinical studies have shown that trauma or massage to the primary tumor increases the number of intravasated single tumor cells and clusters (5). Moreover, CTCs and CTMs were shown to shed into the circulation during tumor resection and, consequently, soft tumor manipulation decreased the risk of metastatic lesions (6-9). Additionally, it was suggested that once inside the vessel, tumor clusters might be limited by the size of the tumor vessel to survive and travel to distant sites (10). Recent studies showed that over 90% of tumor clusters containing up to 20 cells were able to traverse 5 to 10 μm constrictions even in whole blood (11). Using both microfluidics and *in vivo* zebrafish models this study demonstrated that tumor clusters could reorganized in single chains and transit through capillary-sized vessel (11). These observations caused us to think about the ways in which tumors interact with the vasculature to allow the intravasation of polyclonal tumor cell clusters.

Recent advances in microfluidics, particularly in the development of microvessel models that recapitulate perfusable human microvasculature provides unique tools for visualizing the physical and biological factors governing the metastatic process (2, 12, 13). Since tumor vasculature develops relatively quickly, it can lack components of normal microvessels, such as smooth muscle cells, pericytes, and lymphatics (14). As a result, the tumor microvasculature is leakier, with chaotic vessel structures, and with frequent vessel with larger diameters (15).

Using a 3D microfluidic platform to model the tumor microenvironment, we embedded tumor organoids in a collagen-I gel surrounding a functional microvessel under constant perfusion and shear stress. We were able to observe and monitor the formation of three types of tumor-vessel interactions: mosaic vessels (i.e., partial endothelial cell lining), vessel constriction and vessel pull. Furthermore, we found that mosaic vessels are the most frequent type of tumor-vessel interaction observed *in vitro* compared to vessel constriction and vessel pull. The presence of tumor cells within tumor vasculature has long been reported in fixed tissue sections and it has been speculated to contribute to tumor cell intravasation, but the dynamics of this process were never studied (17). Here, we visualized in real-time the formation of a mosaic vessel, followed by the passive shedding of a cancer cell cluster. This result indicates that passive shedding can occur at sites of mosaic vessels, and it implies that active tumor cell migration through the stroma towards the vasculature may not be required. These results agree with previous studies that demonstrates that intravasation occurs mostly within the tumor core where tumors are in direct contact with the vasculature (18).

We also were able to model vascular constriction and vessel pull. The associated mechanical stresses could potentially facilitate intravasation through disruption of vessel structure or drive hypoxia through disruption of vessel function (19, 20). Furthermore, we also observed tumors pulling on the vessel wall which may indicate sites of endothelial cell sprouting or the formation of vessel defects such as dead-ends (2).

In sum, our work reveals the dynamics of tumor-vessel interactions using a 3D microvessel model that contains primary murine breast cancer tissue. Our studies provide a platform to further investigate tumor-vessel interactions by incorporating other components of the tumor microenvironment, such us immune cells. This platform also provides a way to test the effects of cancer therapeutics at the vascular-tumor interphase. A better understanding of these interactions may help to elucidate the anti-vascular effects observed in many therapies and their implications for the treatment of metastasis.

References

1. Nguyen-Ngoc, K.V., et al., 3D culture assays of murine mammary branching morphogenesis and epithelial invasion. Methods Mol Biol, 2015. 1189: p. 135-62.
2. Wong, A.D. and P.C. Searson, Live-cell imaging of invasion and intravasation in an artificial microvessel platform. Cancer Res, 2014. 74(17): p. 4937-45.
3. Cheung, K.J., et al., Collective invasion in breast cancer requires a conserved basal epithelial program. Cell, 2013. 155(7): p. 1639-51.
4. Hou JM, Krebs MG, Lancashire L, Sloane R, Backen A, Swain RK, et al. Clinical significance and molecular characteristics of circulating tumor cells and circulating tumor microemboli in patients with small-cell lung cancer. J Clin Oncol 2012;30:525–32.
5. Liotta LA, Saidel MG, Kleinerman J. The significance of hematogenous tumor cell clumps in the metastatic process. Cancer Res. 1976;36:889–94.
6. Atkin, G., A. Chopada, and I. Mitchell, Colorectal cancer metastasis: in the surgeon's hands? Int Semin Surg Oncol, 2005. 2(1): p. 5.
7. Park, S.Y., et al., Influence of surgical manipulation and surgical modality on the molecular detection of circulating tumor cells from colorectal cancer. J Korean Surg Soc, 2012. 82(6): p. 356-64.
8. Li, W., et al., Laparoscopic surgery minimizes the release of circulating tumor cells compared to open surgery for hepatocellular carcinoma. Surg Endosc, 2015. 29(11): p. 3146-53.
9. Fan, Z.C., et al., Real-time monitoring of rare circulating hepatocellular carcinoma cells in an orthotopic model by in vivo flow cytometry assesses resection on metastasis. Cancer Res, 2012. 72(10): p. 2683-91.
10. Nagakawa, Y., et al., Histologic features of venous invasion, expression of vascular endothelial growth factor and matrix metalloproteinase-2 and matrix metalloproteinase-9, and the relation with liver metastasis in pancreatic cancer. Pancreas, 2002. 24(2): p. 169-78.
11. Au SH, Storey BD, Moore JC, et al. Clusters of circulating tumor cells traverse capillary-sized vessels. Proc Natl Acad Sci U S A. 2016;113(18):4947-52.
12. Bogorad MI, DeStefano J, Karlsson J, Wong AD, Gerecht S, Searson PC. Review: in vitro microvessel models. Lab Chip. 2015;15:4242-4255..
13. Katt ME, Placone AL, Wong AD, Xu ZS, Searson PC. In vitro tumor models: advantages, disadvantages, variables, and selecting the right platform. Front Bioeng Biotechnol. 2016;4:12.
14. Hanahan D, Weinberg RA. Hallmarks of cancer: the next generation. Cell. 2011;144:646-674
15. Folarin AA, Konerding MA, Timonen J, Nagl S, Pedley RB. Three-dimensional analysis of tumour vascular corrosion casts using stereoimaging and micro-computed tomography. Microvasc Res. 2010;80:89-98.
16. Liotta LA, Kleinerman J, Saidel GM. Quantitative relationships of intravascular tumor cells, tumor vessels, and pulmonary metastases following tumor implantation. Cancer Res. 1974;34:997-1004.
17. Chang, Y.S., et al., Mosaic blood vessels in tumors: frequency of cancer cells in contact with flowing blood. Proc Natl Acad Sci U S A, 2000. 97(26): p. 14608-13.

18. Deryugina, E.I. and W.B. Kiosses, Intratumoral Cancer Cell Intravasation Can Occur Independent of Invasion into the Adjacent Stroma. Cell Rep, 2017. 19(3): p. 601-616
19. Helmlinger, G., et al., Solid stress inhibits the growth of multicellular tumor spheroids. Nat Biotechnol, 1997. 15(8): p. 778-83.
20. Padera, T.P., et al., Pathology: cancer cells compress intratumour vessels. Nature, 2004. 427(6976): p. 695.

Curriculum Vitae

VANESA LAURA SILVESTRI

vsilves1@jhmi.edu • 207-629-7804
1110 23rd St NW, Washington, DC 20037

EDUCATION

Johns Hopkins University, School of Medicine, Baltimore, MD **Expected May 2019**
Ph.D. candidate, Biochemistry, Cellular and Molecular Biology Program
Laboratory of Dr. Andrew J. Ewald, Department of Cell Biology

Colby College, Waterville, ME **May 2012**
Bachelor of Arts
Major: Chemistry, Concentration in Cell and Molecular Biology/Biochemistry

RESEARCH EXPERIENCE

Johns Hopkins University, School of Medicine, Baltimore, MD

Ph.D. Student – Dep. of Cell Biology, laboratory of *Dr. Andrew Ewald* **Aug2014-Present**

Rotation Student – Dep. of Neuroscience, laboratory of *Dr. Shantinit Sockanathan* **Jan-Feb 2014**

Rotation Student – Dep. of Neuroscience, laboratory of *Dr. Marie Hardwick* **Aug-Dec 2013**

Colby College, Waterville, ME

Research Technician– Dep. of Cell Biology, laboratory of *Dr. Ronald Peck* **May 2012-July 2013**

Research Assistant (thesis lab)– Biochemistry, laboratory of *Julie T. Millard* **May 2009-Aug 2011**

National Institutes of Health (NIH), Bethesda, MD

Winter Intern– NHGRI, laboratory of *Dr. David Bodine* **Jan 2012-Feb 2012**

WORK AND TEACHING EXPERIENCE

Johns Hopkins University, Baltimore, MD

Invited Lecturer – Tissue Engineering, *Intersession course* **Jan 2019**

Invited Lecturer – Intro to Biology and Medicine, *Intersession course* **Jul-Aug 2018**

Teaching Assistant – Confocal Microscopy, *Dr. Scott Kuo Ewald* **Sep 2017-Nov 2017**

Colby College, Waterville, ME

Teaching and Laboratory Assistant – General Chemistry, *Dr. Dasan Thamattoor* **Sep-Dec 2019**

HONORS AND AWARDS

2017 Isaac Morris Hay and Lucille Elizabeth Hay Graduate Fellowship Award, Johns Hopkins School of Medicine. In recognition of outstanding research in the field of cell biology. Full year scholarship.

2010-11 Colby College Student travel awards for presentations at AACR Meetings.

2009-12 Colby College Presidential Scholar Program. Offered to the top students in each incoming class to conduct research.

ORIGINAL RESEARCH ARTICLES

Cheung, K.J., V. Padmanaban, **V. Silvestri**, K. Schipper, J.D. Cohen, A.N. Fairchild, M.A. Gorin, J.E. Verdone, K.J. Pienta, J.S. Bader, and A.J. Ewald. 2016. Polyclonal breast cancer metastases arise from collective dissemination of keratin 14-expressing tumor cell clusters. *Proceedings of the National Academy of Sciences of the United States of America*. 113:E854-863.

Nguyen-Ngoc, K.V., **V.L. Silvestri***, D. Georgess, A.N. Fairchild, and A.J. Ewald. 2017. Mosaic loss of non-muscle myosin IIA and IIB is sufficient to induce mammary epithelial proliferation. *Journal of Cell Science*. 130:3213-3221
(* indicates co-first author)

Le, P.M., **V.L. Silvestri**, S.C. Redstone, J.B. Dunn, and J.T. Millard. 2018. Cross-linking by epichlorohydrin and diepoxybutane correlates with cytotoxicity and leads to apoptosis in human leukemia (HL-60) cells. *Toxicology and Applied Pharmacology*. 352:19-27

Silvestri, V.L., and J.T. Millard. 2018. Changes in apoptotic gene expression induced by the DNA cross-linkers epichlorohydrin and diepoxybutane in human cell lines. *Data Brief*. 19:932-935.

Silvestri, VL., E. Henriet, A.Wong, P. Searson, A.J. Ewald. 2019. Modeling tumor-vessel interactions in breast cancer metastasis using a tissue-engineered 3D model of the tumor microenvironment. *In Preparation.*

WORKSHOPS AND SYMPOSIA

Dec 2018 3rd Annual Excellence in Diversity Symposium: "Cellular dynamics of tumor-vessel interactions using a tissue-engineered 3D microvessel model of the tumor microenvironment". Baltimore, MD.

Nov 2018 5th Annual Metastatic Breast Cancer Conference: "Cellular dynamics of tumor-vessel interactions using a tissue-engineered 3D microvessel model of the tumor microenvironment". Baltimore, MD.

Dec 2017 American Society of Cell Biology Annual Meeting: “Cellular dynamics of tumor-vessel interactions using a tissue-engineered 3D microvessel model of the tumor microenvironment”. Convention Center. Philadelphia, PA.

May 2017 Fellows Research Day: “Cellular dynamics of tumor-vessel interactions using a tissue engineered 3D microvessel model of the tumor microenvironment” Sidney Kimmel Comprehensive Cancer Center, Johns Hopkins University, Baltimore, MD.

May 2017 11th Annual Nano-Bio Symposium: “Cellular dynamics of tumor-vessel interactions using a tissue-engineered 3D microvessel model of the tumor microenvironment” Sidney Kimmel Comprehensive Cancer Center, Johns Hopkins University, Baltimore, MD.

April 2017 10th Annual Safeway Breast Cancer Research Retreat: “Cellular dynamics of tumor vessel interactions using a tissue-engineered 3D microvessel model of the tumor microenvironment” Mt. Washington Conference Center, Baltimore, MD.

Dec 2016 American Society of Cell Biology Annual Meeting: “Cellular dynamics of tumor vessel interactions using a tissue-engineered 3D microvessel model of the tumor microenvironment”. Convention Center. San Francisco, CA.

April 2016 9th Annual Safeway Breast Cancer Research Retreat: “Cellular dynamics of tumor-vessel interactions using a tissue-engineered 3D microvessel model of the tumor microenvironment” Mt. Washington Conference Center, Baltimore, MD.

Dec 2015 American Society of Cell Biology Annual Meeting: “Collective epithelial dissemination in breast cancer metastasis”. Convention Center. San Diego, CA.

Dec 2015 American Society of Cell Biology Annual Meeting: “Polyclonal breast cancer metastases arise from collective dissemination of keratin 14-expressing tumor cell clusters”. Convention Center. San Diego, CA.

Workshops

Aug 2017 Practical Genomics Workshop, a week long intensive hands-on introduction to analyzing next-generation sequencing data using Unix and R tools. Baltimore, MD.